Computational studies of the initial stages in TiO_2-MOF interface formation

Anuradha Bandaranayake Patabandi Mudiyanselage

A thesis submitted for the degree of Master of Philosophy

School of Chemistry

Cardiff University

February 2022

ABSTRACT

TiO_2 has been significantly used in photocatalytic applications for decades as an inert and sustainable material. However, TiO_2 is less efficient in the photoinduced processes due to the rapid recombination of the photogenerated electrons and holes. Therefore, TiO_2-based heterogeneous composites (i.e., TiO_2-MOF, TiO_2-CNT) are widely investigated given the ability to increase the efficiency of photoinduced applications rather than the individual state of the interacted materials.

This thesis presents a computational chemistry study on the energetics and structures of rutile and anatase TiO_2 polymorphs, the interaction of terephthalic acid (TPA) and metal species with TiO_2, and the interaction of metal organic framework (MOF) nodes with TiO_2, aiming to investigate the TiO_2/MOF heterointerface, which currently is not fully comprehended.

The comparison of energetic, geometric, and electrical properties of bulk rutile and anatase polymorphs of TiO_2 identified that the PBEsol exchange correlation functional with a light basis set is the most appropriate computational approach for discovering TiO_2-based novel materials. The study of different surface energies, geometric and electrical properties of certain low Miller index facets of TiO_2 demonstrated that a 4-layer slab model, with the top 2-layers unconstrained of (110) facet of rutile and the (101) facet of anatase are the best models to study the chemical interactions with TiO_2. The study of TPA interaction with TiO_2 surfaces and the interaction of Zn, Ti and Zr based metal species with the adsorbed TPA on rutile and anatase TiO_2 surfaces gave evidence for the possible layer-by-layer deposition of MOFs on TiO_2. The interaction study of a simplified version of MOF nodes of Zn-MOF-5, Ti-MIL-125 and Zr-UiO-66 with TiO_2 surfaces proved that the deprotonated TPA linkers of MOF nodes favourably bind with the Ti ions on the TiO_2 surface, giving evidence for the possible synthesis of TiO_2-MOF composites using already formed MOF crystals. Generally, the interaction studies concluded that the deprotonated TPA linkers are highly compatible to bind with the TiO_2 surfaces and thus, the growth of MOFs with TPA linkers on TiO_2 is highly favourable. Interactions between bulk crystal structures of different MOFs and hydroxylated TiO_2 surfaces can be investigated to further understand the formation and nature of the TiO_2-MOF interface.

DEDICATION

To my parents, husband and sisters for your endless love, support, and encouragement throughout the whole journey of my life.

ACKNOWLEDGEMENTS

Completion of this work would not have been possible without many beautiful souls being with me all the time.

I gratefully acknowledge my supervisor, Dr. Andrew Logsdail for his kindness, fruitful discussions, guidance, encouragement, time, and support throughout this project.

My sincere thanks also extended to all the members of the Logsdail Group and the School of Chemistry – Cardiff University for the continuous support. Especially, I do greatly appreciate Mr. Harry Thomas for his support in discussions, suggestions, and encouragement throughout this endeavour. Additionally, I am most thankful to Dr. Timothy Easun for the helpful discussions related to MOFs.

I acknowledge the support of the Supercomputing Wales project, which is part-funded by the European Regional Development Fund (ERDF) via Welsh Government.

Via our membership of the UK's HEC Materials Chemistry Consortium, which is funded by EPSRC (EP/R029431), this work used the UK Materials and Molecular Modelling Hub for computational resources, MMM Hub, which is partially funded by EPSRC (EP/T022213).

Last but not least, I would like to thank my parents, husband, sisters and friends for their unconditional love, support, and encouragement.

TABLE OF CONTENTS

LIST OF FIGURES

LIST OF TABLES

ABBREVIATIONS

DFT	Density functional theory
XC	Exchange-correlation
TDDFT	Time-dependent density functional theory
FHI-aims	Fritz Haber Institute ab initio molecular simulations
ASE	Atomic simulation environment
XC	Exchange correlational
BZ	Brillouin zone
ZORA	Zeroth order regular approximation
SCF	Self-consistent field
LUMO	Lowest unoccupied molecular orbital
HOMO	Highest occupied molecular orbital
LDA	Local-density approximation
GGA	Generalized-gradient approximations
MOF	Metal organic framework

CHAPTER 1 - INTRODUCTION

1.1 TiO_2-based materials for photo-induced applications: an overview

Titanium dioxide (TiO_2, titania) is the most extensively investigated and established material for photo-induced functionalities among various semiconducting materials due to the high thermal and chemical stability, less toxicity, minimum production cost and the easily applicable nature at any ambient to harsh condition given the high corrosion resistance.[1–7] According to the electronic structure, TiO_2 is capable of transferring electrons (e_{CB}^-) from the filled valence band (VB) to empty conduction band (CB) leaving a hole (h_{VB}^+) in the VB when the absorbed photoenergy ($h\nu$) exceeds or matches the band gap energy.[8,9] Those photogenerated electrons and holes involve as the charge carriers in different photo-induced processes.[8,9] However, the energy dissipation as heat due to rapid recombination of those photogenerated electrons and holes reduces the efficiency of photo-induced reactions and limits the applications of TiO_2.[1,10–12] Therefore, different strategies to further improve the performance of TiO_2 have been widely investigated in recent years. Examples of those techniques are increasing the light absorption by expanding the absorption wavelength range, increasing the response for visible light and adopting active sites capable of separating photo-induced electrons and holes or suppressing their recombination.[1,13–21] These can be obtained by altering the morphology of TiO_2 to increase the surface (i.e., nanospheres, nanofibers, hollow nanoparticles),[1,13–21] combining with photosensitizers (i.e., quantum dots, organic dyes, perovskites),[22–29] doping with metals (i.e., Fe, Sn, Mo, Co),[1,4,30] doping with non-metals (i.e., B, C, S, N),[1,4] adding metal nanoparticles (i.e., Au, Ag, Mn, Fe, Cr, Cu, Pt, Pd, Rh),[1,4,31–34] combining with other semiconducting material (i.e., Fe_2O_3, CuO, CdSe, CdS, ZnO, SiO_2),[1,35–38] conjugating with different carbon materials [i.e., graphene, carbon nanotubes (CNT)][1,39–42] and, heterojunction formation with mesoporous materials which results in composites with enhanced properties than individual state (i.e., metal organic frameworks (MOFs), zeolites, active carbon).[1,43–49] Among those strategies, TiO_2-MOFs composites have witnessed a huge research effort in the past two decades due to the open metal sites and high porosity in the MOFs which enhance the photocatalytic activity and photoinduced applications.[1] Hereon, this study intends to investigate certain TiO_2-MOF composites among numerous TiO_2-based mesoporous materials for solar energy applications.

1.2 Titania (TiO_2)

TiO_2 was discovered in 1795 as the naturally occurring oxide of titanium, which exists mainly in three types of crystal forms known as rutile, anatase and brookite.[11,50,51] In addition to the main polymorphs, some uncommon polymorphs of TiO_2 such as fluorite, baddeleyite, cotunnite, columbite have been identified at the elevated pressures and temperatures, which assumed to be the minerals found in the mantle of Earth.[11,52,61,53–60] The commercial production of TiO_2 has started back in the 1920s due to a wide range of commercial applications such as coatings for corrosion resistant, opacifying agent of numerous products (i.e., inks, paints, textiles, plastics, etc), self-cleaning surfaces, purification of water and air, ultraviolet radiations absorber in cosmetic products, anti-bacterial agent, and food additives.[4,11,50,51,62–67] Currently, the usage of TiO_2 in industrial level has been enhanced by applications in semiconductors, supercapacitors, photocatalysis, rechargeable batteries, sensors, water remediation, etc.[11,51,68–70] Fundamentally, the electronic structure of the TiO_2 plays the major role to deliver all the valuable properties for numerous applications. In the macroscopic level, rutile TiO_2 has been identified as the most stable TiO_2 polymorph at the ambient conditions, whereas anatase TiO_2 is more stable in the nano-range.[11,51,71,72] In this study, rutile and anatase crystal phases of TiO_2 are investigated towards the formation of TiO_2-MOF composites.

1.3 Metal Organic Frameworks (MOFs)

Metal ions or clusters (i.e., transition metals, alkaline earth metals, p-block metals and actinides) are self-assembled with polydentate organic ligands through coordination bonds to form hybrid nanoporous crystalline framework structures known as MOFs, illustrated in Figure 1.1.[73]

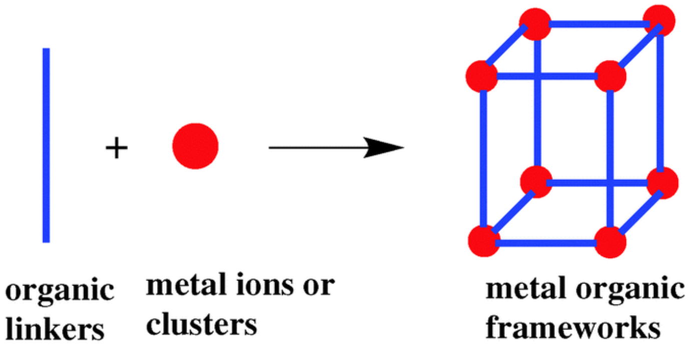

Figure 1.1: Generalised illustration of MOFs formation.*

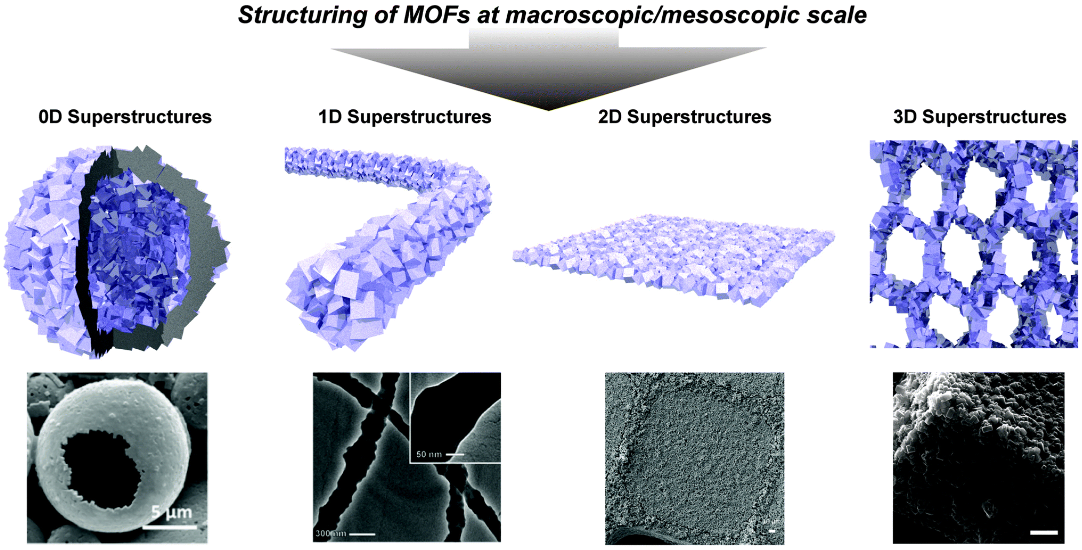

Figure 1.2: Representation of MOFs with different dimensionalities.†

---

* Used with permission of Royal Society of Chemistry, from Metal-organic frameworks as solid catalysts for the synthesis of nitrogen-containing heterocycles, A. Dhakshinamoorthy and H. Garcia, 43, 2014; permission conveyed through Copyright Clearance Center, Inc.

† Used with permission of Royal Society of Chemistry, from Structuring of metal-organic frameworks at the mesoscopic/macroscopic scale, S. Furukawa, J. Reboul, S. Diring, K. Sumida and S. Kitagawa, 43, 2014; permission conveyed through Copyright Clearance Center, Inc.

MOFs, as seen in Figure 1.2, are infinite networks made up of repeating units that can be found in 0D, 1D, 2D, and 3D structures. MOFs are thus used at the macroscopic/mesoscopic scale in Materials science field to develop more intricate and advanced designs.[74] MOFs have a large surface area to volume ratio because of the vast number of nanoscale pores. The open metal sites and high porosity of MOFs result in unique characteristics and properties, leading to potential applications such as heterogeneous catalysis via metal ions, bioreactors, energy production, optics, electronics, molecule storage, gas adsorption, sensing, molecule separation from mixtures, purification via physisorption, chemisorption, drug and biomolecule delivery.[74] Examples for the photocatalytic applications of MOFs include, degradation of organic pollutants, water splitting for H_2 generation, CO_2 reduction, Cr(VI) reduction, etc.[1] Furthermore, photoactive MOFs are used in photoelectric solar energy converters.[1,75–77]

The photoactivity of most of the MOFs occurs mainly via three strategies known as metal to ligand charge transfer (MLCT), ligand to metal charge transfer (LMCT), and the π–π^* transition in the aromatic rings of the organic ligand.[1,78–80] Likewise in titania, the efficiency of photoreactions in MOFs is also reduced by the recombination of photo-induced electrons and holes.[1] Therefore, various research work has been done over the past years for making composites of semiconducting materials and MOFs. In such composites, MOF acts as the photosensitizer and inhibits the recombination of photogenerated electrons and holes by quickly performing the charge transfer over the interface between semiconducting material and the MOF.[1] The different methods of MOFs synthesis are categorised under three main strategies which are: employing two precursor solutions for layer-by-layer deposition of MOFs, using a mixture of precursors and top-down approach. The top-down approach utilises large MOFs crystals to form desired MOFs.[74] In this study, the layer-by-layer growth of MOFs and the deposition of MOFs using a mixture of precursors on TiO_2 are mimicked considering certain Zn(II)-based, Ti(IV)-based and Zr(IV)-based MOFs in which terephthalic acid acts as the organic linker.

1.4 Challenges for the advancement of TiO_2-MOF composites

There are some key challenges to be addressed even though numerous research work have been done for the advancement of TiO_2-MOF composites as efficient photocatalysts, as depicted in the Figure 1.3.[1] Some facts to be focussed on are:

(i) Identifying the preferred crystalline phases and facets of TiO_2 to construct heterogeneous composites with MOFs.[1,81–84]

(ii) The thermodynamically stable and low energy (101) anatase and (110) rutile facets are known to be dominated among the TiO_2 crystals. However, construction between TiO_2 and MOF with a high percentage of high-energy facets can enhance the photoactivity even though it is critical and difficult to achieve.[1,85–89]

(iii) Considering the formation of composites by MOFs and TiO_2 doped with non-metal or metal elements, which are expected to show improved photoactivity, because doping TiO_2 with such elements decreases the band gap and increases the photo response of TiO_2.[1,90–94]

(iv) Different facile synthesis methods need to be considered to precisely control the composite formation.[1,95–99]

1.5 Motivation, aims and objectives

The major inspiration for this investigation was to address the energy demand in the modern society using novel functional materials synthesised from environmentally sustainable resources. The studies presented in this thesis carried out by computational simulations and aimed to investigate the chemical composition and energetics of certain TiO_2-based mesoporous materials to address the challenges in understanding how the properties of such heterogeneous composites can be tailored to enhance the efficiency of solar energy harvesting in photocatalytic and photovoltaic applications.

The general objectives were: (i) to analyse the influence of exchange-correlation functionals on energy, geometry, and electronic structure of anatase and rutile polymorphs of TiO_2; (ii) to build surface structures of TiO_2

to be coupled with MOF linker species towards generating TiO_2-MOF composite materials; (iii) to study the interactions of metal ions with TiO_2 surface bound linker species and, (iv) to study the interactions of MOF nodes with TiO_2 surfaces.

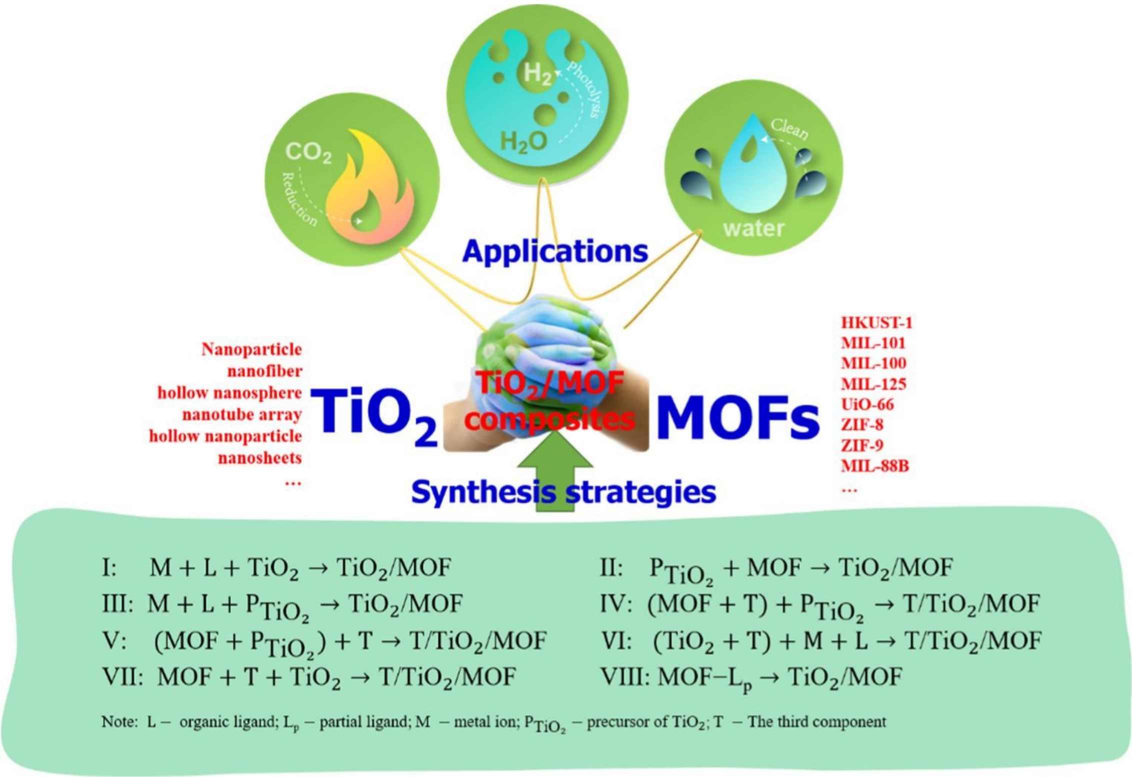

Figure 1.3: Fabrication strategies for TiO_2-MOF composites and promising applications.[‡]

[‡] Reprinted from Chemical Engineering Journal, 391, Chong-Chen Wang, Xun Wang and Wen Liu, The synthesis strategies and photocatalytic performances of TiO_2/MOFs composites: A state-of-the-art review, 123601, 2020, with permission from Elsevier.

CHAPTER 2 - COMPUTATIONAL METHODOLOGY

This chapter describes the techniques used for Density functional theory (DFT) calculations throughout the project. The DFT calculations allow to find the ground state properties of molecular systems.[100] Additionally, the DFT method utilises a set of Schrödinger like variational equations which are solved self consistently providing much accuracy according to Kohn-Sham DFT theory which considers the system as a fictitious system of non-interacting particles.[100] All calculations were performed using the *"Fritz Haber Institute ab initio molecular simulations"* (FHI-aims)[101] software package, along with the Pythonic *"Atomic Simulation Environment"* (ASE)[102] to manage all the geometries. DFT calculations involve various approximations such as exchange correlational (XC) functional, basis set, **k**-point grid for Brillouin zone (BZ) integration, etc.[103] The XC functionals are the semi-empirical functionals which are used in the quantum chemical calculations. A basis set is a set of functions which is used to represent the electronic wave function. The **k**-points are the sampling points in the first Brillouin zone of a material.[103] In this work, the zeroth order regular approximation (ZORA) as a scalar correction was used to include the relativistic effects.[104] A **k**-point density of (0.045 x 2π) Å^{-1} was used for the periodic calculations, unless otherwise stated for defining the number of **k**-point splits along the three reciprocal axes of the first BZ. The approach followed to decide a relevant **k**-point density has been explained further in the section 3.2. An explicit analytical stress tensor computation was requested for the unit cell relaxations. The convergence criteria for the self-consistent field (SCF) calculations based on total energy, sum of the eigenvalues and charge density were less than 10^{-6} eV, 10^{-3} eV and 10^{-6} e a_0^{-3} respectively. The convergence criteria for energy derivatives was 10^{-4} eV Å^{-1}. The spin of each system was set to zero.

The band gap was calculated as below:

$$E_g = E_{LUMO} - E_{HOMO} \qquad 2.1$$

where E_g is the band gap energy, E_{LUMO} is the energy of Lowest Unoccupied Molecular Orbital (LUMO) of the charge transfer compound and, E_{HOMO} is the energy of Highest Occupied Molecular Orbital (HOMO) of the charge transfer compound.

CHAPTER 3 - TiO_2 BULK MODELS

3.1 Introduction

Several computational studies have been performed over the past years to investigate the properties of TiO_2 due to the existence of different crystalline phases with different properties and a broad range of applications.[105] Theoretical prediction of the properties of the TiO_2 phases is important for the design of TiO_2 based materials as the thermodynamically favourable structures should be most easily accessible.[105] Anatase and rutile polymorphs have been extensively investigated previously compared to the other phases because those two compete to be the ground state.[106] The majority of experimental work with bulk titania have been done with rutile TiO_2, which is thermodynamically most stable.[106] However, anatase TiO_2 has been identified as the most stable polymorph within nanostructured TiO_2. DFT calculations with most XC functionals report that anatase TiO_2 is more stable compared to rutile TiO_2.[106] Apart from the investigations of stability, several calculations have also been carried out to investigate Ti-related defects and Oxygen vacancies in TiO_2 because the photocatalytic activity of the material is mainly influenced by them.[107] Moreover, a wide range of TiO_2 based materials have been investigated using DFT calculations to predict the ways to enhance the photoactivity. In that regard, doping with metallic (i.e., 3d and 4d transition metals) or non-metallic (i.e., carbon nanotubes, carbon nanodots) elements and further chemical modifications have achieved a great attention.[11,108–110] Furthermore, DFT/TDDFT (Time-dependent density functional theory) studies of TiO_2-based materials for dye-sensitized and perovskite solar cells have been performed to predict prominent materials and to understand their interfacial properties, adsorption energies, structural changes, etc.[111]

Herein, a comparative DFT study has been performed to investigate the dependence of predicted properties (i.e., lattice parameters, formation energies and band gap energies) on the computational approach, which can be achieved by comparing with reported experimental results. Identification of the most reliable computational approach is important for subsequent further discover of thermodynamically stable TiO_2-based novel materials.

3.2 Methodology for calculation of properties of TiO_2

The most stable polymorphs of TiO_2 at standard temperatures and pressure are anatase and rutile, which have been considered herein. The unit cell of anatase (Ti_4O_8) is displayed in Figure 3.1, and has lattice parameters of $a = b = 3.785$ Å and $c = 9.512$ Å.[112] The unit cell of rutile (Ti_2O_4) is displayed in Figure 3.2, and has lattice parameters of $a = b = 4.593$ Å and $c = 2.959$ Å.[113]

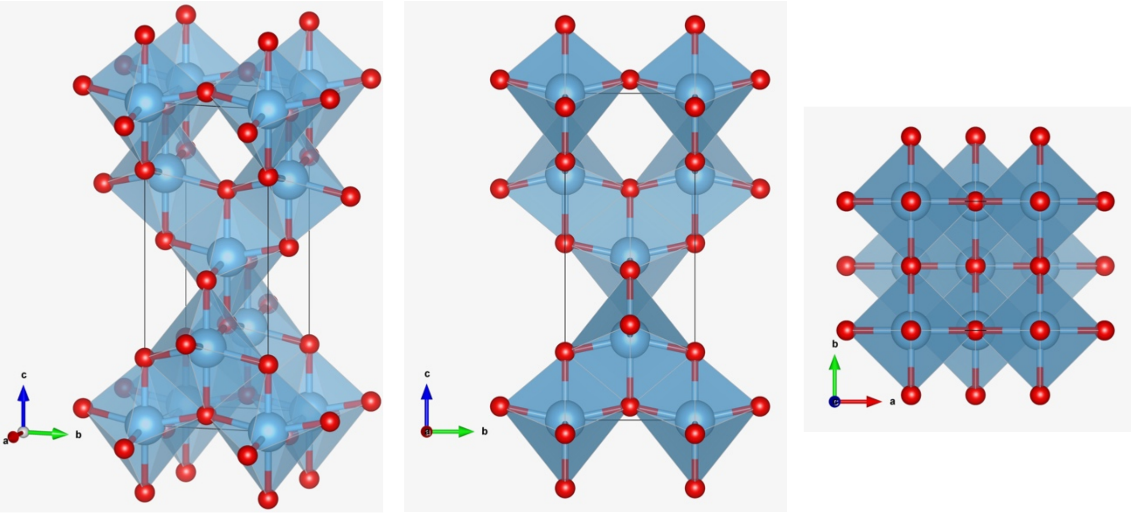

Figure 3.1: Polyhedral views of the unit cell of anatase TiO_2 where blue spheres represent titanium atoms, red spheres represent oxygen atoms, and a black line highlights the conventional unit cell.

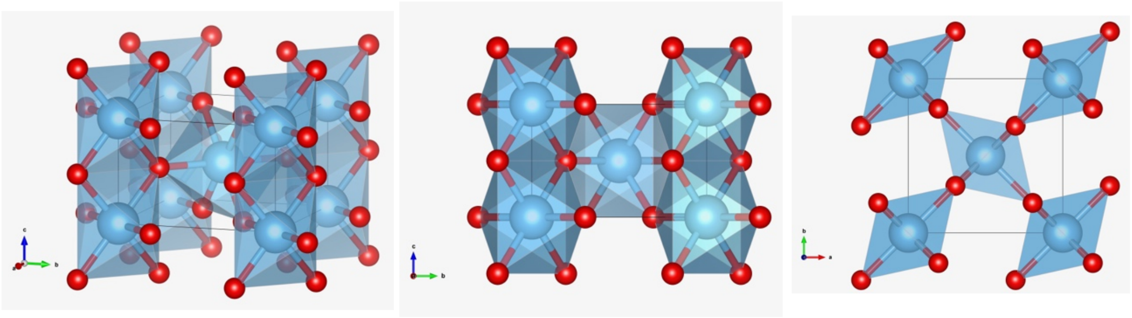

Figure 3.2: Polyhedral views of the unit cell of rutile TiO_2 where blue spheres represent titanium atoms, red spheres represent oxygen atoms, and a black line highlights the conventional unit cell.

Both anatase and rutile TiO_2 have a tetragonal crystal structure and asymmetric unit cells.[114] Several additional atoms than the number of atoms in the unit cells of anatase (Ti_4O_8) and rutile (Ti_2O_4) are shown in the Figure 3.1 and Figure 3.2 for the better visualisation of the surrounding polyhedrons in the crystal structures. The total energy of each bulk model is given from the DFT calculations by integrating the Hamiltonian over the BZ. The **k**-points which are the sampling points in the first BZ used in such integrations are important because the results highly depend on those points in the **k**-grid (i.e., mostly the conduction band minima and the valence band maxima are located at the high symmetry points).[101,115] The precision of a calculation is increased by a higher number of **k**-points, though with the overhead of greater computational cost. Therefore, carrying out a convergence testing to find a reliable **k**-grid density is important to decide the optimum **k**-grid for each calculation.[103] In this study, convergence testing for the **k**-point density was performed using the PBE XC functional and a light basis set. The Γ-centered grid type was used, in which the integers in the **k**-grid defines the number of splits along the reciprocal lattice vectors in the model.[101]

In this study, the **k**-point density was tested from $(0.030 \times 2\pi)$ $Å^{-1}$ to $(0.050 \times 2\pi)$ $Å^{-1}$ in increments of $(0.005 \times 2\pi)$ $Å^{-1}$ and the total energies were compared as shown in the Table 3.1 and Figure 3.3. According to the table 3.1, the total energy of the TiO_2 bulk models is almost same from **k**-point density $(0.030 \times 2\pi)$ $Å^{-1}$ to $(0.045 \times 2\pi)$ $Å^{-1}$, whereas the total energy at $(0.050 \times 2\pi)$ $Å^{-1}$ has been clearly increased. The change in energy from the prior **k**-point energy calculation (ΔE) is also show in the Figure 3.3. The divergence of energy occurs at higher **k**-point densities due to the good screening properties of the material as the tiny energy differences also have been converged.[116] Therefore, the **k**-point density at $(0.045 \times 2\pi)$ $Å^{-1}$ was taken as the converged **k**-point density for the two materials, given the necessity to minimise the computational cost, and this setting is used in all subsequent periodic calculations herein.

Table 3.1: Convergence testing of **k**-grid sampling of anatase and rutile polymorphs of TiO_2. The energy change (ΔE) as a function of the sampling was calculated. The selected converged result is highlighted in blue.

k-grid density (Å⁻¹)	k-grid			Total E (meV)	ΔE (meV)
	a	b	c		
Anatase					
0.030	9	9	4	-109602050.69	-
0.035	8	8	3	-109602050.67	-0.019
0.040	7	7	3	-109602050.79	0.120
0.045	6	6	2	-109602050.65	-0.142
0.050	5	5	2	-109602048.83	-1.827
Rutile					
0.030	7	7	11	-54800907.32	-
0.035	6	6	10	-54800907.31	-0.008
0.040	5	5	8	-54800907.23	-0.074
0.045	5	5	8	-54800907.23	0.000
0.050	4	4	7	-54800906.83	-0.404

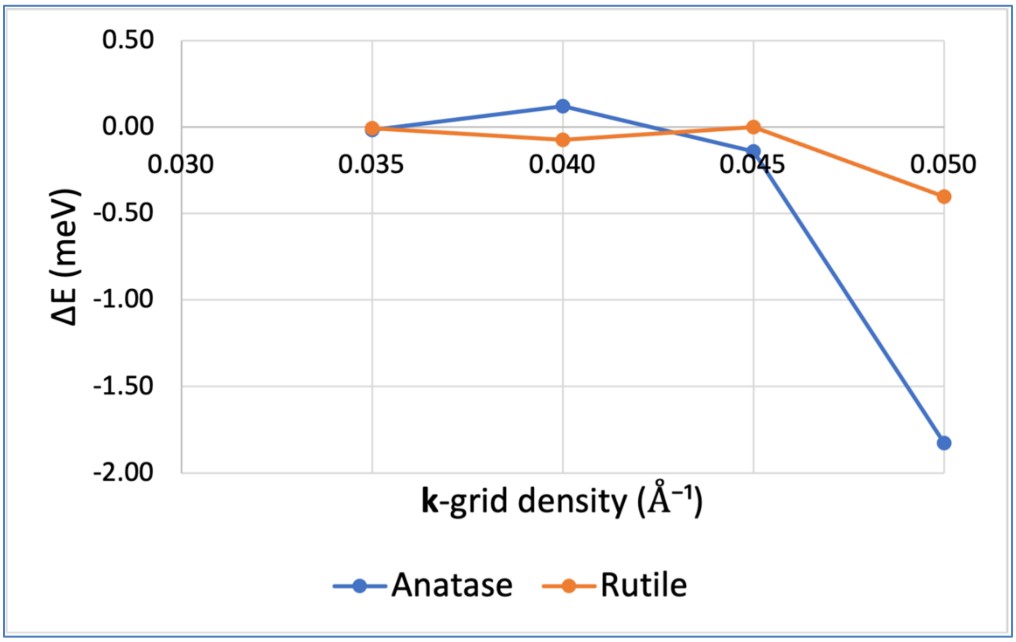

Figure 3.3: Plot of the energy change from previous calculation (ΔE) vs. **k**-grid density of rutile and anatase TiO_2

The Table 3.2 lists the XC density functionals considered in this study to investigate the properties of TiO_2 bulk models, so as to identify a reliable XC functional and a basis set for our work. Additionally, the non-local many-body dispersion (MBD-NL) correction was applied with PBE to test the effect of non-local van der Waals corrections.[117] The unit cell parameters and nuclear coordinates of anatase and rutile TiO_2 were optimised using those XC functionals and the available light, intermediate and tight basis sets in the FHI-aims software package to deliver accuracy while also considering the computational efficiency.[118]

Table 3.2: The XC density functionals considered in this study.

Approximation type	XC density functional
Local-density approximation (LDA)	LDA[119]
Generalized-gradient approximations (GGA)	AM05[120], PBE[121], PBEsol[122], rPBE[123]
Meta-generalized gradient approximations (meta-GGA)	M06-L[124], SCAN[125], mBEEF[126]
Hybrid functionals	B3LYP[127], HSE06[128], PBE0[129]
Hybrid Meta-generalized gradient functionals	M06[130]

In addition to the unit cells of anatase and rutile TiO_2, a triplet-state O_2 gas molecule and a bulk Ti system with a unit cell of $a = b = 2.934$ Å and $c = 4.657$ Å, containing two Ti atoms, were optimised. The respective total energies were used to calculate the formation energy of TiO_2.[131,132] For the bulk Ti, a converged 8 x 8 x 5 **k**-grid was used for the periodic calculations, which corresponds to the $(0.045 \times 2\pi)$ Å^{-1} **k**-point density. Generally, the DFT calculations of Ti have been performed with a higher number of **k**-points (i.e., 80 Å/S_i where S_i is system dimensions and *i* is *x*, *y* slab dimensions,[133] 256 **k**-points in the irreducible BZ[134]) and **k**-point grids such as 10 x 10 x 10.[135] The formation of anatase and rutile unit cells were considered as below.

Anatase: $4Ti\ (s) + 4O_2\ (g) \longrightarrow Ti_4O_8\ (s)$ 3.1

Rutile: $2Ti\ (s) + 2O_2\ (g) \longrightarrow Ti_2O_4\ (s)$ 3.2

Therefore, the formation energy (E_{form}) of TiO_2 per formula unit was calculated using the equations:

$$E_{Ana,form} = [E_{Ana,bulk} - 4E_{O_2} - 4E_{Ti,bulk}]/4 \quad 3.3$$

$$E_{Rut,form} = [E_{Rut,bulk} - 2E_{O_2} - 2E_{Ti,bulk}]/2 \quad 3.4$$

where $E_{Ana,bulk}$ is the total energy of the bulk anatase TiO_2 (Ti_4O_8), $E_{Rut,bulk}$ is the total energy of the bulk rutile (Ti_2O_4), $E_{Ti,bulk}$ is the total energy of the bulk Ti (Ti_2) and, E_{O_2} is the total energy of a O_2 gas molecule which is in the ground state with a spin multiplicity value of 3. Hence, the triplet state of O_2 gas molecule was considered. However, the typical overbinding of O_2 when interacting with the transition-metals has not been considered in this study.[136–138]

3.3 Results and discussion

The energetics, geometric and electrical properties of bulk anatase and rutile TiO_2 have been compared with theoretical and experimental investigations in the literature. The unit cells of anatase and rutile TiO_2 that mentioned in the section 3.2 were used for the calculations without fixing the unit cell parameters.

3.3.1 Formation energy of TiO_2

The reaction between solid Ti with O_2 gas was assumed to be involved in the formation of TiO_2 polymorphs as shown in the equation 3.1 and 3.2 (i.e., they are reference states). According to the NIST-JANAF Thermochemical Tables, the formation energy at 298 K of rutile and anatase are -944.0 kJ/mol[139,140] and -938.72 kJ/mol,[139,141] respectively. These values have been compared with calculated formation energies using equations 3.3 and 3.4, as shown in Table 3.3 and Table 3.4. Furthermore, Table A1-1 shows the data obtained with intermediate and tight basis sets.

Table 3.3: The calculated formation energies (E_{form}) using different XC functionals with a light basis set and their difference than the experimental data (ΔE_{form}). Literature values are highlighted.

XC functional	Rutile		Anatase	
	E_{form} (eV)	ΔE_{form} (eV)	E_{form} (eV)	ΔE_{form} (eV)
LDA	-10.250	-0.466	-10.253	-0.524
AM05	-9.016	0.768	-9.073	0.656
PBE	-9.041	0.743	-9.106	0.623
PBEsol	-9.345	0.439	-9.371	0.358
rPBE	-8.469	1.315	-8.570	1.159
M06-L	-9.356	0.428	-9.269	0.460
SCAN	-10.481	-0.697	-10.376	-0.647
SCAN[105]	-10.656		-10.680	
mBEEF	-9.804	-0.020	-9.873	-0.144
B3LYP	-10.021	-0.237	-10.100	-0.371
HSE06	-9.614	0.170	-9.646	0.083
PBE0	-9.577	0.207	-9.614	0.115
M06	-10.276	-0.492	-9.856	-0.127
Formation energy at 298 K[139]	-9.784		-9.729	

Table 3.4: The calculated formation energies (E_{form}) using PBEsol XC functional and different basis sets and their difference than the experimental data (ΔE_{form}).

XC functional	Basis set	Rutile		Anatase	
		E_{form} (eV)	ΔE_{form} (eV)	E_{form} (eV)	ΔE_{form} (eV)
PBEsol	Light	-9.345	0.439	-9.371	0.358
	Intermediate	-9.273	0.511	-9.309	0.420
	Tight	-9.322	0.462	-9.382	0.347

The formation energies calculated using LDA, SCAN, mBEEF, B3LYP and M06 XC functionals along with the light basis set underestimate the formation energy, while the majority of the other XC functionals including AM05, PBE, PBEsol, rPBE, M06-L, HSE06 and PBE0 overestimate. Additionally, the formation energy obtained using the SCAN XC functional with the light basis set match well with the reported SCAN prediction of formation energies of anatase and rutile TiO_2; though the difference from experiment is higher than other XC functionals.[105]

3.3.2 Geometric properties of TiO_2

Unit cell lengths and the angles of optimised structures, obtained using different XC functionals and basis sets, have been compared with the reported experimental data and computational calculations as shown in Table 3.5 - 3.7. Moreover, Table A1-2 and Table A1-3 show the data obtained with intermediate and tight basis sets.

Table 3.5: Unit cell parameters (*a* and *c*), their difference than the experimental data (Δ*a* and Δ*c*) and, the *β* angle of the rutile TiO_2 calculated using different XC functionals with a light basis set. Literature values are highlighted.

XC functional	*a* (Å)	Δ*a* (Å)	*c* (Å)	Δ*c* (Å)	*β* (°)
LDA	4.550	-0.043	2.926	-0.033	90.000
AM05	4.597	0.004	2.948	-0.011	90.000
PBE	4.643	0.050	2.973	0.014	90.000
PBE[105]	4.644		2.967		
PBE+U (6 eV)[105]	4.679		3.044		
PBEsol	4.591	-0.002	2.948	-0.011	90.000
rPBE	4.685	0.092	2.988	0.029	90.000
M06-L	4.605	0.012	2.989	0.030	90.000
SCAN	4.594	0.001	2.964	0.005	90.000
SCAN[105]	4.591		2.957		
SCAN+U (2 eV)[105]	4.604		2.982		
mBEEF	4.625	0.032	2.970	0.011	90.000
B3LYP	4.619	0.026	2.973	0.014	90.002
HSE06	4.578	-0.015	2.958	-0.001	89.996
HSE (25% Fock)[105]	4.582		2.946		
PBE0	4.575	-0.018	2.954	-0.005	90.000
M06	4.600	0.007	2.952	-0.007	89.999
Neutron diffraction data at 295 K[142]	4.593		2.959		

Table 3.6: Unit cell parameters (*a* and *c*), their difference than the experimental data (Δ*a* and Δ*c*) and, the *β* angle of anatase TiO_2 calculated using different XC functionals with a light basis set. Literature values are highlighted.

XC functional	*a* (Å)	Δ*a* (Å)	*c* (Å)	Δ*c* (Å)	*β* (°)
LDA	3.744	-0.041	9.489	-0.023	90.000
AM05	3.769	-0.016	9.640	0.128	90.000
PBE	3.800	0.015	9.742	0.230	90.000
PBE[105]	3.802		9.703		
PBE+U (6 eV)[105]	3.881		9.765		
PBE+U[Ti][143]	3.88		9.77		
PBE+U[Ti,O][143]	3.86		9.74		
PBEsol	3.772	-0.013	9.584	0.072	90.000
rPBE	3.823	0.038	9.843	0.331	90.000
M06-L	3.796	0.011	9.663	0.151	90.000
SCAN	3.851	0.066	8.979	-0.533	90.004
SCAN[143]	3.777		9.587		
SCAN+U (2 eV)[105]	3.805		9.599		
mBEEF	3.770	-0.015	9.846	0.334	90.000
B3LYP	3.781	-0.004	9.765	0.253	90.000
HSE06	3.762	-0.023	9.644	0.132	90.000
HSE (25% Fock)[105]	3,756		9.615		
HSE15[143]	3.78		9.64		
PBE0	3.759	-0.026	9.631	0.119	89.982
M06	3.766	-0.019	9.651	0.139	90.002
Neutron diffraction data at 295 K[142]	3.785		9.512		

Table 3.7: Unit cell parameters (*a* and *c*), their difference than the experimental data (Δ*a* and Δ*c*) and, the *β* angle of rutile and anatase TiO_2 calculated using PBEsol XC functional and different basis sets.

Basis set	*a* (Å)	Δ*a* (Å)	*c* (Å)	Δ*c* (Å)	*β* (°)
Rutile					
Light	4.591	-0.002	2.948	-0.011	90.000
Intermediate	4.587	-0.006	2.944	-0.015	90.000
Tight	4.589	-0.004	2.938	-0.021	90.000
Anatase					
Light	3.772	-0.013	9.584	0.072	90.000
Intermediate	3.766	-0.019	9.586	0.074	90.000
Tight	3.768	-0.017	9.561	0.049	90.000

The crystal structure data of rutile match well with the experimental data, though there are slight overestimations and underestimations within the range of 0.001 - 0.090 Å. The difference between the calculated and experimental *c* lattice parameter of anatase TiO_2 shows comparatively higher values; in that regard, LDA and PBEsol XC functionals show the smallest differences. Overall, the *β* angle of all the calculations agrees with the typical TiO_2 unit call angle, which is 90°.

3.3.3 Electrical properties of TiO_2

The energy gap between the conduction and valence band, known as the band gap, is important for the optical excitation; the overall performance of a material in the photovoltaic applications is determined by the band gap. Approximately, the band gap for anatase and rutile TiO_2 are ~3.2 eV and ~3.0 eV respectively according to the reported experimental studies.[144,145] The band gap of the optimised structures using different XC functionals and basis sets have been calculated using the equation 3.5, and compared with the reported experimental data and computational calculations in Table 3.8. Additionally, Table A1-4 shows the data obtained with intermediate and tight basis sets.

Table 3.8: Calculated band gap (E_g) using different XC functionals and basis sets and, their difference than the experimental data (ΔE_g). Literature values are highlighted.

XC functional	Rutile (eV)	E_g (eV)	Anatase (eV)	E_g (eV)
LDA	1.77	-1.26	2.09	-1.11
AM05	1.79	-1.24	2.15	-1.05
PBE	1.77	-1.26	2.13	-1.07
PBE[105]	**1.83**		**2.10**	
PBE+U (6 eV)[105]	**2.49**		**2.82**	
PBEsol	1.77	-1.26	2.11	-1.09
rPBE	1.77	-1.26	2.14	-1.06
M06-L	2.06	-0.97	2.44	-0.76
SCAN	2.08	-0.95	2.02	-1.18
SCAN[105]	**2.23**		**2.56**	
SCAN+U (2 eV)[105]	**2.47**		**2.80**	
mBEEF	2.19	-0.84	2.66	-0.54
B3LYP	3.53	0.50	3.92	0.72
Gaussian basis, B3LYP			**3.70**	
HSE06	3.27	0.24	3.65	0.45
HSE (25% Fock)[105]	**3.42**		**3.77**	
PBE0	4.06	1.03	4.42	1.22
M06	4.03	1.00	4.38	1.18
Experimental data at 298 K[144,145]	**3.03**		**3.20**	
LCAO-PBE[106]	**1.88**		**2.36**	
LCAO-PBE0[106]	**4.05**		**4.50**	
PAW-PBE[106]	**3.03**		**2.08**	
OLCAO-LDA-AE	**1.78**		**2.04**	
PW-PPS-LDA[106]	**1.88**			
LMTO-ASA+G0W0[106]	**2.50**			
PW-PPs-PBE+G0W0[106]	**2.05**			

From Table 3.8, we see that most of the calculated band gaps, in this study as well as reported values, underestimate or overestimate the experimental band gap by about ~1 eV. Previously, this error has been attributed to the limitations of the DFT approach.[146–148] According to the electron paramagnetic resonance (EPR) experiments, oxygen vacancies in TiO_2 create Ti^{3+} 3d defect states around ~0.8 eV below the CB.[149–153] However, DFT calculations place the defect states within the CB, and the electrons are delocalised over the Ti ions, leading to a failure in generating much agreeable band gaps. According to the study done by Ohler *et al.*, the DFT+U approach has been identified as a possible way to overcome this effect.[133] The DFT+U approach, introduces an on-site U parameter (Hubbard correction) in eV for localised electrons which aims at a correct description of the derivative discontinuity and avoids the additional Hartree-Fock calculations of the exchange energy.[133,136] In this study, B3LYP and HSE06 hybrid XC functionals are in good agreement with the expected results.

3.4 Conclusions

The above results of bulk TiO_2 were considered to decide a reliable XC functional and a basis set for further calculations in this study. The comparison of formation energies, unit cell parameters and band gap energies show that the HSE06 hybrid XC functional with a light basis set provide data in excellent agreement with the experimental investigations; however, these come with a computational overload. The PBEsol XC functional with a light basis set also provides favourable accuracy, and efficiency in computational calculations. Additionally, the typical overbinding of O_2 in the Ti-O systems when using PW91 and GGA functionals has found to be less when using the PBEsol functional due to the cancellation of errors to a certain degree.[136–138] Therefore, PBEsol XC functional with a light basis set was selected for the continuation of this whole study to investigate promising TiO_2-MOF conjugates; however, a hybrid functional such as HSE06 can be recommended to further studies of photovoltaic properties of such materials.

CHAPTER 4 - TiO_2 SURFACE MODELS

4.1 Introduction

Over the last decade, remarkable progress has been made in the design and investigation of the TiO_2 facets due to their different morphology-dependent activities, such as facilitating the movement of charge carriers and light absorption which lead to the development of energy applications.[154]

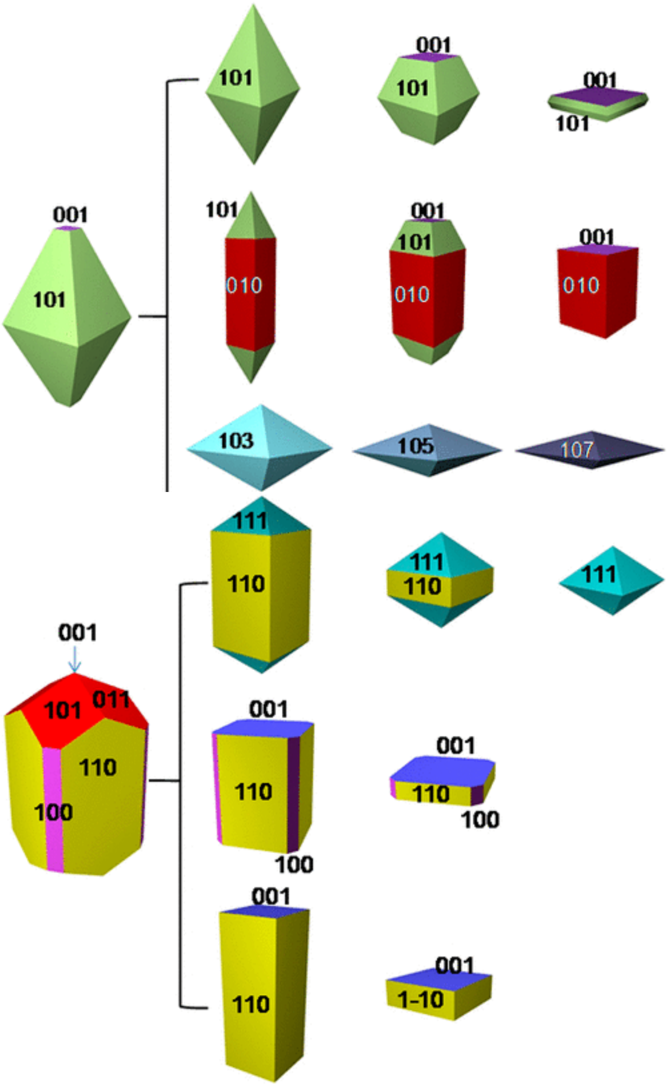

Figure 4.1: Equilibrium crystal shape and other evolved shapes with different facets of (a) anatase and (b) rutile TiO_2, which were obtained via the Wulff construction.§

---

§ Reprinted (adapted) with permission from *Chem. Rev.* 2014, 114, 19, 9559–9612. Copyright 2014 American Chemical Society.

The Wulff construction has been used to study the equilibrium crystal shape and other derived shapes of anatase and rutile TiO_2 composed of different facets as shown in the Figure 4.1.[155] Several energy minimisation arguments are used in the Wulff construction to identify the preferred planes in the equilibrium crystal shape and those planes are specified as Miller indices according to a notation system.[155] The facets contribute to the largest area of the stable equilibrium structures are identified as the most stable equilibrium crystal structures.[155] Synthesis of TiO_2 facets have been used different temperatures, surface treatments and surface-sensitive techniques whereas the structural information has been obtained using different techniques, such as X-ray diffraction (XRD), scanning tunnelling microscopy, X-ray Photoelectron Spectroscopy (XPS), etc. However, there are some issues associated with such investigations due to the thermodynamic stability of facets, which affected by reconstruction and phase transitions at different temperatures.[156] Therefore, several theoretical work have been given rise to understand the structures of the relaxed surfaces of these facets, hydroxylated surfaces of these facets, stable thicknesses of thin films and electrical properties. In this regard, low Miller index facets of (110), (101), (001) and (100) have been studied using both computational and experimental investigations although (110) rutile and (101) anatase TiO_2 are identified as the thermodynamically most stable facets.[133,154,156,157] Nevertheless, several studies have been demonstrated that the above relative stability can be varied according to the functionalisation and applications of these facets [i.e., the fluorine-terminated (001) anatase facet is energetically preferable than the (101),[158] the (110) anatase facet is most stable for photocatalytic oxygen evolution reaction while the (001) facet is most stable for photocatalytic hydrogen evolution reaction,[154] both (101) and (110) rutile facet are stable for photocatalytic oxygen evolution reaction,[154] etc]. Additionally, these facets show different properties compared to the bulk models due to the presence of differently coordinated oxygen and titanium atoms as well as the oxygen vacancies in the outermost relaxed surface, which were formed when removing the nearby layer.[159] Therefore, fundamental studies identifying the significance of each crystal facet are essential to understand the tremendous applications of thin films of these facets.

4.2 Methodology for generation of TiO_2 bulk models and calculations

The optimised bulk structures of anatase and rutile TiO_2 using the PBEsol functional, and a light basis set were used to generate different two-dimensional slab models. The (1 x 1) slab models were generated with (101), (001), (100) and (110) Miller index for anatase (Figure 4.2) and, with (110) and (101) Miller index for rutile (Figure 4.3), which are the most prominent and investigated surfaces among different Miller indices of TiO_2 shown in the Figure 4.1.[114,154,160–166]

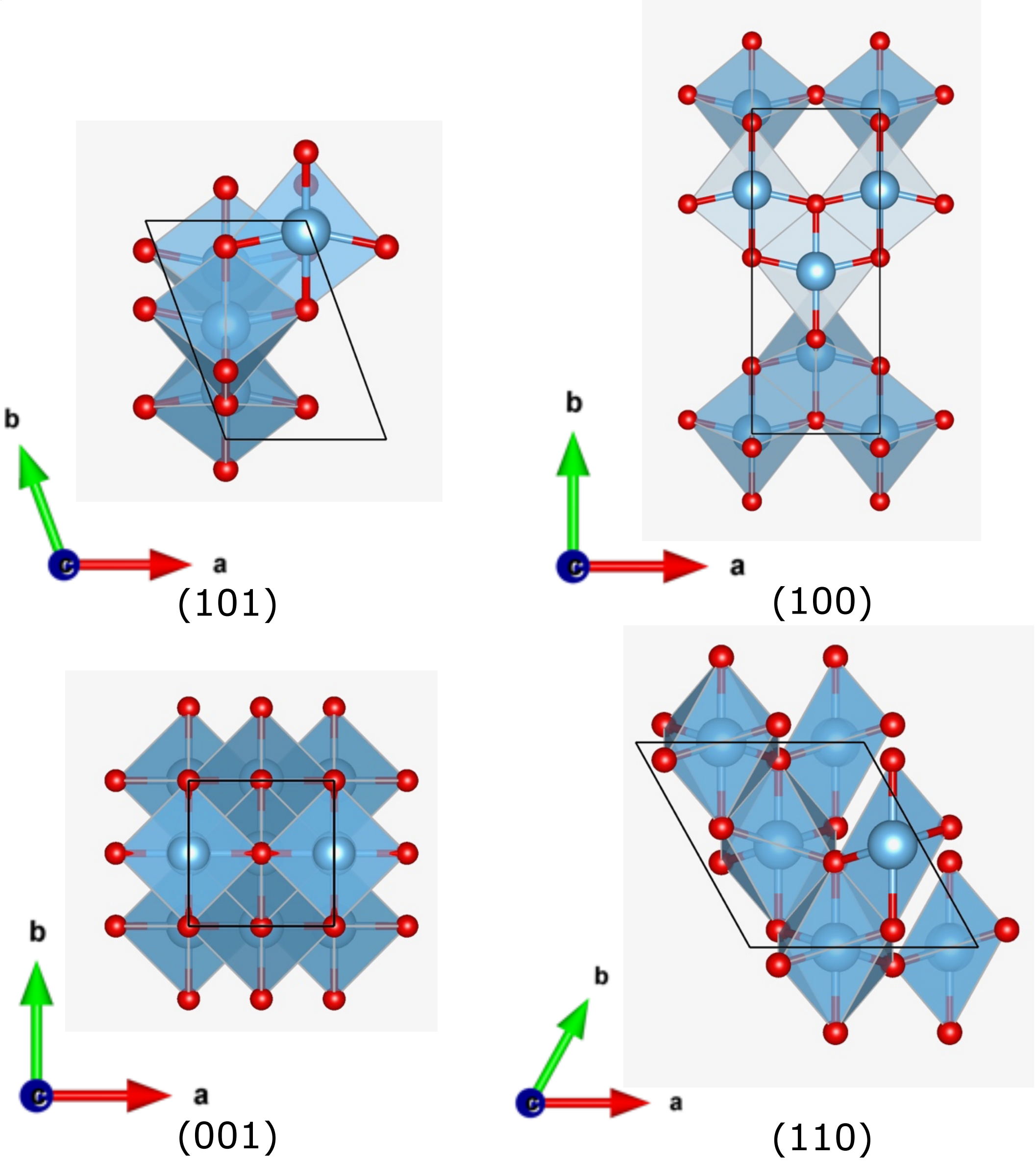

(101) (100) (001) (110)

Figure 4.2: Top-down view along the *xy* plane of different facets of anatase TiO_2 where blue spheres represent titanium atoms, red spheres represent oxygen atoms, and a black line highlights the conventional unit cell.

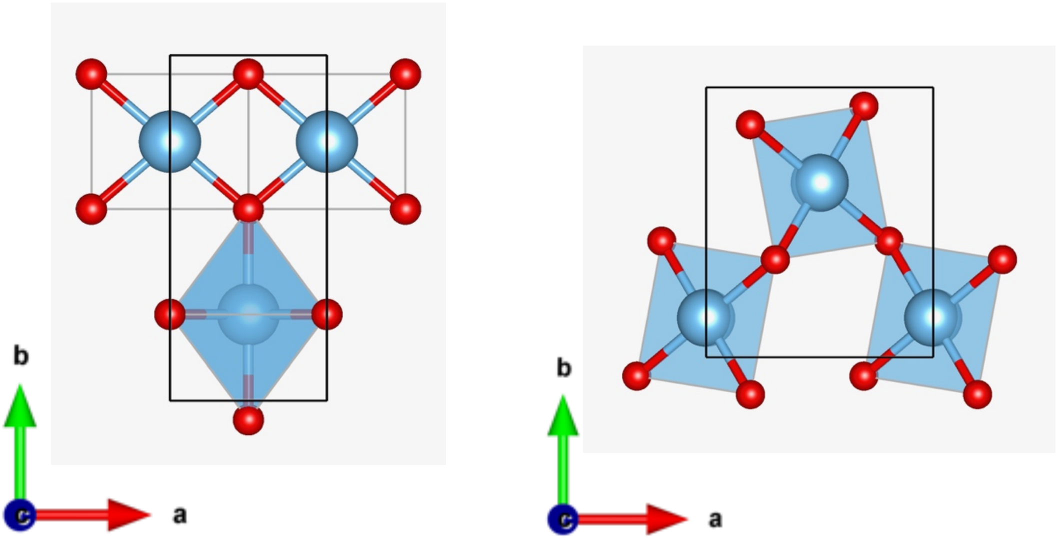

(110) (101)

Figure 4.3: Top-down view along the *xy* plane of different facets of rutile TiO_2 where blue spheres represent titanium atoms, red spheres represent oxygen atoms, and a black line highlights the conventional unit cell.

Among the different surface facets of TiO_2, (110) rutile has been identified as the most stable facet and it has been extensively studied. The (110) rutile surfaces are already existed in the nature and can be considered as a prototype of the oxide surface of TiO_2. The structure of (110) rutile is formed by neutral atomic layers where one layer consists of the O-Ti_2O_2-O composition.[159,167] Likewise, a Ti_2O_4 unit was considered as a single layer in each facet for the comparison of results in this study. The slab thickness was varied as a parameter to be converged where number of layers considered ranged from 1-6 for the study (Table A2-1 and A2-2). Slabs of (100) anatase and (001) anatase were built only with even number of Ti_2O_4 layers, while other facets generated both even and odd number of layers given the structural geometry of the facets.

Geometry optimisations were performed with varying number of top layers unconstrained until mid-depth of the slab. Layers after the mid depth were not unconstrained as it allows relaxation of so many layers, which could lead to unusual results. A vacuum of 20 Å in total was introduced above and below the surfaces (i.e., perpendicular to the *xy*-plane). For each surface facet, the

k-grid was maintained at the **k**-point density of (0.045 x 2π) Å^{-1}. However, the **k**-grid of the *z* direction was set to 1 because surfaces are periodic only in *x* and *y* directions while a vacuum exists in the *z* direction. A dipole correction was introduced in the vacuum region. The dipole correction introduces an electrostatic potential step during the surface slab calculation, to compensate for a potential surface dipole.[101]

The total energies of the cleaved and relaxed slab were used to calculate the energy of cleavage and the relaxation, respectively. The surface energy (γ_{hkl}) was then used to determine the relative stability of the facets. The equation to calculate the γ_{hkl} of each face with Miller indices (hkl) was derived as below:

$$E_C = \frac{E_{surf,fix} - (s.E_{bulk})}{A} \tag{4.1}$$

$$E_R = \frac{E_{surf,rel} - E_{surf,fix}}{A} \tag{4.2}$$

$$\gamma_{hkl} = E_C + E_R = \frac{1}{A}[2E_{surf,rel} - E_{surf,fix} - (s.E_{bulk})] \tag{4.3}$$

where, E_C is the cleavage energy for generating the (1 x 1) slab model of the facet, $E_{surf,rel}$ is the total energy of the slab model after the relaxation, $E_{surf,fix}$ is the total energy of the generated slab model before the relaxation (i.e. with bulk structure), A is the surface area of one side of the slab model in the xy-plane, E_R is the relaxation energy of the slab model, E_{bulk} is the total energy of the unit cell and s is the number of unit cells in the slab model. When calculating the cleaved energy and the relaxation energy, only the unconstrained top surface is considered.

The relaxation of unconstrained surface atoms along the *x* axis was calculated as below:

$$\Delta x = x_{rel} - x_{unrel} \tag{4.4}$$

where Δx is the relaxation along the x axis, x_{rel} is the *x* coordinate of a specific atom of relaxed slab and x_{unrel} is the *x* coordinate of the same atom of unrelaxed slab. Likewise, the relaxations of unconstrained surface atoms along the *y* and *z* axes also calculated.

4.3 Results and discussion

The surface energies, geometric and electrical properties of different low Miller index facets of anatase and rutile TiO_2 were compared with the reported theoretical and experimental studies to understand the significance of those surfaces.

4.3.1 Surface energy of different TiO_2 facets

Testing the surface energy by varying the slab thickness and atomic constraints is important to determine the appropriate converged settings. The surface energies were calculated using the equations in the section 4.2 and represented in Table 4.1 to determine the stability of various facets. The lowest surface energies are the (101) facet of anatase and the (110) facet of rutile in agreement with the experimental evidence.[168] Moreover, the surface energies of different slabs varying the thickness up to six Ti_2O_4 layers and constraints up to mid-depth can be compared as depicted in the Figure 4.4, where the surface energy was converged with the top 2-layers unconstrained from a 4-layer slab model.

Unsurprisingly, the unrelaxed surface slabs show higher surface energies due to the constrains for relaxing after slicing through the bulk TiO_2 to generate surface slab models. According to the Table 4.1, the surface energies become similar when increasing the number of layers in the slab as energy is converged. The relaxation has greatly lowered the surface energy of (110), (101) and (100) facets of anatase TiO_2, but not the (001) facet (Table 4.1). The (001) facet has been identified as a minority surface in most truncated bipyramidal anatase TiO_2 nanocrystals which has the (001) facets as bases while the main faces consist of (101) planes according to the Wulff construction as depicted in the Figure 4.1.[155,168] The reported surface energy with LDA functional (0.66 J m^{-2}) agrees with the converged surface energy value (0.65 J m^{-2}) of (101) anatase in this study. The converged surface energy obtained for the (001) anatase in this study (1.22 J m^{-2}) is lower than the reported surface energies with LDA functional (1.36 J m^{-2}, 1.52 J m^{-2}). The calculated unrelaxed surface energies of (110) rutile using PBEsol functional with a light basis set in this study match with the literature, 1.48 J

m^{-2} using GGA-PW91 functional[157] even though some other previously reported values such as 1.71 J m^{-2} (LDA),[156] 1.78 J m^{-2} for 6-layer slab (LDA)[169,170] are higher. Moreover, the surface energy of a relaxed slab of (110) rutile are reported in the literature as 1.10 J m^{-2} (LDA, 3-layer slab),[156] 0.83 J m^{-2} (LDA, 6-layer slab),[156] 0.84 J m^{-2} (LDA, 6-layer slab),[170] 0.81 J m^{-2} (GGA-PW91, 3-layer slab)[171] and 0.80 J m^{-2} (GGA-PW91, 6-layer slab)[172] in agreement with the calculated values from this study.

Surface energies of the (110) rutile shows an oscillating odd-even behaviour, which has been previously identified.[159,166] The surface energies of slabs with odd number of layers are higher compared to the surface energies of slabs with even number of layers. Slabs with odd number of layers have an extra symmetry of reflection at the centre which mirror the atomic displacements on two sides of the slab.[159,166] This constrains the relaxation of the slabs and increases the surface energy.[159,166] Those interactions are getting weaker with increasing the number of layers and tend to converge. The energy convergence rate in the slabs with even number of layers is higher than the slabs with odd number of layers.[159,166]

Table 4.1: Surface energy (J m^{-2}) for the (1 x 1) slab models in different facets of anatase and rutile TiO_2 which were generated by varying the thickness and constraints on the layers. The converged results are highlighted in blue. (The unrelaxed and relaxed slab models are mentioned as unrel. and rel. respectively).

Number of unconstrained top layers	Surface energy with respect to total number of layers in the slab (J m^{-2})						Lit. values (J m^{-2})
	1	2	3	4	5	6	
(101) Anatase							
All constrained	1.238	1.324	1.322	1.322	1.322	1.322	1.28(unrel.)[168] PBE 0.49(rel.)[168] PBE 0.76(rel.)[133] LDA 0.66(rel.)[133] LDA
1	-	0.678	0.705	0.705	0.705	0.573	
2	-	-	0.629	0.646	0.647	0.515	
3	-	-	-	-	0.634	0.502	
(110) Anatase							
All constrained	2.010	2.229	2.241	2.242	2.242	2.243	2.17(unrel.)[168] PBE 1.15(rel.)[168] PBE
1	-	1.302	1.381	1.387	1.388	1.388	
2	-	-	1.195	1.269	1.273	1.273	
3	-	-	-	-	1.251	1.254	
(100) Anatase							
All constrained	-	1.440	-	1.632	-	1.642	1.59(unrel.)[168] PBE 0.58(rel.)[168] PBE
1	-	0.476	-	0.895	-	0.902	
2	-	-	-	0.755	-	0.799	
3	-	-	-	-	-	0.757	
(001) Anatase							
All constrained	-	1.276	-	1.277	-	1.277	1.12(unrel.)[168] PBE 0.98(rel.)[168] PBE 1.36(rel.)[133] LDA 1.52(rel.)[133] LDA
1	-	1.224	-	1.224	-	1.224	
2	-	-	-	1.224	-	1.224	
3	-	-	-	-	-	1.224	
(110) Rutile							
All constrained	2.021	1.452	1.579	1.555	1.561	1.560	0.65(rel.)[133] LDA 0.67(rel.)[133] LDA 0.89(rel.)[156] LDA 0.73(rel.)[157] GGA
1	-	0.555	0.933	0.875	0.888	0.886	
2	-	-	0.808	0.704	0.749	0.742	
3	-	-	-	-	0.711	0.687	
(101) Rutile							
All constrained	1.662	0.186	1.313	1.318	1.319	1.319	1.47(rel.) LDA[173] 1.03(rel.) GGA[173]
1	-	1.871	1.208	1.216	1.214	1.215	
2	-	-	1.856	1.856	1.180	1.183	
3	-	-	-	-	1.856	1.857	

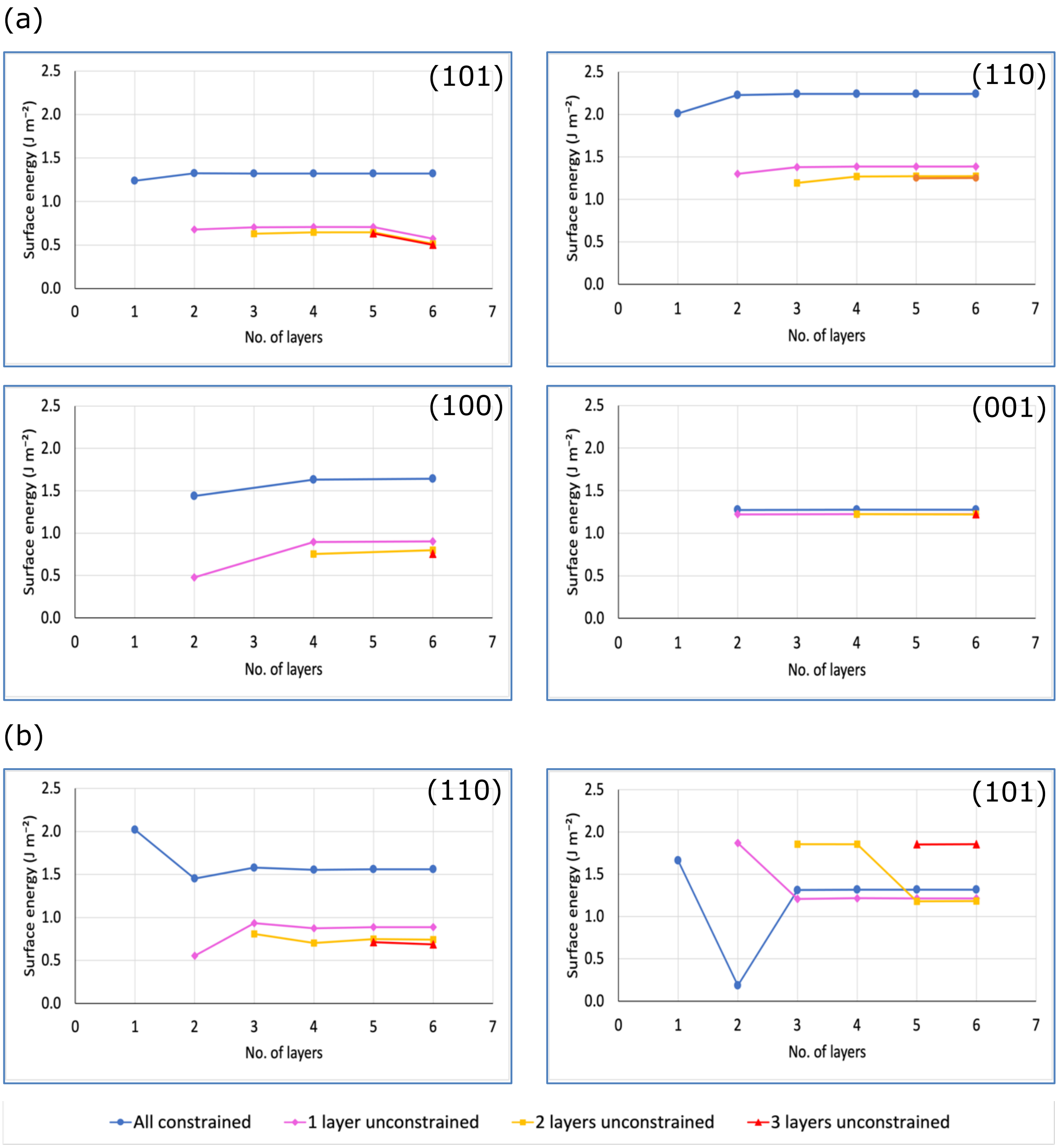

Figure 4.4: The plots of surface energy vs. total number of layers (Ti_2O_4 units) of slab models in different facets of (a) anatase and (b) rutile TiO_2.

According to the Figure 4.4, when varying the thickness up to six Ti_2O_4 layers and constraints up to mid-depth, the surface energy was converged with the top 2-layers unconstrained, 4-layer slab model.

4.3.2 Geometry of different TiO_2 facets

The atomic structure of different facets was investigated as shown in the Figure 4.5 and 4.6 because the interaction of TiO_2 surfaces with guest molecules depends on the coordination of surface ions.[156] The (110) rutile surface is comprised of five- (Ti_{5c}) and six-coordinated (Ti_{6c}) Ti atoms with two- (O_{2c}) and three-coordinated (O_{3c}) O atoms. The (101) rutile surface is composed of Ti_{5c} and O_{2c}. Likewise, both (101) and (100) anatase surfaces are composed of Ti_{5c}, O_{2c} and O_{3c}. The (110) anatase is covered with four-coordinated Ti atoms (Ti_{4c}) and O_{2c}. The (001) anatase surface is terminated with Ti_{5c} with O_{2c}. The relaxation of these surface atoms leads to some displacements of the unconstrained atoms in the top layers of the slab.

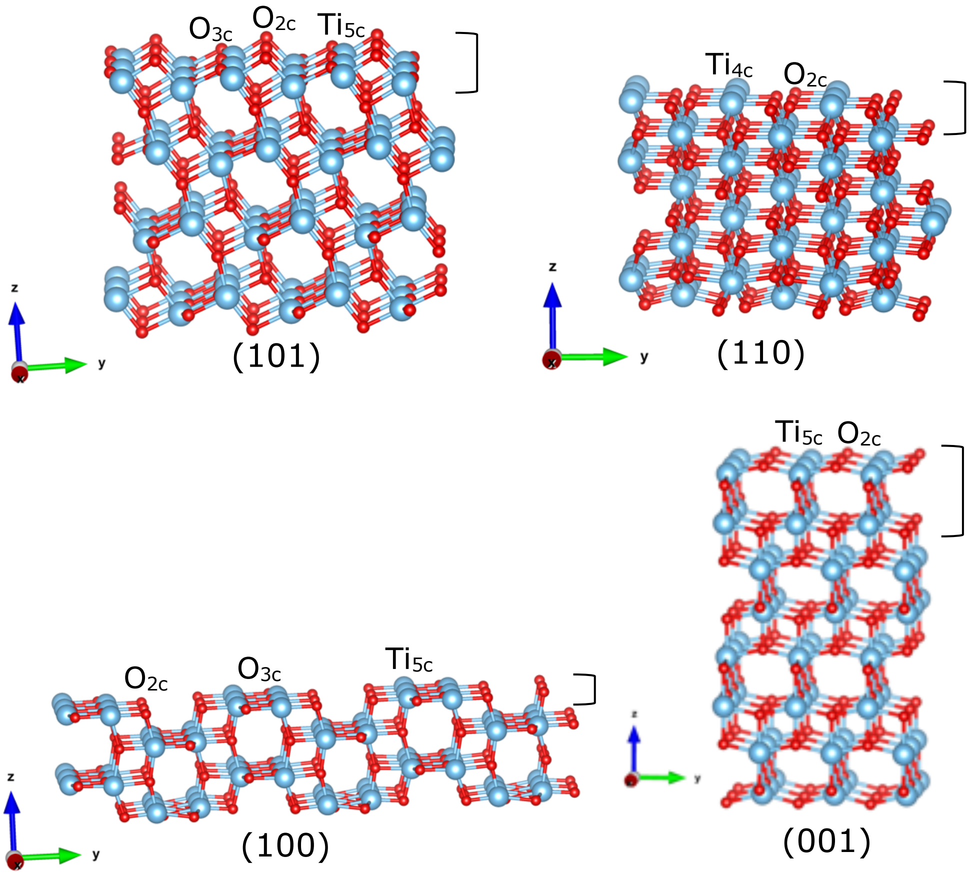

Figure 4.5: The 4-layer (3x3x1) slab models, with top 2-layers unconstrained of facets of anatase TiO_2 where blue and red spheres represent Ti and O atoms respectively. A single layer is indicated with a side bracket in the right-hand side.

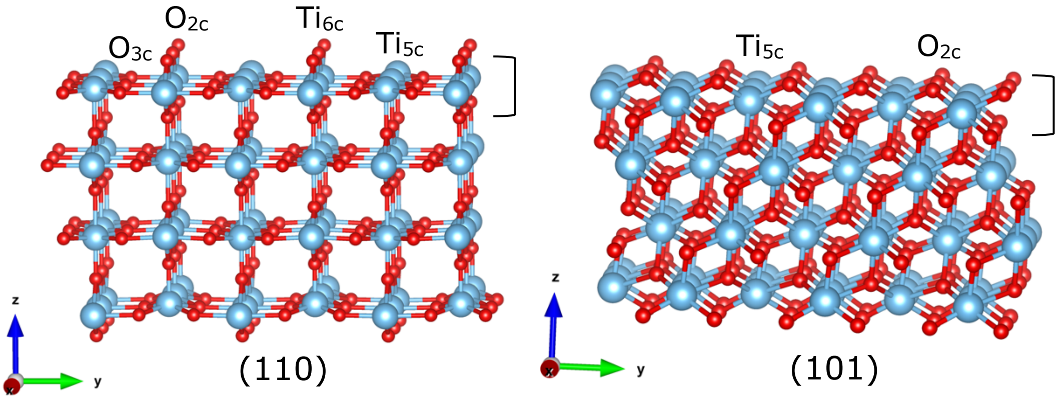

(110)

(101)

Figure 4.6: The 4-layer (3x3x1) slab models, with top 2-layers unconstrained of facets of rutile TiO_2 where blue and red spheres represent Ti and O atoms respectively. A single layer is indicated with a side bracket in the right-hand side.

The most stable (110) rutile surface has a less density of dangling bonds while the (101) anatase surface is formed of an array of troughs and ridges due to the two-coordinated O atoms at the highest level.

The converged slab model with 4-layers, with the top 2 unconstrained, where a vacuum of 20 Å in total exist above and below the surfaces, was used to investigate the relaxations of surface atoms calculated using the equation 4.4. The relaxations of most stable (110) rutile are given in the Table 4.2 referring the atomic index of Figure 4.7 whereas the relaxations of (101) anatase are given in the Table 4.3 referring the atomic index of Figure 4.8. The relaxations of other minority facets are given in the Appendix 3. In the (110) rutile facet, the dominant relaxations are happened along the *z* axis where the undercoordinated Ti moves downward by 0.13 Å, reducing the bond lengths with the atoms in second layer and, six-coordinated Ti atoms and the three-coordinated O atoms are move upward by 0.23 Å and 0.19 Å respectively, giving evidence for the relaxations reported by Ramamoorthy *et al*.[156] In the (101) anatase facet, the dominant relaxations are happened along both *y* and *z* axes. The undercoordinated Ti move upward by 0.17 Å along the *z* axis and move downward by 0.14 Å along the *y* axis whereas Ti move downward by 0.14 Å along the *z* axis. Furthermore, the three-coordinated and two-coordinated O atoms move downward along the *y* axis whilst three-coordinated O atoms move upward in the *z* axis. These results give evidence for the structural rearrangements of surface atoms after slicing from bulk TiO_2 to achieve the minimum energy and stabilise.

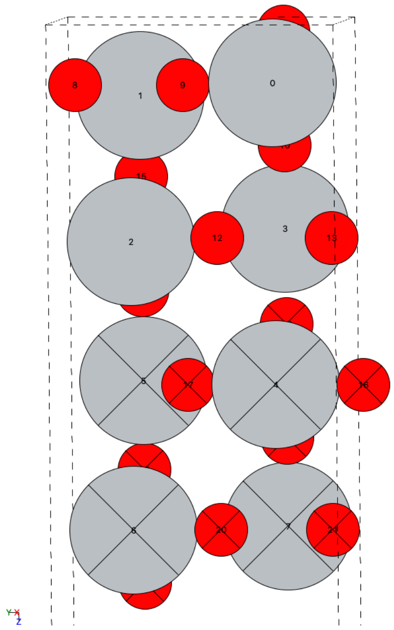

Figure 4.7: The 4-layer slab model, with top 2-layers unconstrained of (110) facet of rutile TiO_2 where a dotted line highlights the conventional unit cell, grey and red spheres represent Ti and O atoms respectively.

Table 4.2: Unrelaxed coordinates (x_1, y_1, z_1), relaxed coordinates (x_2, y_2, z_2), and relaxations (Δx, Δy, Δz) of near-surface atoms of (110) facet of rutile TiO_2 where atom index is referred to Figure 4.7.

(110) Rutile		Unrelaxed coordinates			Relaxed coordinates			Relaxations		
Atom	Atom index	*x*	*y*	*z*	*x*	*y*	*z*	Δ*x*	Δ*y*	Δ*z*
Ti	0	1.474	1.623	1.623	1.474	1.623	1.389	0.000	0.000	-0.234
Ti	1	0.000	4.869	1.623	0.000	4.869	1.753	0.000	0.000	0.130
Ti	2	1.474	4.869	4.869	1.474	4.869	4.925	0.000	0.000	0.056
Ti	3	0.000	1.623	4.869	0.000	1.623	4.715	0.000	0.000	-0.154
O	8	1.474	6.136	1.623	1.474	6.088	1.429	0.000	-0.048	-0.194
O	9	1.474	3.602	1.623	1.474	3.651	1.429	0.000	0.049	-0.194
O	10	0.000	1.623	2.890	0.000	1.623	2.867	0.000	0.000	-0.023
O	11	0.000	1.623	0.356	0.000	1.623	0.323	0.000	0.000	-0.033
O	12	1.474	2.890	4.869	1.474	2.916	4.837	0.000	0.026	-0.032
O	13	1.474	0.356	4.869	1.474	0.331	4.837	0.000	-0.025	-0.032
O	14	0.000	4.869	6.136	0.000	4.869	6.094	0.000	0.000	-0.042
O	15	0.000	4.869	3.602	0.000	4.869	3.555	0.000	0.000	-0.047

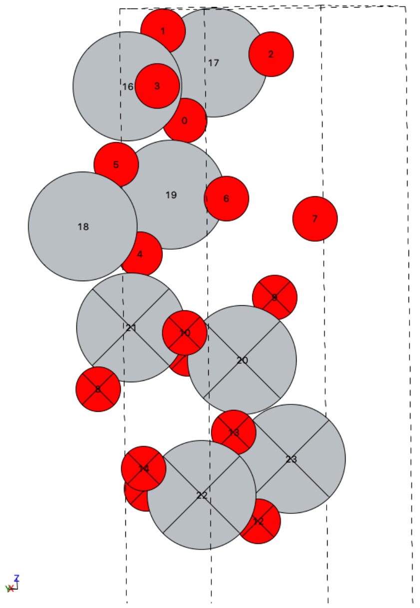

Figure 4.8: The 4-layer slab model, with top 2-layers unconstrained of (101) facet of anatase TiO_2 where a dotted line highlights the conventional unit cell, grey and red spheres represent Ti and O atoms respectively.

Table 4.3: Unrelaxed coordinates (x_1, y_1, z_1), relaxed coordinates (x_2, y_2, z_2), and relaxations (Δx, Δy, Δz) of near-surface atoms of (101) facet of anatse TiO_2 where atom index is referred to Figure 4.8.

(101) Anatase		Unrelaxed coordinates			Relaxed coordinates			Relaxations		
Atom	Atom index	*x*	*y*	*z*	*x*	*y*	*z*	Δ*x*	Δ*y*	Δ*z*
O	0	5.658	3.226	32.179	5.658	3.073	32.130	0.000	-0.153	-0.049
O	1	5.658	3.999	34.510	5.658	3.748	34.496	0.000	-0.251	-0.014
O	2	3.772	1.770	33.633	3.772	1.614	33.855	0.000	-0.156	0.222
O	3	3.772	5.456	33.057	3.772	5.319	33.094	0.000	-0.137	0.037
O	4	5.658	4.608	28.669	5.658	4.591	28.659	0.000	-0.017	-0.010
O	5	5.658	5.381	31.000	5.658	5.305	31.029	0.000	-0.076	0.029
O	6	3.772	3.151	30.123	3.772	3.134	30.111	0.000	-0.017	-0.012
O	7	1.886	1.687	29.547	1.886	1.649	29.559	0.000	-0.038	0.012
Ti	16	5.658	5.073	32.906	5.658	4.928	33.073	0.000	-0.145	0.167
Ti	17	5.658	2.153	33.783	5.658	2.143	33.642	0.000	-0.010	-0.141
Ti	18	5.658	6.454	29.396	5.658	6.432	29.443	0.000	-0.022	0.047
Ti	19	5.658	3.534	30.274	5.658	3.556	30.210	0.000	0.022	-0.064

4.3.3 Electrical properties of different TiO_2 facets

The band gap of the optimised facets using PBEsol functionals and a light basis set is calculated using the equation 2.1 and compared with the reported data as shown in the Table 4.4.

Table 4.4: Calculated band gap (E_g) using PBEsol XC functional and a light basis set and, their difference than the experimental data (ΔE_g). Literature values are highlighted.

	E_{HOMO} (eV)	E_{LUMO} (eV)	Band gap (E_g)	**Band gap (E_g) for HSE06 functional**[154]
(101) anatase	-7.87	-5.95	1.91	**3.4**
(001) anatase	-7.08	-5.73	1.36	**2.6**
(100) anatase	-6.94	-5.34	1.60	**3.3**
(110) anatase	-6.74	-5.23	1.51	**3.4**
Bulk anatase	-9.27	-7.16	2.11	**3.3**
(110) rutile	-7.78	-6.41	1.38	**3.3**
(101) rutile	-6.95	-5.57	1.37	**3.2**
Bulk rutile	-8.88	-7.11	1.77	**3.1**

The band gaps of facets are comparatively lower than the bulk TiO_2 according to the PBEsol functional and those values are clearly underestimates of the band gaps calculated using the HSE06 functional, which are in good agreement with the experimental data.[154] According to the literature, hybrid functionals give more accurate band gap data.[154] Underestimation of the band gaps relative to experiment was also observed for the PBEsol functional in section 3.3.3 as well. Therefore, the band gap energies are not considered in our further work here with the PBESol functional.

4.4 Conclusions

The calculations have shown that the (110) surface of rutile and the (101) anatase have the lowest surface energies with the PBESol functional and thus, highly stable slab models. This agrees with the Wulff construction because those facets contribute to the largest area of the equilibrium structures of both anatase and rutile TiO_2 shown in the Figure 4.1. Additionally, the reported experimental studies also have proven that by discovering that the (110) rutile and (101) anatase are the most stable surface of TiO_2.[133,154,156,157] Moreover, the surface energies are not converged until a considerable number of layers with appropriate constraints are used; in our case, this is with a 4-layer slab model, with the top 2-layers unconstrained. Herein, the 4-layer slab model, with the top 2-layers unconstrained of (110) facet of rutile and the (101) facet of anatase was adopted as the slab model to be used for the further studies of chemical interactions with TiO_2.

CHAPTER 5 - INTERACTION OF TEREPHTHALIC ACID AND METAL SPECIES WITH TiO_2

5.1 Introduction

The chemical and physical properties of surfaces are modified via the controlled chemical functionalisation in modern nanostructuring.[174–177] Several experimental and theoretical studies for functionalisation of metal surfaces such as gold, copper, silver and metal oxide surfaces such as TiO_2, AgO, ZnO, ZrO_2 have been studied using the self-assembled monolayers (SAM) of alkane chains and aromatic rings containing carboxylic acids.[174,178] In that regard, functionalisation of TiO_2 surfaces has been widely investigated towards the applications in optoelectronics, catalysis, sensor fabrication, surface coating, medical usage, etc.[174] The functionalisation of TiO_2 surface allows to produce high-quality, tuneable and stable surfaces in which a monolayer of organic molecules is anchored to TiO_2 surface and acted as the template for on-top build structure.[174,179–182] Most of the functional molecules are linked with the TiO_2 surface using carboxylic acid groups and the remaining functional groups are reacted with the ancillary molecules to result the desired mesoporous structure on TiO_2 surface conferring the improved electrical properties to the whole system.[174,183]

The highly symmetric planar molecule, 1,4 benzenedicarboxylic acid which is known as terephthalic acid or TPA has been received a considerable attention as the prototypical structure for generating a wide range of MOFs due to containing two functional groups.[174,179–182] The MOFs thin films deposited on a desired substrate is known as the SURMOFs (surface-coordinated MOF thin films), which has the advantage of controlling the growth orientation and thickness to maintain the homogeneity. In this regard, TPA has been investigated as a SAM to develop SURMOFs on TiO_2.[174,179–182] Subsequently, the potential syntheses of MOFs can be verified by investigating the interactions of TPA monolayer with metal species. Such TiO_2-SURMOF systems are highly advantageous as the two materials possess different properties while the whole system also shows improved electrical properties due to the possibility of charge transfer over the interface from the adsorbed TPA to TiO_2.[174,179–182]

5.2 Methodology for interactions

An optimised one-sided slab model was considered for studying the molecule adsorption on TiO_2. As finalised from the Section 4.4, the 4-layer slab model, with the top 2-layers unconstrained of (101) facet of anatase and the (110) facet of rutile were used throughout for studying the chemical reactions. Those slab models were repeated periodically in x- and y- directions while the vacuum persists in z-direction to generate the supercell surfaces with an enough area to accommodate different chemical species. The gas-phase model of each chemical species was optimised separately before interacting with the surface model.

5.2.1 Adsorption of terephthalic acid on TiO_2

The 1,4-benzenedicarboxylic acid known as terephthalic acid (TPA)[184] was considered as the prototypical organic linker for the mesoporous materials of interests (Figure 5.1).

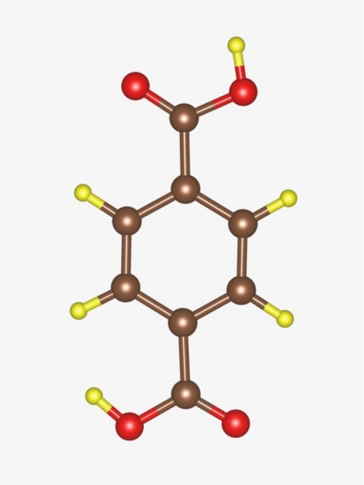

Figure 5.1: Ball and stick model of TPA molecule where brown spheres represent carbon atoms, red spheres represent oxygen atoms and yellow spheres represent hydrogen atoms.

TPA was introduced to the TiO_2 surfaces to interact by mimicking the first step of layer-by-layer MOFs growth on TiO_2. Therefore, orientations of the TPA molecules were decided given the purpose of following an interaction with a metal specie consist of at least two ligands. Four types (a-d) and two types (e-f) of possible starting geometries were considered for the adsorption of TPA molecules on TiO_2 surface in vertical orientation and horizontal orientation respectively as below:

Vertical adsorptions:

Structure A - Vertical adsorption of a single TPA molecule where the H atoms of interacting carboxylic group is attached to TPA

Structure B - Vertical adsorption of closely interacting two TPA molecules in face-to-face orientation where the H atoms of interacting carboxyl groups are in opposite sides and, the H atoms of carboxyl groups interact with the TiO_2 surface are dissociated on to the TiO_2 surface.

Structure C - Vertical adsorption of closely interacting two TPA molecules in side-by-side orientation where the H atoms of interacting carboxyl groups are close to each other and, the H atoms of carboxyl groups interact with the TiO_2 surface are dissociated on to the TiO_2 surface

Structure D - Vertical adsorption of two distant TPA molecules in face-to-face orientation where the H atoms of interacting carboxyl groups are in opposite sides and, the H atoms of carboxyl groups interact with the TiO_2 surface are dissociated on to the TiO_2 surface

Horizontal adsorptions:

Structure E - Horizontal adsorption of a single TPA molecule where the H atoms of interacting carboxylic groups are attached to another TPA

Structure F - Horizontal adsorption of a single TPA molecule where the H atoms of interacting carboxylic groups are dissociated onto the TiO_2 surface

A (4 x 3) supercell model of (101) anatase surface with an area of 233.10 Å^2 along the *xy* plane was used to study the adsorption of one and two TPA molecules; a (4 x 4) supercell model with a surface area of 310.80 Å^2 along the *xy* plane was also used to study the interactions between two distant TPA molecules. Likewise, a (4 x 2) and (4 x 3) supercell models of the (110) rutile surface with a surface area of 156.35 Å^2 and 229.64 Å^2 along the *xy* plane were used to study the interactions with close and distant TPA adsorptions, respectively. A converged 1 x 1 x 1 **k**-grid was used for both (4 x 3) and (4 x 4) supercell models of (101) anatase while, a 2 x 2 x 1 and a 2 x 1 x 1 **k**-grid was used for the (4 x 2) and (4 x 3) supercell models of (110) rutile respectively, which correspond to the $(0.045 \times 2\pi)$ Å^{-1} **k**-point density.

The adsorption energy (E_{ads}) was calculated using the equation:

$$E_{ads} = E_{slab+TPA} - n.E_{surf,rel} - m.E_{TPA} \qquad 5.1$$

where, $E_{slab+TPA}$ is the energy of the combined system, $E_{surf,rel}$ is the total energy of the facet model after relaxation, n is the number of facet models repeated in the supercell, E_{TPA} is the total energy of the optimised gas-phase TPA molecule and, m is the number of TPA molecules.

5.2.2 Interaction of metal species with TiO_2 surface bound TPA

Synthesis of mesoporous materials involves the interaction of the metal species and organic linkers, such as metal chlorides, metal isopropoxides (i-Pr), metal acetates, etc. In this study, anhydrous state of $ZnCl_2$, $TiCl_4$, $ZrCl_4$, $Zn(OH)_2$, $Ti(OH)_4$, $Zr(OH)_4$, $Zn(i\text{-}Pr)_2$, $Ti(i\text{-}Pr)_4$ and $Zr(i\text{-}Pr)_4$ were considered as the interacting metal species with TiO_2 surface bound TPA, assumed as the second step of layer-by-layer MOFs growth on TiO_2. The most stable oxidation state of each metal has been considered. The oxidation state can be defined as the number of electrons that an atom loses or gain when bonding with another atom in a compound. The Three types of models with two TPA molecules bound to TiO_2 surfaces taken from section 5.2.1 were used to study the interactions with metal species as below (a short name to identify each model is mentioned in italics):

(a) H dissociative vertical adsorption of close 2 TPA (face-to-face TPA and H in opposite sides): *Face-to-face close*

(b) H dissociative vertical adsorption of distant 2 TPA (face-to-face TPA and H in opposite sides): *Face-to-face distant*

(c) H dissociative vertical adsorption of close 2 TPA (side-by-side TPA and H in same side): *Side-by-side*

Two ligands of the metal atom were assumed to react with the two H atoms of the carboxylate groups of TPA molecules as shown in the reactions below:

$$[(TiO_2)(TPA)_2] + M\mathrm{Cl}_X \longrightarrow [M\mathrm{Cl}_{X-2}(TiO_2)(TPA)_2] + 2\ \mathrm{HCl} \qquad 5.2$$

$$[(TiO_2)(TPA)_2] + M(\text{i-Pr})_X \longrightarrow [M(\text{i-Pr})_{X-2}(TiO_2)(TPA)_2] + 2\ \text{i-PrH} \qquad 5.3$$

$$[(TiO_2)(TPA)_2] + M(\mathrm{OH})_X \longrightarrow [M(\mathrm{OH})_{X-2}(TiO_2)(TPA)_2] + 2\ H_2O \qquad 5.4$$

where M is the metal species and X is the number of ligands bound to the metal atom. The reaction energy ($E_{reaction}$) was calculated using the equation:

$$E_{reaction} = E_{slab+TPA+MX} + (2.E_{HX}) - E_{slab+TPA} - E_{MX} \qquad 5.5$$

where, $E_{slab+TPA+MX}$ is the energy of whole system, $E_{slab+TPA}$ is the total energy of TPA adsorbed TiO_2 slab model and, E_{MX} is the energy of metal species and E_{HX} is the by-product such as HCl, i-PrH and H_2O.

5.2.3 Mulliken analysis

Mulliken analysis was performed for the systems where metal species interact with TPA bound TiO_2 surfaces. Mulliken analysis produces the electronic occupation of each atom in the system in terms of the basis used. The calculated partial charges of individual atoms were used to analyse charge transfer between the TPA and metal species. According to the literature, Mulliken analysis with small basis sets have been resulted qualitatively reasonable values whereas, ill-defined values are resulted with the completeness of basis set.[101,118] In this study, the charge difference of the metal ions before and after the adsorption with TPA/TiO_2 systems was calculated as below:

$$\Delta q = q_2 - q_1 \qquad 5.6$$

where the change in charge is Δq, the charge of the metal ion before and after the adsorption are q_1 and q_2, respectively.

5.3 Results and discussion

5.3.1 Adsorption of TPA on TiO_2 surface

The adsorption energetics and structural properties of TPA adsorption on anatase and rutile TiO_2 surfaces, as explained in the section 5.2.1, have been investigated. Pristine TiO_2 surfaces can be used to study the adsorption of carboxylic acids because surface defects are not significantly affected, according to the previous literature.[174,185] The adsorption energy for anchoring TPA molecules mimicking the layer-by-layer MOFs growth on TiO_2 surface was calculated using the equation 5.1 and shown in the Table 5.1. The structure of TPA/TiO_2 systems are depicted in Figure 5.2 to Figure 5.5.

Table 5.1: Adsorption energy for the TPA/TiO_2 systems.

TPA/TiO_2 system	Orientation of interacting carboxyl acids and H atoms	Adsorption energy (eV/molecule)	
		Rutile	Anatase
(A) H non-dissociative vertical adsorption of 1 TPA	-	-1.194	-1.132
(B) H dissociative vertical adsorption of close 2 TPA	Face-to-face and H in opposite sides	-2.245	-1.482
(C) H dissociative vertical adsorption of close 2 TPA	Side-by-side and H in same side	-1.982	-1.433
(D) H dissociative vertical adsorption of distant 2 TPA	Face-to-face and H in opposite sides	-2.301	-1.375
(E) H non-dissociative horizontal adsorption of 1 TPA	-	-1.827	-1.137
(F) H dissociative horizontal adsorption of 1 TPA	-	-1.839	-0.447

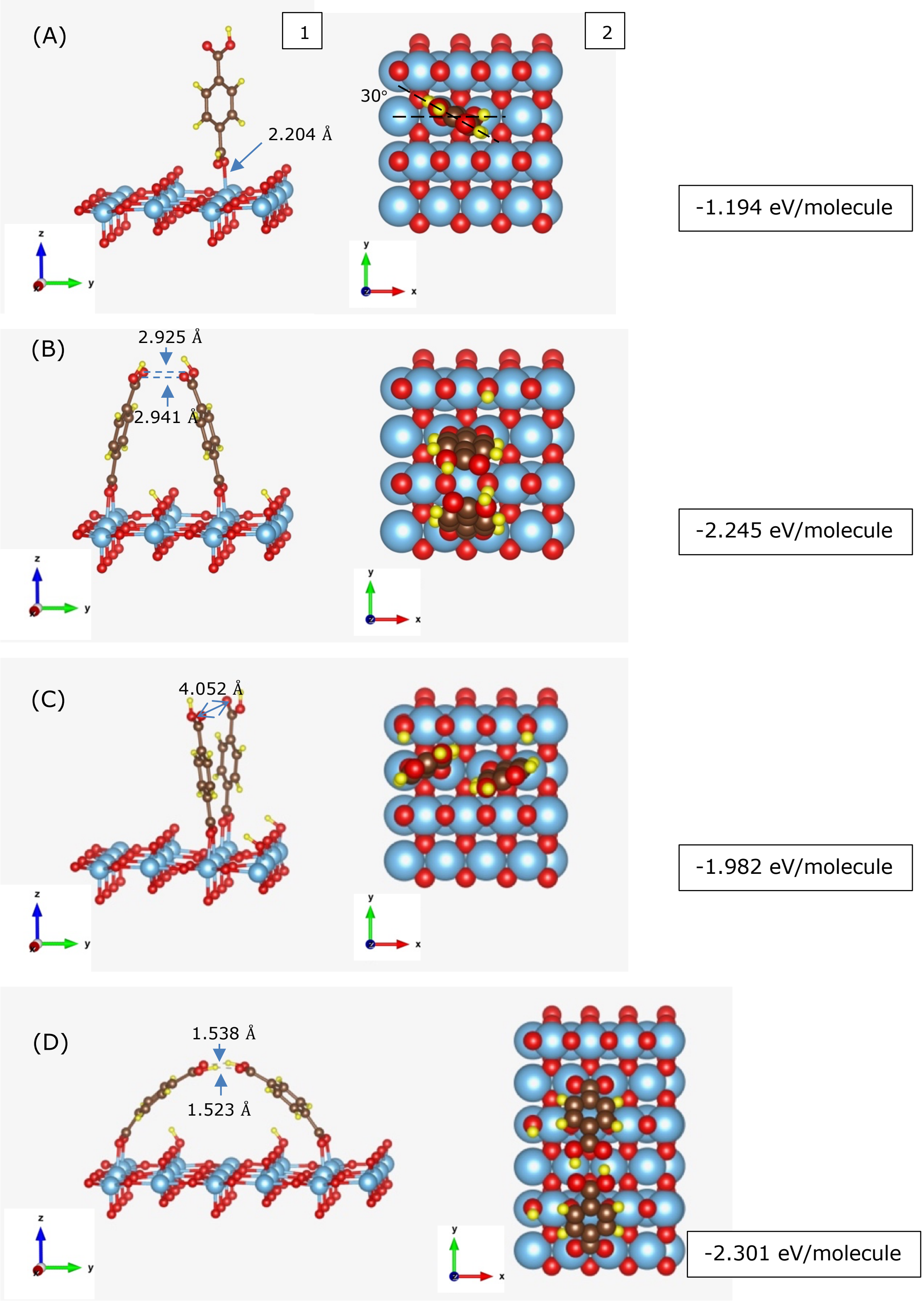

Figure 5.2: Structures of TPA adsorbed on rutile TiO_2 vertically: (1) side view where only top layer is shown and (2) top view of optimised structure. Atoms are coloured as: Ti, blue; O, red; C, brown and H, yellow. Dotted lines in (A) shows the angle for the rotation of TPA during the optimisation. Adsorption energy is mentioned in a box.

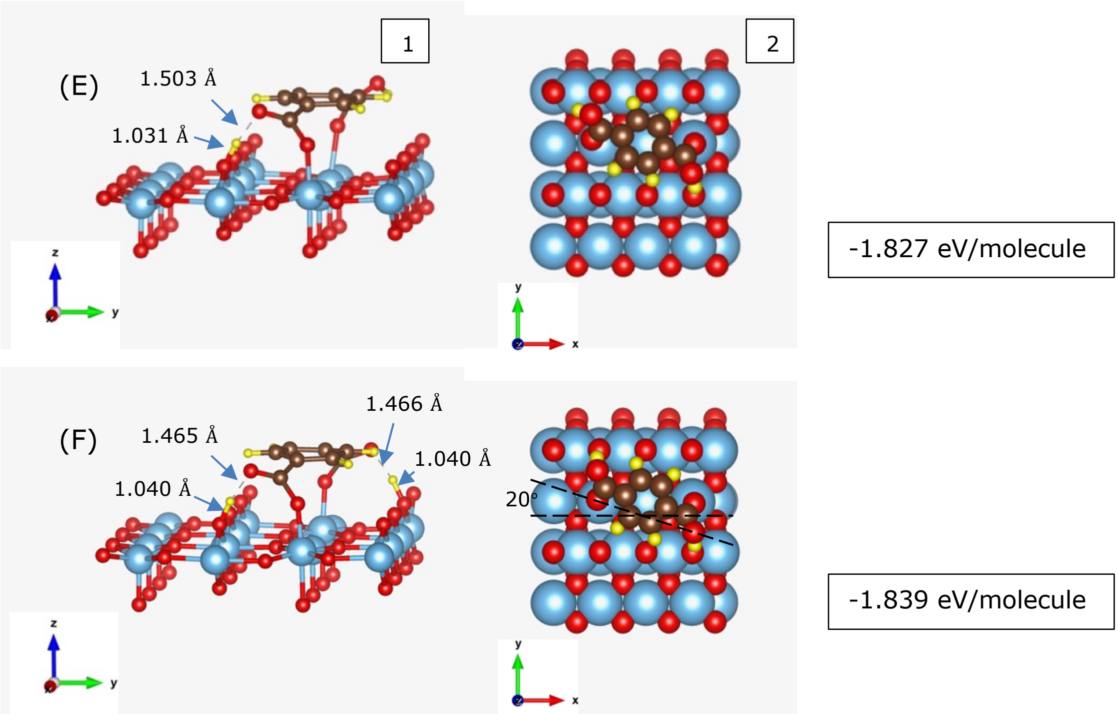

Figure 5.3: Structures of TPA adsorbed on rutile TiO$_2$ horizontally: (1) side view where only top layer is shown and (2) top view of optimised structure. Atoms are coloured as: Ti, blue; O, red; C, brown and H, yellow. Dotted lines in (F) shows the angle for the rotation of TPA during the optimisation. Adsorption energy is mentioned in a box.

TPA molecules interact via the carboxylic groups with the Ti$_{5C}$ ions on (110) rutile surface, which are unsaturated. The TPA molecule in structure *A* shows the highest adsorption energy due to a 30° rotation around the bond between aromatic ring and a surface Ti$_{5C}$ ion when the H of carboxylic group is not dissociated. The structure *D* shows the lowest adsorption energy due to the more favourable anchoring between the carboxylate ions with Ti$_{5C}$ ions on (110) rutile surface as well as due to the favourably interacting top two carboxylic acid groups via hydrogen bonds and van der Waals forces in agreement with reported value -2.35 eV/molecule with PW91 GGA functional.[174] Structure *C* shows a slight rotation of TPA molecules due to the repulsion between the OH parts of nearby carboxyl groups. Structure *E* shows a migration of one H onto the bridging O$_{2C}$ forming a surface hydroxyl group, a ~60° rotation of other carboxylic group and a 20° rotation of the whole molecule, which is the same behaviour reported by Zasada *et al.* with PW91 GGA functional where the values are stated as: O-H is 0.99 Å, O$_{TPA}$-OH$_{surf}$ is 2.21 Å, rotation of the molecule is 19° and adsorption energy is -3.33 eV.[174]

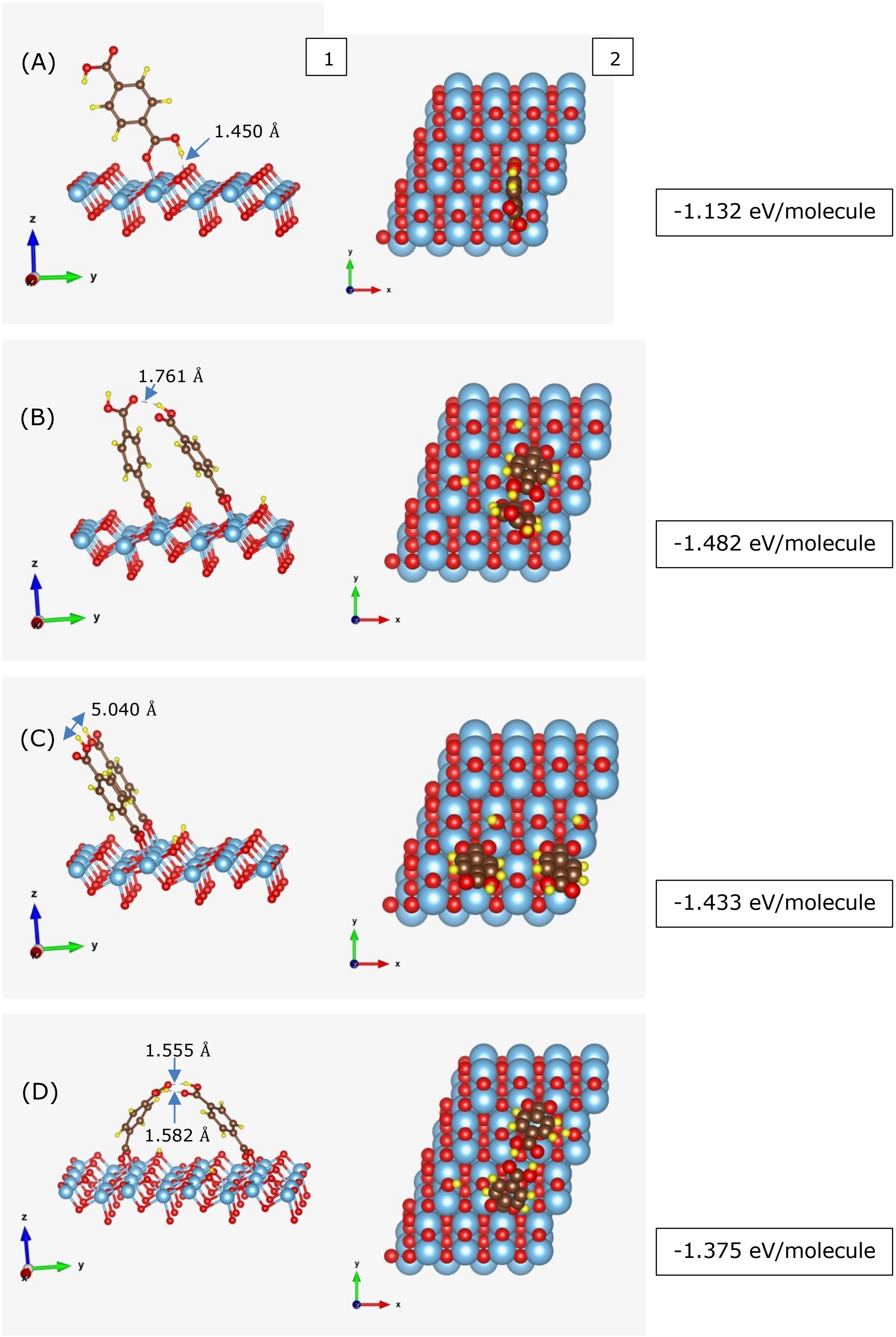

Figure 5.4: Structures of TPA adsorbed on anatase TiO_2 vertically: (1) side view where only top layer is shown and (2) top view of optimised structure. Atoms are coloured as: Ti, blue; O, red; C, brown and H, yellow. Adsorption energy is mentioned in a box.

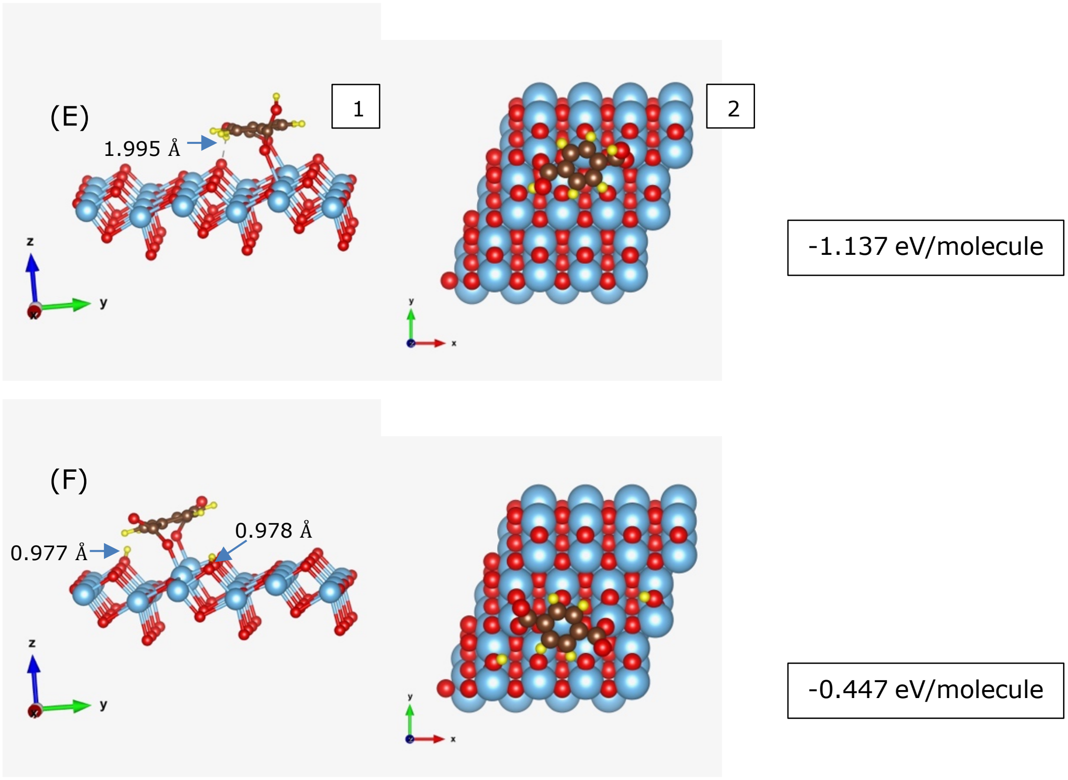

Figure 5.5: Structures of TPA adsorbed on anatase TiO_2 horizontally: (1) side view where only top layer is shown and (2) top view of optimised structure. Atoms are coloured as: Ti, blue; O, red; C, brown and H, yellow. Adsorption energy is mentioned in a box.

TPA molecules interact via the carboxylic groups with the Ti_{5C} ions on (101) anatase surface. The TPA molecule in the structure *F* shows the strongest adsorption energy due to a rotation of carboxylic groups to stabilise on a surface with closely arranged O_{2C} and O_{3C} atoms. The structure *B* shows the weakest adsorption energy due to the more favourable anchoring between the carboxylate ions with Ti_{5C} ions on the anatase surface. Additionally, the top two terminal carboxylic acid groups are interacting via a hydrogen bond. The structure *C* does not show a repulsion between the OH parts of nearby carboxyl groups like in (110) rutile because the large distance of 5.040 Å. Structure *E* does not show a migration of one H onto the surface, but shows the same 90° rotation of one carboxylic group as on (110) rutile surface. Overall, the adsorption energies on the (101) anatase surface are higher than the (110) rutile surface, and vertical adsorptions of TPA molecules tend to bend towards the array of troughs and ridges created by O_{2C}.

5.3.2 Interaction of metal species with TPA functionalised TiO_2 surface

The adsorption energies and structural properties for the interaction of different Zn, Ti and Zr based metal species with the terminal carboxylic groups of TPA adsorbed on anatase and rutile TiO_2 surfaces as explained in the methodology section 5.2.2 have been investigated. The adsorption energy for anchoring TPA on TiO_2 surfaces was calculated using the equation 5.2 and shown in the Table 5.2. Interaction of Zn(II)-based metal species was considered as being fully coordinated with the two H atoms of carboxylic acids of TPA leaving to form separate products. Therefore, the resulting structures consist only of a Zn ion and the respective geometries are given in the Figure 5.6. The structural geometries of other systems are depicted from Figure 5.7 to Figure 5.12.

Table 5.2: Adsorption energy (eV) for the metal species interaction with TPA/TiO_2 systems. Negative adsorption energy values are shown in blue.

Metal species	Adsorption energy (eV)					
	Face-to-Face close TPA		Face-to-Face distant TPA		Side-by-side TPA	
	Rutile	Anatase	Rutile	Anatase	Rutile	Anatase
$ZnCl_2$	2.079	2.372	1.917	1.938	2.446	2.205
$TiCl_4$	-1.323	-1.261	-1.148	-1.306	-1.102	-0.993
$ZrCl_4$	0.657	0.851	0.877	0.708	1.234	1.345
$Zn(OH)_2$	0.231	0.524	0.069	0.090	0.598	0.358
$Ti(OH)_4$	-2.138	-2.041	-1.949	-2.112	-2.029	-1.653
$Zr(OH)_4$	-0.344	-0.133	-0.105	-0.279	0.266	0.334
$Zn(i\text{-}Pr)_2$	0.143	0.436	-0.019	0.002	0.510	0.270
$Ti(i\text{-}Pr)_4$	0.129	0.266	0.271	0.097	0.336	0.494
$Zr(i\text{-}Pr)_4$	-0.248	0.006	0.001	-0.175	0.306	0.451

Face-to-face close

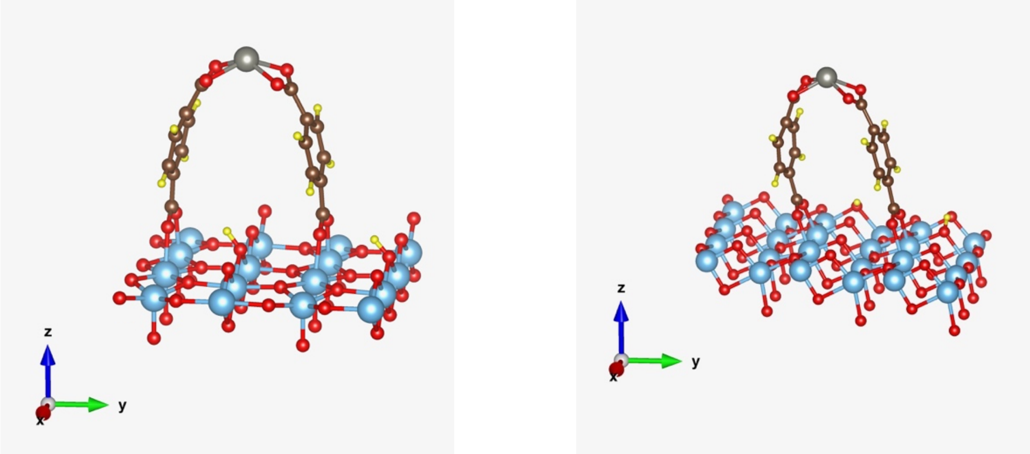

Face-to-face distant

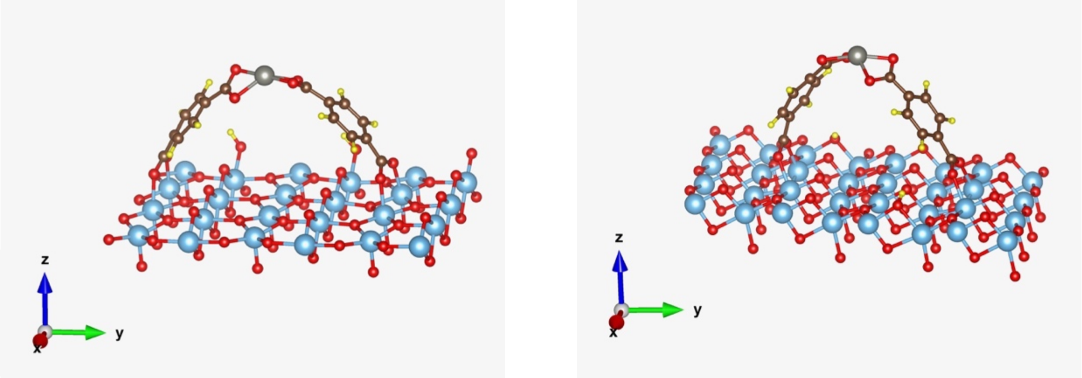

Side-by-side

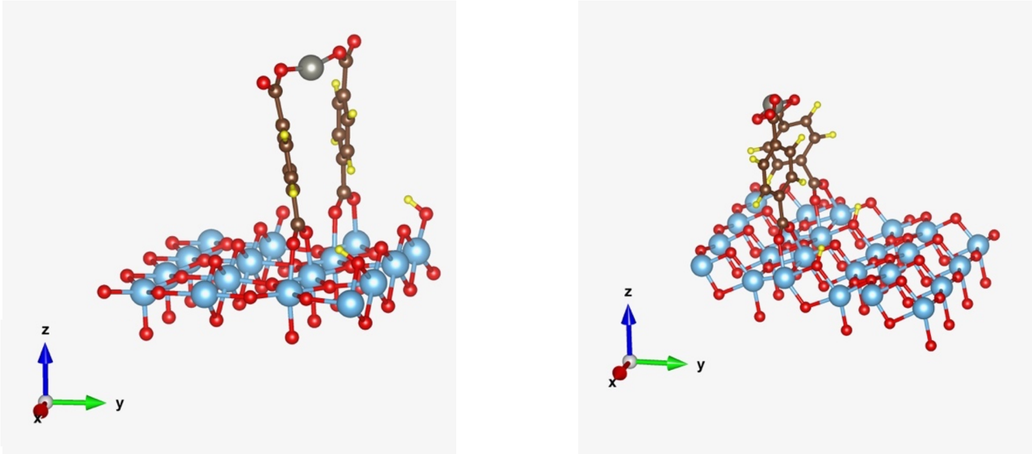

Figure 5.6: Side views of the structures where only top layer is shown for Zn-based metal species interacting with TPA adsorbed on rutile TiO_2 (left) and anatase TiO_2 (right). Atoms are coloured as: Ti, blue; O, red; C, brown; H, yellow and Zn, grey.

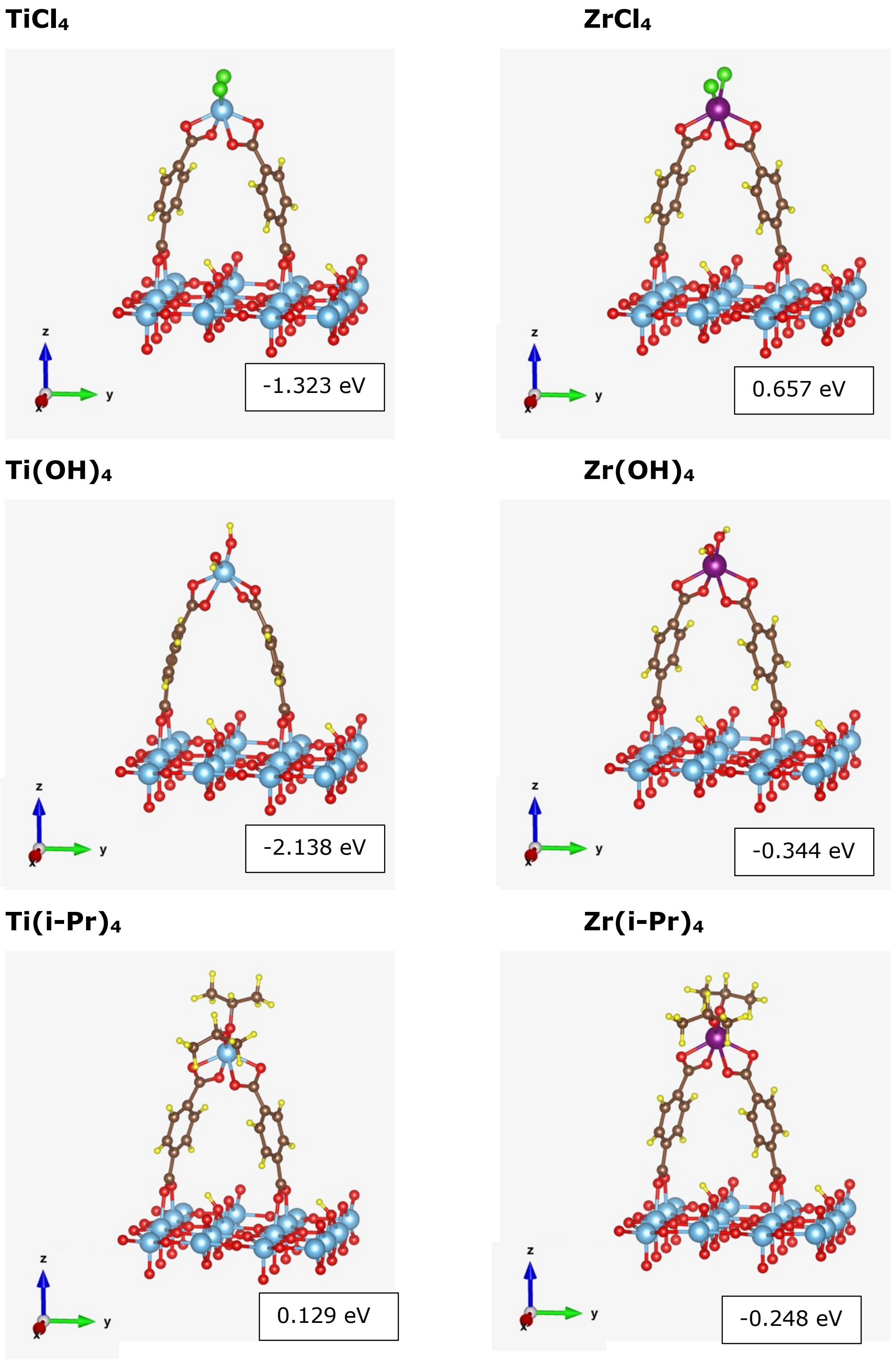

Figure 5.7: Side views of the structures where only top layer is shown for metal species interacting with *face-to-face close* TPA on rutile TiO_2. Atoms are coloured as: Ti, blue; O, red; C, brown; H, yellow; Zn, grey and Zr, purple. Interaction energy is mentioned in a box.

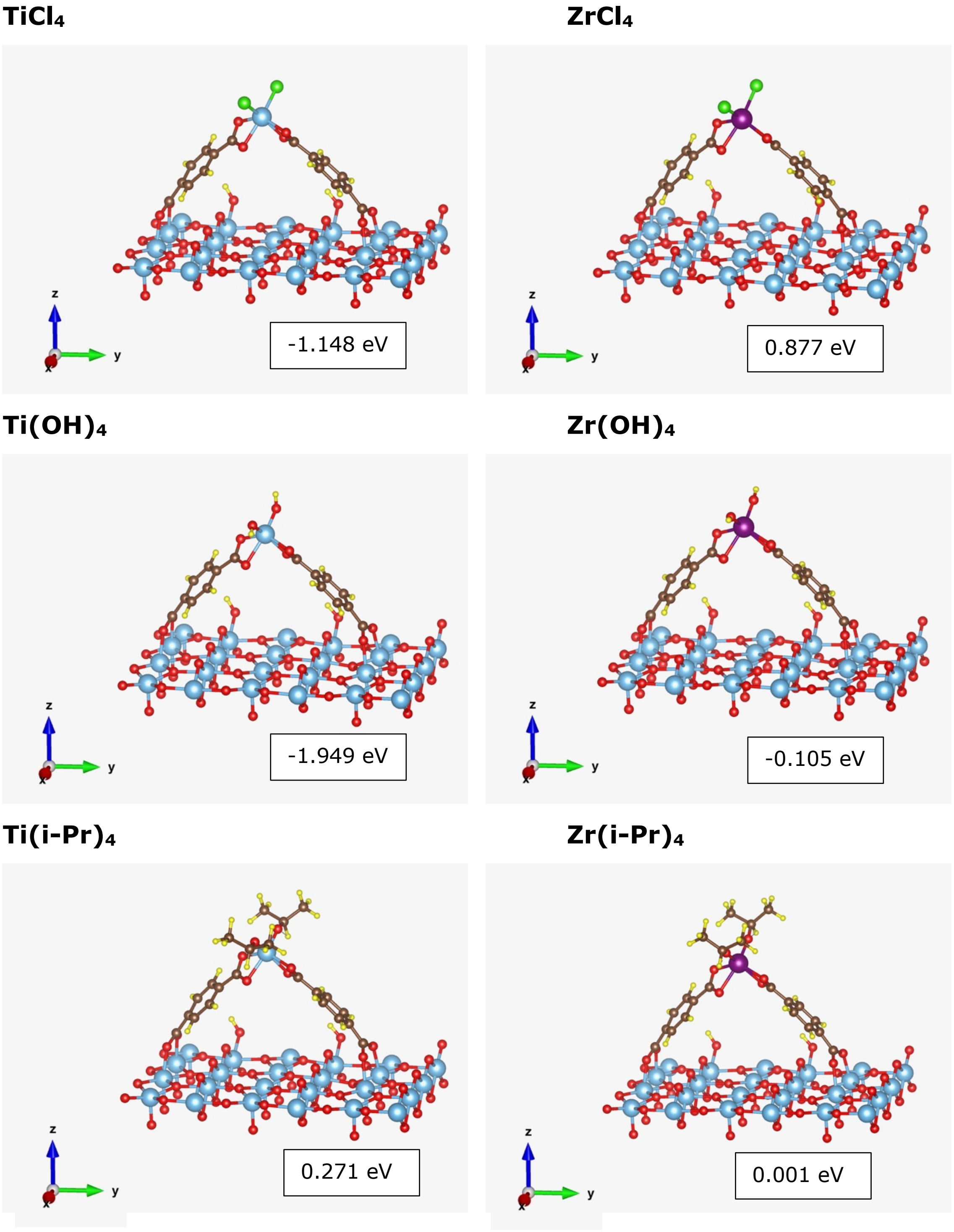

Figure 5.8: Side views of the structures where only top layer is shown for metal species interacting with *face-to-face distant* TPA on rutile TiO_2. Atoms are coloured as: Ti, blue; O, red; C, brown; H, yellow; Zn, grey and Zr, purple. Interaction energy is mentioned in a box.

$TiCl_4$

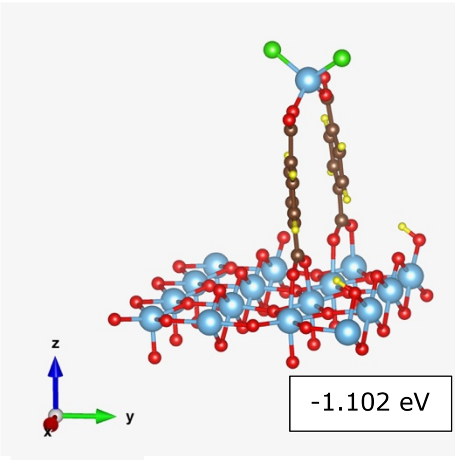

$ZrCl_4$

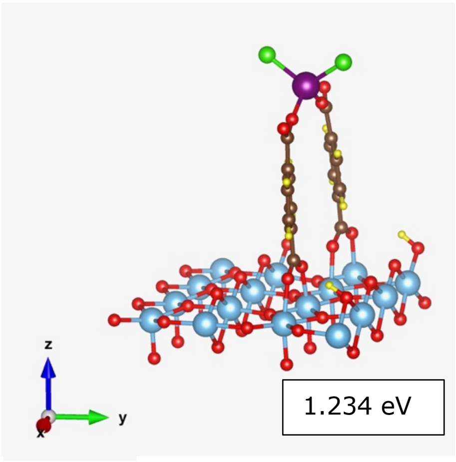

$Ti(OH)_4$

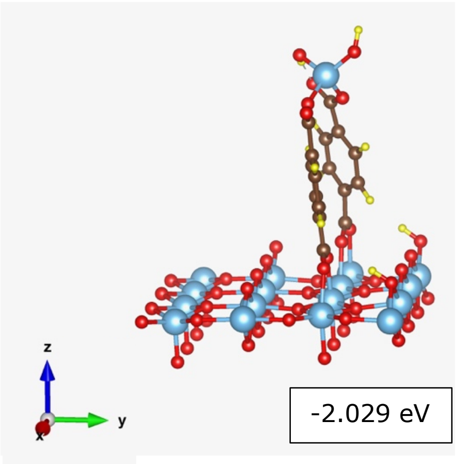

$Zr(OH)_4$

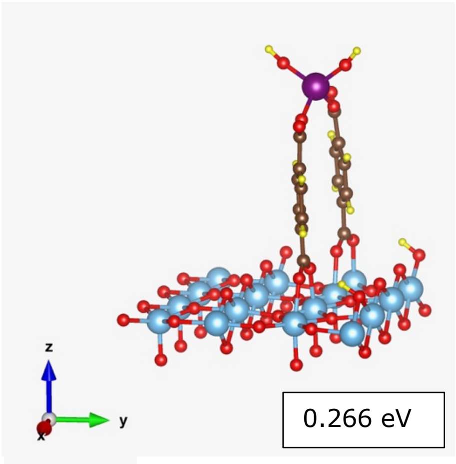

$Ti(i\text{-}Pr)_4$

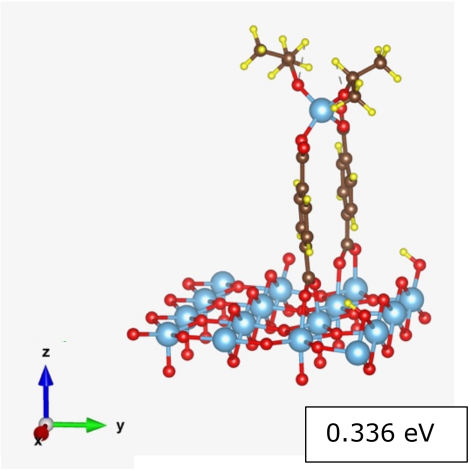

$Zr(i\text{-}Pr)_4$

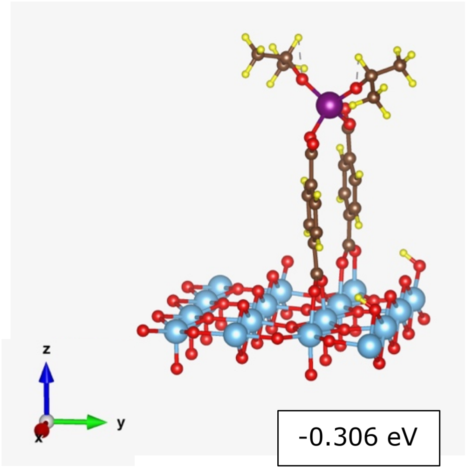

Figure 5.9: Side views of the structures where only top layer is shown for metal species interacting with *side-by-side* TPA on rutile TiO_2. Atoms are coloured as: Ti, blue; O, red; C, brown; H, yellow; Zn, grey and Zr, purple. Interaction energy is mentioned in a box.

TiCl$_4$

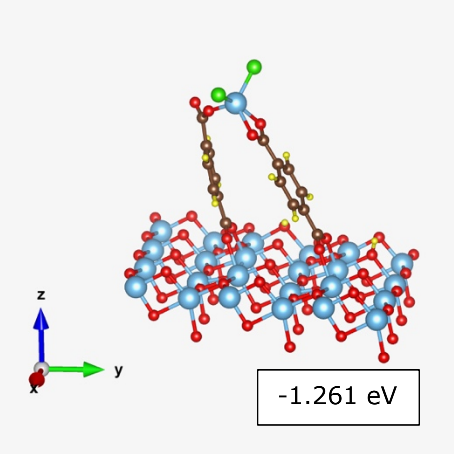

ZrCl$_4$

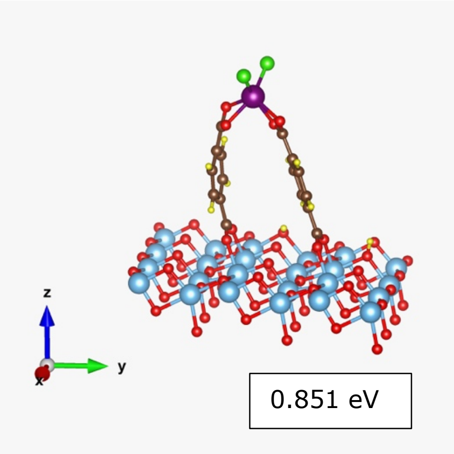

Ti(OH)$_4$

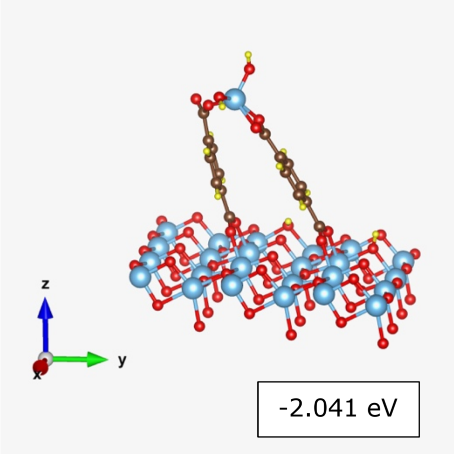

Zr(OH)$_4$

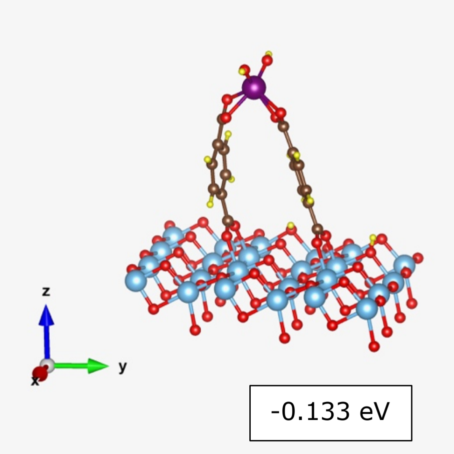

Ti(i-Pr)$_4$

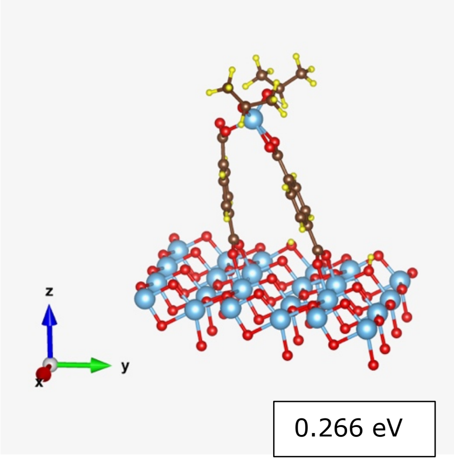

Zr(i-Pr)$_4$

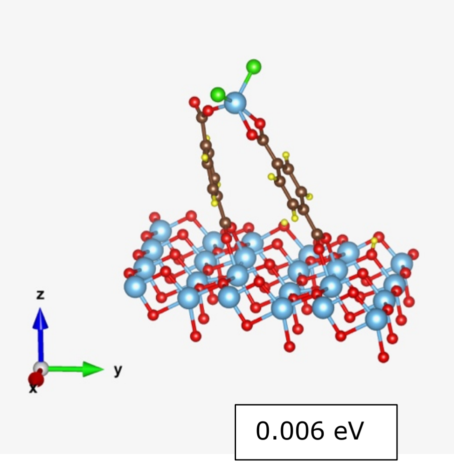

Figure 5.10: Side views of the structures where only top layer is shown for metal species interacting with *face-to-face close* TPA on anatase TiO$_2$. Atoms are coloured as: Ti, blue; O, red; C, brown; H, yellow; Zn, grey and Zr, purple. Interaction energy is mentioned in a box.

$TiCl_4$ **$ZrCl_4$**

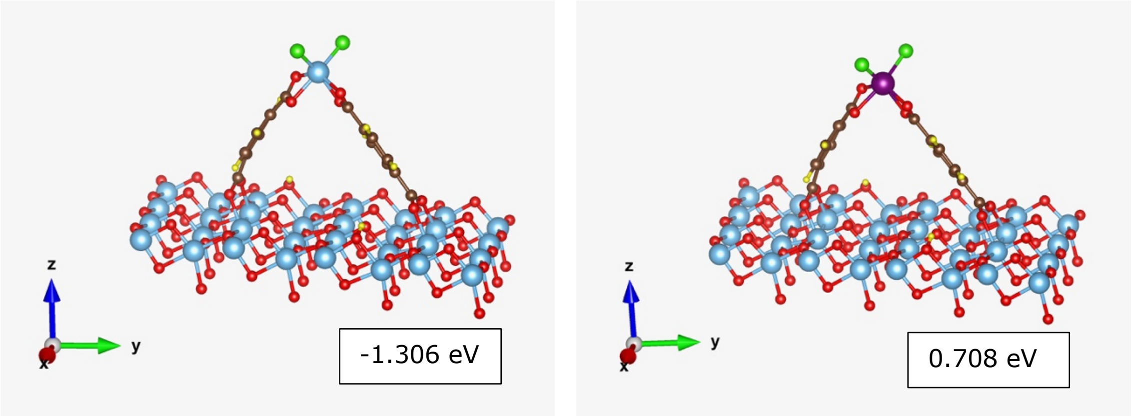

$Ti(OH)_4$ **$Zr(OH)_4$**

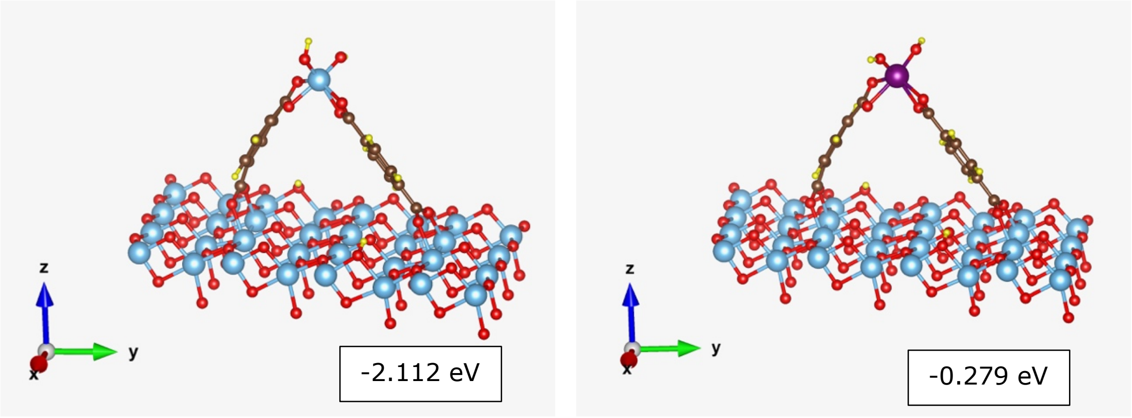

$Ti(i\text{-}Pr)_4$ **$Zr(i\text{-}Pr)_4$**

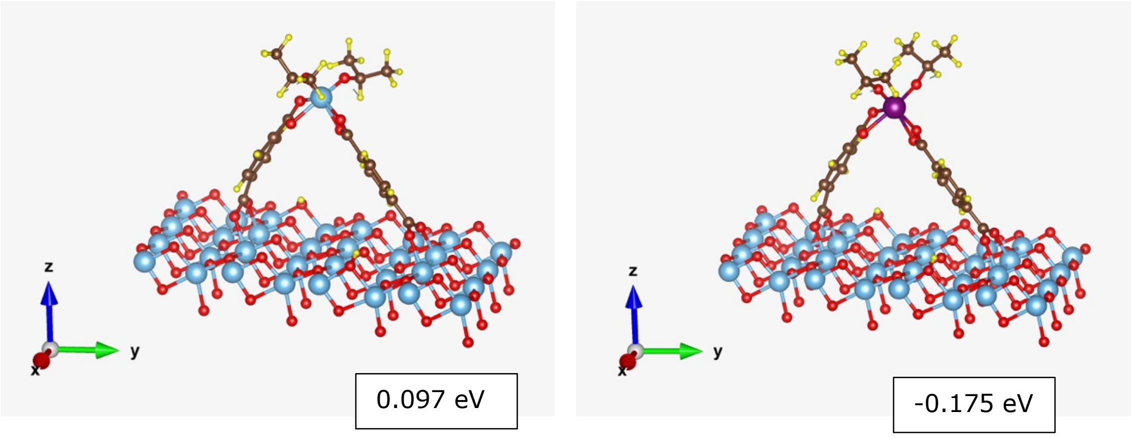

Figure 5.11: Side views of the structures where only top layer is shown for metal species interacting with *face-to-face distant* TPA on anatase TiO_2. Atoms are coloured as: Ti, blue; O, red; C, brown; H, yellow; Zn, grey and Zr, purple. Interaction energy is mentioned in a box.

$TiCl_4$

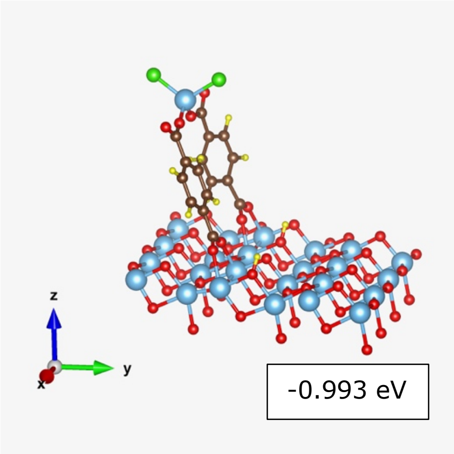

$ZrCl_4$

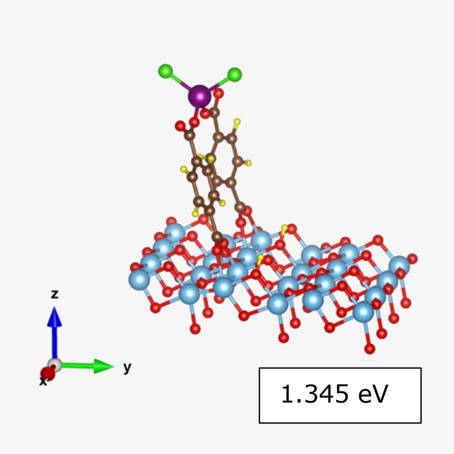

$Ti(OH)_4$

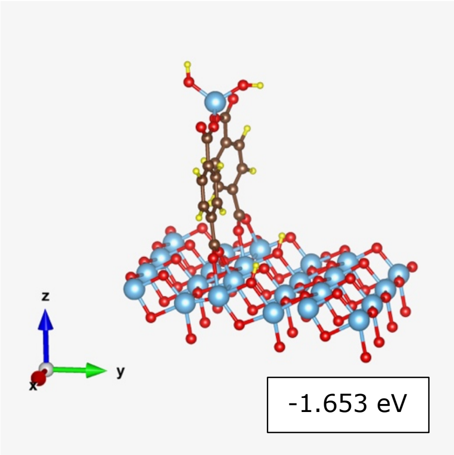

$Zr(OH)_4$

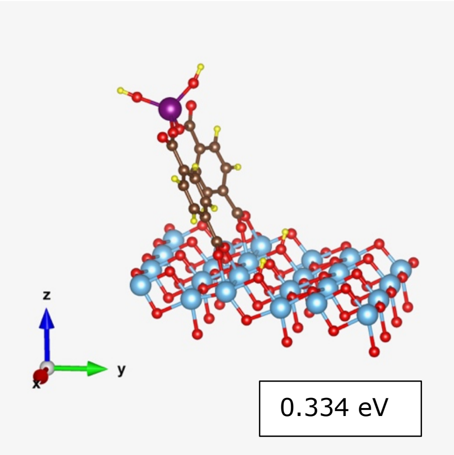

$Ti(i\text{-}Pr)_4$

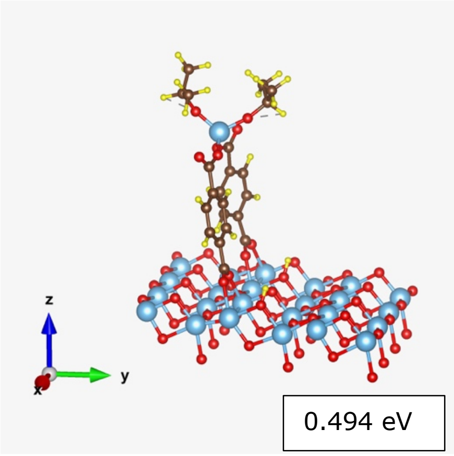

$Zr(i\text{-}Pr)_4$

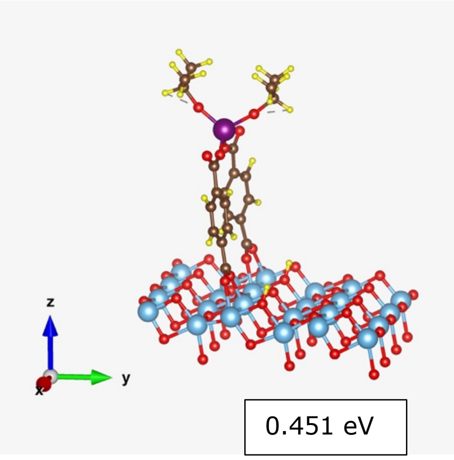

Figure 5.12: Side views of the structures where only top layer is shown for metal species interacting with *side-by-side* TPA on anatase TiO_2. Atoms are coloured as: Ti, blue; O, red; C, brown; H, yellow; Zn, grey and Zr, purple. Interaction energy is mentioned in a box.

The main interaction occurs between the metal species and the terminal carboxylic groups of TPA. The carboxylic groups of TPA are slightly twisted to coordinate with the metal species effectively. Also, the adjacent TPA molecules, which are interacting via the hydrogen bonds, are forced to interact with metal ions to achieve the functionalisation. The adsorption of $TiCl_4$ and $TiOH_4$ on TPA/TiO_2 systems show significantly negative adsorption energies, while $ZrOH_4$ also show negative reaction energies, specifically with the face-to-face orientations. The adsorption of $ZnCl_2$ shows the strongest reaction energies while the adsorption of $Ti(OH)_4$ shows the weakest reaction energies among all the investigated systems. The study done by Zasada *et al.* to observe the interactions between $[(HCOO)Zn]^+$ and the terminal carboxylic groups of TPA dimers on TiO_2 surface has been demonstrated the same behaviours.[174] Those results of reaction energy can be attributed due to the arrangement of geometry. Reactions of Zn-based metal species with *face-to-face* TPA have resulted a square planar geometry and the *side-on-side* TPA have resulted a linear geometry (Figure 5.6). Reactions of $TiCl_4$, $ZrCl_4$, $Ti(OH)_4$, $Zr(OH)_4$, $Ti(i\text{-}Pr)_4$ and $Zr(i\text{-}Pr)_4$ with *face-to-face* TPA have resulted a trigonal prismatic geometry (Figure 5.7, Figure 5.8, Figure 5.10 and Figure 5.11). Reactions of $TiCl_4$, $ZrCl_4$, $Ti(OH)_4$, $Zr(OH)_4$, $Ti(i\text{-}Pr)_4$ and $Zr(i\text{-}Pr)_4$ with *side-on-side* TPA have resulted a tetrahedral geometry (Figure 5.9 and Figure 5.12). Overall, the reaction of TPA adsorbed on TiO_2 surfaces with the metal species are disadvantaged, as the stable intermolecular interactions of adjacent TPA molecules (via hydrogen bonds between the carboxylic groups) means positive adsorption energies exist.[174,186,187]

Calculation of the atomic charges and the charge transfer allows to identify important changes in electronic properties. In this study, the charges of the metal ions before and after the adsorption with TPA/TiO_2 systems were considered as described in the section 5.2.3 to investigate the charge transfer behaviour of the metal ions upon the interaction with terminal carboxylic groups of TPA as shown in the Table 5.3. The Ti(IV) ion of the $TiCl_4$ and $TiOH_4$ adsorbed systems in both face-to-face and side-by-side orientations, the Zr(IV) ion of the $Zr(OH)_4$ adsorbed systems with face-to-face orientation, and the Ti(IV) ion and Zr(IV) of the $Ti(i\text{-}Pr)_4$ and $Zr(i\text{-}Pr)_4$ adsorbed systems with face-to-face orientation show negative charge differences. Therefore, mainly the systems with negative adsorption energies according to Table 5.2 show negative charge differences of the metal ions according to the Table 5.3 giving evidence for the stabilisation of the system due to charge transfer from metal species to the TPA/TiO_2 system.

Table 5.3: Mulliken analysis data for the metal species adsorbed on TPA/TiO_2, where the charge of the metal ion after the adsorption is q and the change in the charge of metal ion after the adsorption is Δq.

Metal species	Face-to-Face close TPA on rutile		Face-to-Face close TPA on anatase		Face-to-Face distant TPA on rutile		Face-to-Face distant TPA on anatase		Side-by-side TPA on rutile		Side-by-side TPA on anatase	
	q (e)	Δq (e)	q (e)	Δq (e)	q (e)	Δq (e)	q (e)	Δq (e)	q (e)	Δq (e)	q (e)	Δq (e)
$ZnCl_2$	0.77	0.17	0.77	0.17	0.77	0.17	0.77	0.17	0.66	0.06	0.73	0.13
$TiCl_4$	0.60	-0.02	0.68	0.06	0.61	-0.01	0.61	-0.01	0.78	0.16	0.79	0.17
$ZrCl_4$	1.03	0.05	1.03	0.04	1.06	0.08	1.06	0.07	1.23	0.24	1.23	0.25
$Zn(OH)_2$	0.77	0.18	0.77	0.18	0.77	0.18	0.77	0.18	0.66	0.07	0.73	0.14
$Ti(OH)_4$	0.79	-0.12	0.84	-0.07	0.79	-0.12	0.79	-0.12	0.91	0.00	0.98	0.06
$Zr(OH)_4$	1.26	-0.15	1.25	-0.16	1.29	-0.12	1.28	-0.13	1.45	0.04	1.45	0.04
$Zn(i\text{-}Pr)_2$	0.77	0.18	0.77	0.17	0.77	0.17	0.77	0.17	0.66	0.07	0.73	0.13
$Ti(i\text{-}Pr)_4$	0.81	-0.11	0.88	-0.04	0.82	-0.10	0.82	-0.10	0.97	0.05	0.96	0.05
$Zr(i\text{-}Pr)_4$	1.26	-0.10	1.26	-0.10	1.28	-0.08	1.28	-0.08	1.40	0.04	1.42	0.06

5.4 Conclusions

The vertical adsorption of TPA after deprotonating the terminal carboxylic acid in which the other terminal carboxylic groups are in face-to-face orientation is concluded as the most favourable way of anchoring TPA molecules on both (110) rutile and (101) anatase TiO_2 surfaces. This can be attributed due to the Van der Waals interaction between the terminal carboxylic acid groups of adjacent TPA molecules as well as the favourable linking between the deprotonated carboxylic group with the Ti_{5C} ions on both surfaces. At low coverages, the adsorption of TPA in horizontal manner after dissociating H atoms from the carboxylic acids on to surface can be expected. The interaction of TPA/TiO_2 systems with metal species to achieve an on-top growth of MOFs is promising, due to the anchoring properties of the terminal carboxylic groups of TPA, with $ZnCl_2$, $TiCl_4$, $ZrCl_4$, $Zn(OH)_2$, $Ti(OH)_4$, $Zr(OH)_4$, $Zn(i\text{-}Pr)_2$, $Ti(i\text{-}Pr)_4$ and $Zr(i\text{-}Pr)_4$ even though a considerable attention needs to be given to overcome the constraints exist due to intermolecular stabilisation of adjacent TPA molecules on TiO_2 surface via hydrogen bonds between the terminal carboxylic groups. Especially, at high coverages of the TiO_2 surface with adsorbed TPA molecules, some constraints exist to the adsorption of chemical species.

CHAPTER 6 - MOF NODES INTERACTON WITH TiO_2 SURFACES

6.1 Introduction

In recent years, the construction of TiO_2-MOF composites has been extensively investigated to achieve enhanced photocatalytic and photovoltaic properties than their original state.[1] TiO_2-MOF composites have great characteristics such as efficient light utilisation by MOFs acting as the photosensitizer, capability of transferring photogenerated electrons directly to metal ions via organic linkers, TiO_2 acts as the primary photocatalyst and MOFs act as co-catalyst.[1] There are several computational studies have been performed to investigate the atomic structure and the energetics of TiO_2 and MOFs even though the studies to understand the nature of hybrid heterointerface of TiO_2-MOF composites have been done to a lesser extent.[188,189] The (100) Zn-MOF-5/(110) rutile TiO_2 interface has been studies using DFT+D calculations by Zasada *et al.* who reported that the Zn-MOF-5 is favourably linked after deprotonating the TPA linkers and the heterointerface can enhance the photoactivity by directly transferring the photoinduced electrons from the Zn-MOF-5 moiety to the CB of TiO_2.[188] The quantum mechanical study done by Bristow *et al.* regarding the growth of (011) Miller index of Zn-MOF-5 on (110) Miller index of rutile TiO_2 also has revealed that the thermodynamically stable bidentate connection is formed between the MOF nodes and TiO_2 surface after deprotonating the TPA and a surface O_{2C} accommodates the leaving proton.[189]

Among numerous types of MOFs, Zn-MOF-5, Ti-MIL-125 and Zr-UiO-66 possess high thermal and chemical stability.[1,190–196] Additionally, the features such as extraordinary porosity, tunability of the pore size and large surface area have made those MOFs use in various applications.[1,190–196] Furthermore, the metal nodes of these MOFs involve in preparation of series of derivatives coordinating with different organic linkers.[1,190–196] This chapter discusses the study focused on the interactions between TiO_2 surfaces and MOFs nodes separated from bulk models of Zn-MOF-5, Ti-MIL-125 and Zr-UiO-66 to investigate the energetics and the structural properties as a simplified version of the TiO_2-MOF heterointerfaces, expecting that the resulting chemical bonding characteristics are relevant to other related TiO_2-MOF composites as well.

6.2 Methodology for interactions

The optimised 4-layer slab models of the anatase (101) facet and the (110) facet of rutile, with top 2-layers unconstrained, were used to investigate the chemical interactions with certain metal nodes of MOFs. Bulk models of Zn-MOF-5, Ti-MIL-125 and Zr-UiO-66 were used from the studies of Allen *et al.,*[197] Smalley *et al.*[198] and Lee *et al.,*[199] respectively, which are built based on X-ray diffraction studies and deposited in the Crystallography Open Database (COD)[200]. A single metal node was separated from the bulk structure and all the TPAs were replaced with formate groups except one TPA, to reduce the computational cost and time when using large MOF nodes with many atoms. The modified metal nodes were optimised in the gas phase before interacting with the rutile and anatase TiO_2 surfaces. Deprotonation of the terminal carboxylic acid group of TPA was considered when linking with the TiO_2 surface assuming that an exposed O_{2C} ion binds with the released proton.

The supercell models of rutile and anatase TiO_2 with adequate surface area were chosen to accommodate the metal nodes and to avoid image interactions. A (4 x 3) supercell model of the (110) rutile surface, with an area of 229.64 $Å^2$, and the (101) anatase surface with an area of 233.10 $Å^2$, along the *xy* plane, were used to study the adsorption of the metal nodes of Zn-MOF-5 and the Zr-UiO-66; for the adsorption of Ti-MIL-125, a (4 x 3) supercell model of the (101) anatase surface and a (6 x 3) supercell model of the (110) rutile surface, with an area of 344.45 $Å^2$ along the *xy* plane was used. A converged 1 x 1 x 1 **k**-grid was used for (4 x 3) supercell model of (101) anatase, while a 2 x 1 x 1 and a 1 x 1 x 1 **k**-grid was used for the (4 x 3) and (6 x 3) supercell models of (110) rutile, respectively, which are corresponded to the $(0.045 \times 2\pi)$ $Å^{-1}$ **k**-point density.

The adsorption energy (E_{ads}) was calculated using the equation:

$$E_{ads} = E_{slab+MN} - n.E_{slab,rel} - E_{MN} \qquad 5.1$$

where, $E_{slab+MN}$ is the energy of the combined system, $E_{slab,rel}$ is the total energy of the facet model after relaxation, n is the number of facet models repeated in the supercell, E_{MN} is the total energy of the optimised gas-phase metal node.

6.3 Results and discussion

The energetics and structural properties of metal nodes adsorbed on anatase and rutile TiO_2 surfaces were calculated as explained in the section 6.2. The structure and the relevant adsorption energy of each system are depicted in Figure 6.1. From section 5.3.1 and the previous studies,[188,189,201] the surface Ti_{5C} ions and the deprotonated TPA linkers are compatible to interact, whereas the O_{2C} ions are available to accommodate the leaving proton. Also, the negative adsorption energies in Figure 6.1 evidence the thermodynamic favourability of the reactions between the metal nodes and the TiO_2 surfaces. The adsorption energy for the Zn-MOF-5 metal node on (110) rutile system is -1.913 eV, whereas the reported value is -2.4 eV with the PW91 GGA XC functional.[188]

Table 6.1 shows the different bond lengths of each model depicted in the Figure 6.1. The two strong Ti_{5C}-O_{TPA} bonds stabilise the metal nodes in vertical orientation on both rutile and anatase TiO_2 surfaces. Also, the Ti_{5C}-O_{TPA} bond lengths change with the metal nodes and the surfaces; the MIL-125 adsorption on rutile and anatase TiO_2 has the shortest and longest Ti_{5C}-O_{TPA} bond lengths as 1.99 Å and 2.12 Å. The metal-O_{TPA} bond lengths, $C_{carboxyl}$-C_{phenyl} bond lengths at the metal node terminal and $C_{carboxyl}$-C_{phenyl} bond lengths near the TiO_2 surface show slight elongations in few angstroms (~0.002 Å), which are not significant. The study by Zasada *et al.* also reported the distance change in $C_{carboxyl}$-C_{phenyl} bond by 0.13 Å in the (100) Zn-MOF-5/(110) rutile interface, due to tilting of the linkers of bulk (100) Zn-MOF-5 as well as the change of Zn-O_{TPA} bond distances as 2.31 Å and 1.95 Å.[188] Tilting of linkers and changing the bond distances occurred when stabilising the MOF nodes or bulk MOF structures, while the structural constraints imposed by the TiO_2 surface exist.[188]

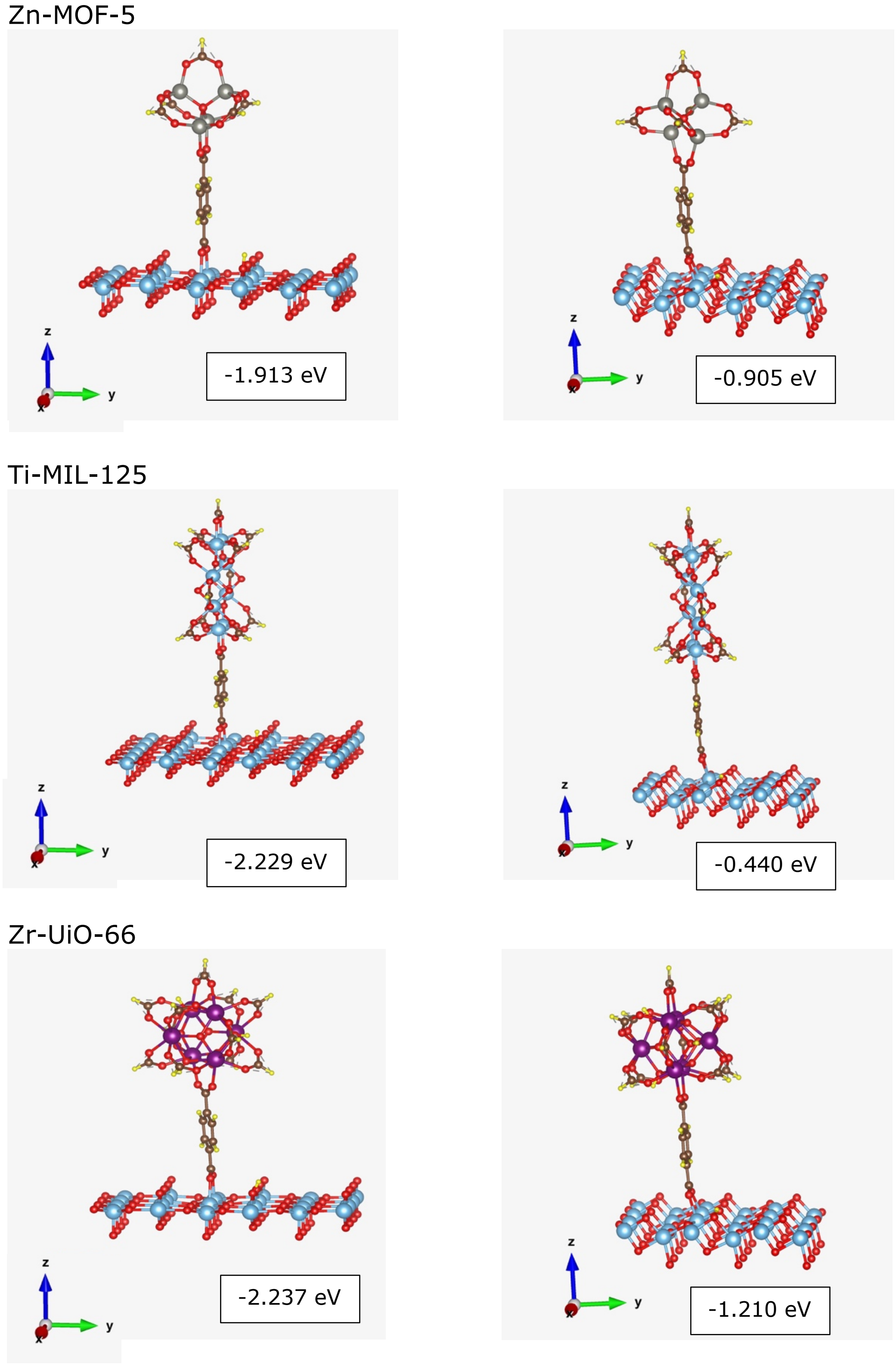

Figure 6.1: Side views of the structures where only top layer is shown for MOF nodes interacting with TPA adsorbed on rutile TiO_2 (left) and anatase TiO_2 (right). Adsorption energy is mentioned in a box. Atoms are coloured as: Ti, blue; O, red; C, brown; H, yellow; Zn, grey and Zr, purple.

Table 6.1: Bond lengths of the TiO_2-MOF systems in Å.

	Zn-MOF-5			Ti-MIL-125			Zr-UiO-66		
	Rutile	Anatase	Metal node in gas phase	Rutile	Anatase	Metal node in gas phase	Rutile	Anatase	Metal node in gas phase
Ti-O_{TPA}	2.002	2.030	-	1.983	2.126	-	2.006	2.005	-
Ti-O_{TPA}	2.001	2.036	-	1.992	2.121	-	1.997	2.058	-
Metal-O_{TPA}	1.944	1.944	1.941	2.074	2.065	2.071	2.217	2.221	2.215
Metal-O_{TPA}	1.944	1.945	1.940	2.072	2.076	2.071	2.227	2.219	2.221
C(carboxyl)-C(phenyl) metal node side	1.496	1.494	1.493	1.493	1.491	1.491	1.495	1.484	1.492
C(carboxyl)-C(phenyl) TiO_2 surface side	1.478	1.484	1.484	1.471	1.470	1.494	1.447	1.494	1.496

6.4 Conclusions

According to the negative adsorption energies obtained for the interaction of Zn-MOF-5, Ti-MIL-125 and Zr-UiO-66 MOF nodes with the TiO_2 surfaces, the MOFs nodes favourably bind with the Ti_{5C} ions of (110) rutile and (101) anatase TiO_2 surfaces. This is evidence for the reported, thermodynamically favourable reaction where MOFs with deprotonated TPA linker constructively interact with the TiO_2 surfaces forming hybrid heterointerfaces.[189] O_{2C} ions on both (110) rutile and (101) anatase TiO_2 surfaces easily accommodate the departing proton from the terminal carboxylic acid group of TPA, facilitating the reaction further. The bond distances of the organic ligands of the MOF node tend to elongate due to the tilting of MOF node to circumvent the structural constraints imposed by the TiO_2, which would need to be addressed when further considering layer-by-layer deposition of MOF nodes on TiO_2, and bulk MOFs interaction with TiO_2.

CHAPTER 7 - CONCLUSIONS AND FUTURE WORK

7.1 Conclusions

The energetics and structures of bulk models and surfaces of rutile and anatase polymorphs of TiO_2, interaction of terephthalic acid (TPA) and metal species with TiO_2, and interaction of metal organic framework (MOF) nodes with TiO_2 have investigated in this research. The obtained results have been validated by comparing with the reported computational and experimental observations where possible.

In Chapter 3, formation energies, molecular structures, and band gap of bulk rutile and anatase polymorphs of TiO_2 have calculated using a range of XC functionals, validated with the previously reported data and, identified that the PBEsol XC functional with a light basis set is the most appropriate setting to discover the functionalisation of TiO_2 to deliver new composites.

In Chapter 4, surface energies, geometric and electrical properties have been investigated with (110) and (101) facets for rutile TiO_2 and (101), (001), (100) and (110) facets for anatase TiO_2. A converged 4-layer slab model, with the top 2-layers unconstrained of (110) facet of rutile and the (101) facet of anatase TiO_2 were selected as the best models to study the chemical interactions with TPA.

Chapter 5 details calculations of the adsorption of TPA on to (110) rutile and (101) anatase TiO_2 surfaces and also the interaction of Zn(II), Ti(IV) and Zr(IV) based metal chlorides, hydroxides and isopropoxides with already adsorbed TPA on the TiO_2 surfaces. The results proved that the adsorption of TPA on to TiO_2 is highly favourable after dissociating the terminal hydrogen of TPA. The leaving hydrogen is accommodated by the O_{2C} ions on the TiO_2 surface whereas TPA binds with the surface Ti_{5C} ions. The interaction of metal species with TPA is promising due to the linking properties of terminal carboxylic acid even though there is a slight constraint due to the Van der Waals interactions between the terminal carboxylic acid groups of nearby TPA molecules.

Finally, Chapter 6 looks at the interaction of TPA-coordinated MOF nodes of Zn-MOF-5, Ti-MIL-125 and Zr-UiO-66 with (110) rutile and (101) anatase.

Likewise, the TPA adsorption on to TiO_2 surface, the deprotonation of terminal carboxylic acid of TPA linker facilitates the adsorption of such MOF nodes on to TiO_2 surface.

Overall, the layer-by-layer MOFs growth using TPA followed by metal species or using already formed MOF nodes is highly favourable on both (110) rutile and (101) anatase TiO_2 surfaces because of the anchoring properties of the terminal carboxylic acid groups of TPA as well as the availability of Ti_{5C} and O_{2C} ions on the TiO_2 surface to accommodate TPA molecules and the departing protons, respectively.

7.2 Future work

Given the scope of work covered in this study, there are numerous options for further research. Various organic ligands (i.e., 1,3,5-benzenetricarboxylate, 1,4-benzenedipyrazolate, imidazolate) and metal species [i.e., Cr(II), Co(II), Fe(II)] are involved in synthesis for a diverse number of investigated MOFs to date.[1,78–80] Exploration of the MOFs growth using such different reaction components should be done to understand the chemical bonding at the TiO_2-MOF interface and consequences for applications.

The bulk crystal structures of different MOFs are widely available from X-ray diffraction studies. Different MOF nodes and crystal facets can be generated utilising such bulk crystal structures to be interacted with the TiO_2 surfaces; although the most stable (110) rutile and (101) anatase TiO_2 surfaces were used in this study, exploration with the higher energy facets is also necessary to better understand the formation and nature of the TiO_2-MOF interfaces. Additionally, the TiO_2 surfaces are commonly hydroxylated, which will ultimately change the adsorptions. Therefore, investigation of MOFs adsorption on hydroxylated TiO_2 surfaces can be done for further understanding of the TiO_2-MOF interface.

Moreover, Chapter 3 explains the high accuracy of band gap data with the HSE06 hybrid XC functional. Therefore, investigation of band gap energy, HOMO and LUMO to explore the photo-induced behaviours (i.e., LMCT, MLCT and π–π* transition in the organic ligands comprising aromatic ring[1,78–80]) of these materials are recommended to further study the photovoltaic properties of TiO_2-MOF composites.

REFERENCES

1 C. C. Wang, X. Wang and W. Liu, *Chem. Eng. J.*, 2020, **391**, 123601–123637.

2 K. Nakata and A. Fujishima, *J. Photochem. Photobiol. C Photochem. Rev.*, 2012, **13**, 169–189.

3 S. Sun, P. Song, J. Cui and S. Liang, *Catal. Sci. Technol.*, 2019, **9**, 4198–4215.

4 T. Peng and J. A. Lalman, *TiO_2 Nanomaterials for Enhanced Photocatalysis*, American Chemical Society, 2019.

5 X. Hu, X. Hu, Q. Peng, L. Zhou, X. Tan, L. Jiang, C. Tang, H. Wang, S. Liu, Y. Wang and Z. Ning, *Chem. Eng. J.*, 2020, **380**, 122366–122376.

6 S. Shen, J. Chen, M. Wang, X. Sheng, X. Chen, X. Feng and S. S. Mao, *Prog. Mater. Sci.*, 2018, **98**, 299–385.

7 W. Liu, J. Ni and X. Yin, *Water Res.*, 2014, **53**, 12–25.

8 M. Janczarek, Ł. Klapiszewski, P. Jędrzejczak, I. Klapiszewska, A. Ślosarczyk and T. Jesionowski, *Chem. Eng. J.*, 2022, **430**, 132062–132089.

9 J. Schneider, M. Matsuoka, M. Takeuchi, J. Zhang, Y. Horiuchi, M. Anpo and D. W. Bahnemann, *Chem. Rev.*, 2014, **114**, 9919–9986.

10 L. Bai, S. Wang, Z. Wang, E. Hong, Y. Wang, C. Xia and B. Wang, *Environ. Pollut.*, 2019, **248**, 516–525.

11 N. Rahimi, R. A. Pax and E. M. A. Gray, *Prog. Solid State Chem.*, 2016, **44**, 86–105.

12 N. Rahimi, R. Pax and E. M. A. Gray, *Prog. Solid State Chem.*, 2019, **55**, 1–19.

13 J. P. Zou, Y. Chen, S. S. Liu, Q. J. Xing, W. H. Dong, X. B. Luo, W. L. Dai, X. Xiao, J. M. Luo and J. Crittenden, *Water Res.*, 2019, **150**, 330–339.

14 J. Luo, S. Zhang, M. Sun, L. Yang, S. Luo and J. C. Crittenden, *ACS Nano*, 2019, **13**, 9811–9840.

15 M. Wang, L. Chen, S. Pan, C. Mou, K. Shi and Z. Chen, *Infect. Genet. Evol.*, 2019, **69**, 1–7.

16 X. Zheng, S. Xu, Y. Wang, X. Sun, Y. Gao and B. Gao, *J. Colloid Interface Sci.*, 2018, **527**, 202–213.

17 F. Han, V. S. R. Kambala, M. Srinivasan, D. Rajarathnam and R. Naidu, *Appl. Catal. A Gen.*, 2009, **359**, 25–40.

18 Y. Sheng, Z. Wei, H. Miao, W. Yao, H. Li and Y. Zhu, *Chem. Eng. J.*, 2019, **370**, 287–294.

19 Y. Zhang, L. Li, Y. Liu, T. Feng, S. Xi, X. Wang, C. Xue, J. Qian and G. Li, *Chem. Sci.*, 2019, **10**, 8323–8330.

20 Q. Sun, X. Hu, S. Zheng, J. Zhang and J. Sheng, *Environ. Pollut.*, 2019, **245**, 53–62.

21 N. Liu, Q. Zhu, N. Zhang, C. Zhang, N. Kawazoe, G. Chen, N. Negishi and Y. Yang, *Environ. Pollut.*, 2019, **247**, 847–856.

22 W. Liu, Y. Li, F. Liu, W. Jiang, D. Zhang and J. Liang, *Water Res.*, 2019, **151**, 8–19.

23 A. Dawson and P. V. Kamat, *J. Phys. Chem. B*, 2001, **105**, 960–966.

24 J. M. Rehm, G. L. McLendon, Y. Nagasawa, K. Yoshihara, J. Moser and M. Grätzel, *J. Phys. Chem.*, 1996, **100**, 9577–9578.

25 D. Robert, *Catal. Today*, 2007, **122**, 20–26.

26 D. R. Baker and P. V. Kamat, *Adv. Funct. Mater.*, 2009, **19**, 805–811.

27 Q. Dai and J. Rabani, *J. Photochem. Photobiol. A Chem.*, 2002, **148**, 17–24.

28 A. Zaban, O. I. Mićić, B. A. Gregg and A. J. Nozik, *Langmuir*, 1998, **14**, 3153–3156.

29 F. De Angelis, *Acc. Chem. Res.*, 2014, **47**, 3349–3360.

30 S. George, S. Pokhrel, Z. Ji, B. L. Henderson, T. Xia, L. Li, J. I. Zink, A. E. Nel and L. Mädler, *J. Am. Chem. Soc.*, 2011, **133**, 11270–11278.

31 E. Stathatos, P. Lianos, P. Falaras and A. Siokou, *Langmuir*, 2000, **16**, 2398–2400.

32 V. Iliev, D. Tomova, L. Bilyarska and G. Tyuliev, *J. Mol. Catal. A Chem.*, 2007, **263**, 32–38.

33 S. Linic, P. Christopher and D. B. Ingram, *Nat. Mater. 2011 1012*, 2011, **10**, 911–921.

34 A. V. Rupa, D. Manikandan, D. Divakar and T. Sivakumar, *J. Hazard. Mater.*, 2007, **147**, 906–913.

35 Z. Cai, X. Hao, X. Sun, P. Du, W. Liu and J. Fu, *Water Res.*, 2019, **162**, 369–382.

36 L. Wang, X. Gao, J. Su, Q. Zhang, K. Zheng and Z. Zhang, *J. Photochem. Photobiol. A Chem.*, 2019, **383**, 111973–111982.

37 K. Vinodgopal and P. V. Kamat, *Environ. Sci. Technol.*, 2002, **29**, 841–

845.

38 X. Wang, J. Yu, C. Fu, T. Li and H. Yu, *Appl. Surf. Sci.*, 2019, **494**, 740–748.

39 S. Mallakpour, V. Behranvand and F. Mallakpour, *Carbohydr. Polym.*, 2019, **224**, 115138–115148.

40 Z. Cai, A. D. Dwivedi, W. N. Lee, X. Zhao, W. Liu, M. Sillanpää, D. Zhao, C. H. Huang and J. Fu, *Environ. Sci. Nano*, 2018, **5**, 27–47.

41 W. Tao, M. Wang, R. Ali, S. Nie, Q. Zeng, R. Yang, W. M. Lau, L. He, H. Tang and X. Jian, *Appl. Surf. Sci.*, 2019, **495**, 143435–143442.

42 Q. Chen, L. Chen, J. Qi, Y. Tong, Y. Lv, C. Xu, J. Ni and W. Liu, *Chinese Chem. Lett.*, 2019, **30**, 1214–1218.

43 C. Huang, M. Zhu, L. Kang, X. Li and B. Dai, *Chem. Eng. J.*, 2014, **242**, 69–75.

44 Y. Li, S. Zhang, Q. Yu and W. Yin, *Appl. Surf. Sci.*, 2007, **253**, 9254–9258.

45 X. Wu, S. Yin, Q. Dong, C. Guo, H. Li, T. Kimura and T. Sato, *Appl. Catal. B Environ.*, 2013, **142**–**143**, 450–457.

46 S. Sampath, H. Uchida and H. Yoneyama, *J. Catal.*, 1994, **149**, 189–194.

47 S. Anandan and M. Yoon, *J. Photochem. Photobiol. C Photochem. Rev.*, 2003, **4**, 5–18.

48 S. H. Liu and W. X. Lin, *J. Hazard. Mater.*, 2019, **368**, 468–476.

49 S. Fukahori, H. Ichiura, T. Kitaoka and H. Tanaka, *Environ. Sci. Technol.*, 2003, **37**, 1048–1051.

50 M. J. Gázquez, J. P. Bolívar, R. Garcia-Tenorio, F. Vaca, M. J. Gázquez, J. P. Bolívar, R. Garcia-Tenorio and F. Vaca, *Mater. Sci. Appl.*, 2014, **5**, 441–458.

51 A. J. Haider, Z. N. Jameel and I. H. M. Al-Hussaini, *Energy Procedia*, 2019, **157**, 17–29.

52 J. Muscat, V. Swamy and N. M. Harrison, *Phys. Rev. B*, 2002, **65**, 224112–224126.

53 M. Mattesini, J. S. De Almeida, L. Dubrovinsky, N. Dubrovinskaia, B. Johansson and R. Ahuja, *Phys. Rev. B - Condens. Matter Mater. Phys.*, 2004, **70**, 1–4.

54 V. Swamy and B. C. Muddle, *Phys. Rev. Lett.*, 2007, **98**, 035502–035505.

55 L. Koči, D. Y. Kim, J. S. De Almeida, M. Mattesini, E. Isaev and R. Ahuja, *J. Phys. Condens. Matter*, 2008, **20**, 345218–345224.

56 J. Dewhurst and J. Lowther, *Phys. Rev. B*, 1996, **54**, 3673–3675.

57 N. A. Dubrovinskaia, L. S. Dubrovinsky, R. Ahuja, V. B. Prokopenko, V. Dmitriev, H. P. Weber, J. M. Osorio-Guillen and B. Johansson, *Phys. Rev. Lett.*, 2001, **87**, 275501–275504.

58 D. Nishio-Hamane, A. Shimizu, R. Nakahira, K. Niwa, A. Sano-Furukawa, T. Okada, T. Yagi and T. Kikegawa, *Phys. Chem. Miner. 2009 373*, 2009, **37**, 129–136.

59 X. F. Zhou, X. Dong, G. R. Qian, L. Zhang, Y. Tian and H. T. Wang, *Phys. Rev. B - Condens. Matter Mater. Phys.*, 2010, **82**, 060102–060105.

60 H. Sato, S. Endo, M. Sugiyama, T. Kikegawa, O. Shimomura and K. Kusaba, *Science (80-.).*, 1991, **251**, 786–788.

61 L. Gerward and J. S. Olsen, *J. Am. Ceram. Soc.*, 1997, **30**, 259–264.

62 A. J. Bard, *J. Phys. Chem.*, 2002, **86**, 172–177.

63 H. C. Choi, H. J. Ahn, Y. M. Jung, M. K. Lee, H. J. Shin, S. Bin Kim and Y. E. Sung, *Appl. Spectrosc.*, 2004, **58**, 598–602.

64 N. Serpone, D. Dondi and A. Albini, *Inorganica Chim. Acta*, 2007, **360**, 794–802.

65 H. Yamashita, M. Harada, J. Misaka, M. Takeuchi, B. Neppolian and M. Anpo, *Catal. Today*, 2003, **84**, 191–196.

66 X. Chen, *Chinese J. Catal.*, 2009, **30**, 839–851.

67 G. P. Dransfield, *Radiat. Prot. Dosimetry*, 2000, **91**, 271–273.

68 E. Şennik, Z. Çolak, N. Kilinç and Z. Z. Öztürk, *Int. J. Hydrogen Energy*, 2010, **35**, 4420–4427.

69 A. Jaroenworaluck, N. Pijarn, N. Kosachan and R. Stevens, *Chem. Eng. J.*, 2012, **181–182**, 45–55.

70 G. K. Mor, O. K. Varghese, M. Paulose, K. G. Ong and C. A. Grimes, *Thin Solid Films*, 2006, **496**, 42–48.

71 R. D. Shannon and J. A. Pask, *J. Am. Ceram. Soc.*, 1965, **48**, 391–398.

72 M. Lazzeri, A. Vittadini and A. Selloni, *Phys. Rev. B*, 2001, **63**, 155409–155417.

73 A. Dhakshinamoorthy and H. Garcia, *Chem. Soc. Rev.*, 2014, **43**, 5750–5765.

74 S. Furukawa, J. Reboul, S. Diring, K. Sumida and S. Kitagawa, *Chem.*

Soc. Rev., 2014, **43**, 5700–5734.

75 F. Bella, R. Bongiovanni, R. S. Kumar, M. A. Kulandainathan and A. M. Stephan, *J. Mater. Chem. A*, 2013, **1**, 9033–9036.

76 S. L. Li and Q. Xu, *Energy Environ. Sci.*, 2013, **6**, 1656–1683.

77 Y. Li, A. Pang, C. Wang and M. Wei, *J. Mater. Chem.*, 2011, **21**, 17259–17264.

78 T. Zhang and W. Lin, *Chem. Soc. Rev.*, 2014, **43**, 5982–5993.

79 X. Yan, S. Komarneni, Z. Zhang and Z. Yan, *Microporous Mesoporous Mater.*, 2014, **183**, 69–73.

80 D. Banerjee, C. M. Simon, A. M. Plonka, R. K. Motkuri, J. Liu, X. Chen, B. Smit, J. B. Parise, M. Haranczyk and P. K. Thallapally, *Nat. Commun. 2016 71*, 2016, **7**, 1–7.

81 N. Liu, X. Chen, J. Zhang and J. W. Schwank, *Catal. Today*, 2014, **225**, 34–51.

82 J. Tian, Z. Zhao, A. Kumar, R. I. Boughton and H. Liu, *Chem. Soc. Rev.*, 2014, **43**, 6920–6937.

83 J. Zhang, P. Zhou, J. Liu and J. Yu, *Phys. Chem. Chem. Phys.*, 2014, **16**, 20382–20386.

84 R. Kaplan, B. Erjavec, G. Dražić, J. Grdadolnik and A. Pintar, *Appl. Catal. B Environ.*, 2016, **181**, 465–474.

85 S. Liu, J. Yu and M. Jaroniec, *Chem. Mater.*, 2011, **23**, 4085–4093.

86 A. Meng, J. Zhang, D. Xu, B. Cheng and J. Yu, *Appl. Catal. B Environ.*, 2016, **198**, 286–294.

87 N. Roy, Y. Sohn and D. Pradhan, *ACS Nano*, 2013, **7**, 2532–2540.

88 J. Yu, J. Low, W. Xiao, P. Zhou and M. Jaroniec, *J. Am. Chem. Soc.*, 2014, **136**, 8839–8842.

89 J. Pan, G. Liu, G. Q. Lu and H. M. Cheng, *Angew. Chemie Int. Ed.*, 2011, **50**, 2133–2137.

90 R. Daghrir, P. Drogui and D. Robert, *Ind. Eng. Chem. Res.*, 2013, **52**, 3581–3599.

91 M. Pelaez, N. T. Nolan, S. C. Pillai, M. K. Seery, P. Falaras, A. G. Kontos, P. S. M. Dunlop, J. W. J. Hamilton, J. A. Byrne, K. O’Shea, M. H. Entezari and D. D. Dionysiou, *Appl. Catal. B Environ.*, 2012, **125**, 331–349.

92 J. Zhang, Y. Wu, M. Xing, S. A. K. Leghari and S. Sajjad, *Energy Environ. Sci.*, 2010, **3**, 715–726.

93 W. Wang, M. O. Tadé and Z. Shao, *Prog. Mater. Sci.*, 2018, **92**, 33–63.

94 K. Song, J. Zhou, J. Bao and Y. Feng, *J. Am. Ceram. Soc.*, 2008, **91**, 1369–1371.

95 M. Malekshahi Byranvand, A. Nemati Kharat, L. Fatholahi and Z. Malekshahi Beiranvand, *J. Nanostructures*, 2013, **3**, 1–9.

96 Z. Zhao, J. Tian, Y. Sang, A. Cabot and H. Liu, *Adv. Mater.*, 2015, **27**, 2557–2582.

97 Y. C. Nah, I. Paramasivam and P. Schmuki, *ChemPhysChem*, 2010, **11**, 2698–2713.

98 P. Roy, S. Berger and P. Schmuki, *Angew. Chemie Int. Ed.*, 2011, **50**, 2904–2939.

99 M. Cargnello, T. R. Gordon and C. B. Murray, *Chem. Rev.*, 2014, **114**, 9319–9345.

100 J. A. Pople, P. M. W. Gill and B. G. Johnson, *Chem. Phys. Lett.*, 1992, **199**, 557–560.

101 V. Blum, R. Gehrke, F. Hanke, P. Havu, V. Havu, X. Ren, K. Reuter and M. Scheffler, *Comput. Phys. Commun.*, 2009, **180**, 2175–2196.

102 A. Hjorth Larsen, J. JØrgen Mortensen, J. Blomqvist, I. E. Castelli, R. Christensen, M. Dułak, J. Friis, M. N. Groves, B. Hammer, C. Hargus, E. D. Hermes, P. C. Jennings, P. Bjerre Jensen, J. Kermode, J. R. Kitchin, E. Leonhard Kolsbjerg, J. Kubal, K. Kaasbjerg, S. Lysgaard, J. Bergmann Maronsson, T. Maxson, T. Olsen, L. Pastewka, A. Peterson, C. Rostgaard, J. SchiØtz, O. Schütt, M. Strange, K. S. Thygesen, T. Vegge, L. Vilhelmsen, M. Walter, Z. Zeng and K. W. Jacobsen, *J. Phys. Condens. Matter*, 2017, **29**, 273002–273060.

103 K. Choudhary and F. Tavazza, *Comput. Mater. Sci.*, 2019, **161**, 300–308.

104 W. P. Huhn and V. Blum, *Phys. Rev. Mater.*, 2017, **1**, 033803–033820.

105 Y. Zhang, J. W. Furness, B. Xiao and J. Sun, *J. Chem. Phys.*, 2019, **150**, 014105–014110.

106 L. Chiodo, J. M. García-Lastra, A. Iacomino, S. Ossicini, J. Zhao, H. Petek and A. Rubio, *Phys. Rev. B - Condens. Matter Mater. Phys.*, 2010, **82**, 045207–045218.

107 H. Cui, H. Liu, J. Shi and C. Wang, *Int. J. Photoenergy*, 2013, **2013**, 1–16.

108 J. Schneider, M. Matsuoka, M. Takeuchi, J. Zhang, Y. Horiuchi, M. Anpo and D. W. Bahnemann, *Chem. Rev.*, 2014, **114**, 9919–9986.

109 Y. Nam, J. H. Lim, K. C. Ko and J. Y. Lee, *J. Mater. Chem. A*, 2019, **7**,

13833–13859.

110 J. Chen, F. Qiu, W. Xu, S. Cao and H. Zhu, *Appl. Catal. A Gen.*, 2015, **495**, 131–140.

111 F. De Angelis, *Acc. Chem. Res.*, 2014, **47**, 3349–3360.

112 M. Horn, C. F. Schwebdtfeger and E. P. Meagher, *Zeitschrift für Krist. - Cryst. Mater.*, 1972, **136**, 273–281.

113 D. M. Tobaldi, A. Tucci, A. S. Škapin and L. Esposito, *J. Eur. Ceram. Soc.*, 2010, **30**, 2481–2490.

114 W. Li, C. Ni, H. Lin, C. P. Huang and S. I. Shah, *J. Appl. Phys.*, 2004, **96**, 6663–6668.

115 W. S. Morgan, J. J. Jorgensen, B. C. Hess and G. L. W. Hart, *Comput. Mater. Sci.*, 2018, **153**, 424–430.

116 P. Kratzer and J. Neugebauer, *Front. Chem.*, 2019, **7**, 1–18.

117 J. Hermann and A. Tkatchenko, *Phys. Rev. Lett.*, 2020, **124**, 146401–146407.

118 X. Ren, P. Rinke, V. Blum, J. Wieferink, A. Tkatchenko, A. Sanfilippo, K. Reuter and M. Scheffler, *New J. Phys.*, 2012, **14**, 053020–053074.

119 D. M. Ceperley and B. J. Alder, *Phys. Rev. Lett.*, 1980, **45**, 566–569.

120 R. Armiento and A. E. Mattsson, *Phys. Rev. B - Condens. Matter Mater. Phys.*, 2005, **72**, 085108–085112.

121 J. P. Perdew, K. Burke and M. Ernzerhof, *Phys. Rev. Lett.*, 1996, **77**, 3865–3868.

122 J. P. Perdew, A. Ruzsinszky, G. I. Csonka, O. A. Vydrov, G. E. Scuseria, L. A. Constantin, X. Zhou and K. Burke, *Phys. Rev. Lett.*, 2008, **100**,

136406–136409.

123 B. Hammer, L. B. Hansen and J. K. Nørskov, *Phys. Rev. B*, 1999, **59**, 7413–7421.

124 Y. Zhao and D. G. Truhlar, *J. Chem. Phys.*, 2006, **125**, 194101–194118.

125 J. Sun, A. Ruzsinszky and J. Perdew, *Phys. Rev. Lett.*, 2015, **115**, 036402–036407.

126 J. Wellendorff, K. T. Lundgaard, K. W. Jacobsen and T. Bligaard, *J. Chem. Phys.*, 2014, **140**, 144107–144116.

127 P. J. Stephens, F. J. Devlin, C. F. Chabalowski and M. J. Frisch, *J. Phys. Chem.*, 1994, **98**, 11623–11627.

128 J. Heyd, G. E. Scuseria and M. Ernzerhof, *J. Chem. Phys.*, 2003, **118**, 8207–8215.

129 C. Adamo and V. Barone, *J. Chem. Phys.*, 1999, **110**, 6158–6170.

130 Y. Zhao and D. G. Truhlar, *Theor. Chem. Acc.*, 2007, **120**, 215–241.

131 A. Jain, S. P. Ong, G. Hautier, W. Chen, W. D. Richards, S. Dacek, S. Cholia, D. Gunter, D. Skinner, G. Ceder and K. A. Persson, *APL Mater.*, 2013, **1**, 11002–11011.

132 R. D. Hoffman, S. E. Woosley, Y.-Z. Qian, S. Zenitani, M. Hesse and A. Klimas, *Proc. Phys. Soc.*, 1962, **80**, 783–786.

133 B. Ohler, S. Prada, G. Pacchioni and W. Langel, *J. Phys. Chem. C*, 2012, **117**, 358–367.

134 A. Vegas, J. Mejía-López, A. H. Romero, M. Kiwi, D. Santamaría-Pérez and V. G. Baonza, *Solid State Sci.*, 2004, **6**, 809–814.

135 J. Liu, X. Fan, C. Sun and W. Zhu, *RSC Adv.*, 2016, **6**, 71311–71318.

136 M. Arrigoni and G. K. H. Madsen, *J. Chem. Phys.*, 2020, **152**, 044110–044120.

137 B. Hammer, L. B. Hansen and J. K. Nørskov, *Phys. Rev. B*, 1999, **59**, 7413–7421.

138 C. Liu, T. R. Cundari and A. K. Wilson, *J. Phys. Chem. C*, 2012, **116**, 5681–5688.

139 M. W. Chase, C. A. Davies, J. R. Downey, D. J. Frurip, R. A. McDonald and A. N. Syverud, *J. Phys. Chem. Ref. Data, Suppl. 1*, 1985, **14**, 1–1856.

140 Rutile (TiO_2), https://webbook.nist.gov/cgi/cbook.cgi?ID=C1317802&Mask=2, (accessed 12 January 2022).

141 Anatase (TiO_2), https://webbook.nist.gov/cgi/formula?ID=C1317700&Mask=2, (accessed 12 January 2022).

142 J. K. Burdett, T. Hughbanks, G. J. Miller, J. V. Smith and J. W. Richardson, *J. Am. Chem. Soc.*, 2002, **109**, 3639–3646.

143 M. Arrigoni and G. K. H. Madsen, *J. Chem. Phys.*, 2020, **152**, 044110–044120.

144 M. Harb, G. Jeantelot and J.-M. Basset, *J. Phys. Chem. C*, 2019, **123**, 28210–28218.

145 M. Xu, Y. Gao, E. M. Moreno, M. Kunst, M. Muhler, Y. Wang, H. Idriss and C. Wöll, *Phys. Rev. Lett.*, 2011, **106**, 138302–138305.

146 G. Mattioli, F. Filippone, P. Alippi and A. Amore Bonapasta, *Phys. Rev.*

B - Condens. Matter Mater. Phys., 2008, **78**, 241201–241204.

147 D. Vogtenhuber, R. Podloucky, A. Neckel, S. G. Steinemann and A. J. Freeman, *Phys. Rev. B*, 1994, **49**, 2099–2103.

148 T. Tamura, S. Ishibashi, K. Terakura and H. Weng, *Phys. Rev. B - Condens. Matter Mater. Phys.*, 2009, **80**, 195302–195307.

149 D. C. Hurum, A. G. Agrios, K. A. Gray, T. Rajh and M. C. Thurnauer, *J. Phys. Chem. B*, 2003, **107**, 4545–4549.

150 T. Berger, M. Sterrer, O. Diwald, E. Knözinger, D. Panayotov, T. L. Thompson and J. T. Yates, *J. Phys. Chem. B*, 2005, **109**, 6061–6068.

151 R. L. Kurtz, R. Stock-Bauer, T. E. Msdey, E. Román and J. L. De Segovia, *Surf. Sci.*, 1989, **218**, 178–200.

152 E. Serwicka, M. W. Schlierkamp and R. N. Schindler, *Zeitschrift fur Naturforsch. - Sect. A J. Phys. Sci.*, 1981, **36**, 226–232.

153 M. A. Henderson, W. S. Epling, C. H. F. Peden and C. L. Perkins, *J. Phys. Chem. B*, 2002, **107**, 534–545.

154 M. Harb, G. Jeantelot and J.-M. Basset, *J. Phys. Chem. C*, 2019, **123**, 28210–28218.

155 G. Liu, H. G. Yang, J. Pan, Y. Q. Yang, G. Q. M. Lu and H. M. Cheng, *Chem. Rev.*, 2014, **114**, 9559–9612.

156 M. Ramamoorthy, D. Vanderbilt and R. D. King-Smith, *Phys. Rev. B*, 1994, **49**, 16721–16727.

157 S. P. Bates, G. Kresse and M. J. Gillan, *Surf. Sci.*, 1997, **385**, 386–394.

158 H. G. Yang, C. H. Sun, S. Z. Qiao, J. Zou, G. Liu, S. C. Smith, H. M. Cheng and G. Q. Lu, *Nat. 2008 4537195*, 2008, **453**, 638–641.

159 J. Oviedo, M. A. S. Miguel and J. F. Sanz, *J. Chem. Phys.*, 2004, **121**, 7427–7433.

160 P. Banerjee, C. Roy, A. J. Santos, S. K. De, F. M. Morales and S. Bhattacharyya, *Mater. Today Nano*, 2022, **17**, 100153–100163.

161 B. Wang, R. Wang and H. Fan, *J. Phys. Chem. C*, 2022, **126**, 974–985.

162 C. Günnemann, C. Haisch, M. Fleisch, J. Schneider, A. V. Emeline and D. W. Bahnemann, *ACS Catal.*, 2019, **9**, 1001–1012.

163 W. F. Huang, P. Raghunath and M. C. Lin, *J. Comput. Chem.*, 2011, **32**, 1065–1081.

164 B. Ohler, S. Prada, G. Pacchioni and W. Langel, *J. Phys. Chem. C*, 2013, **117**, 358–367.

165 D. E. Barlaz and E. G. Seebauer, *J. Vac. Sci. Technol. A Vacuum, Surfaces, Film.*, 2016, **34**, 020603–020607.

166 M. Ramamoorthy, D. Vanderbilt and R. D. King-Smith, *Phys. Rev. B*, 1994, **49**, 16721–16727.

167 A. Kiejna, T. Pabisiak and S. W. Gao, *J. Phys. Condens. Matter*, 2006, **18**, 4207–4217.

168 A. Vittadini, M. Casarin and A. Selloni, *Theor. Chem. Accounts 2006 1175*, 2006, **117**, 663–671.

169 M. Lazzeri and A. Selloni, *Phys. Rev. Lett.*, 2001, **87**, 266105–266108.

170 M. Lazzeri, A. Vittadini and A. Selloni, *Phys. Rev. B*, 2001, **63**, 155409–155417.

171 P. Lindan, N. Harrison and M. Gillan, *Phys. Rev. B*, 1997, **55**, 15919–15927.

172 S. D. Elliott and S. P. Bates, *Phys. Rev. B*, 2003, **67**, 035421–035425.

173 H. Perron, C. Domain, J. Roques, R. Drot, E. Simoni and H. Catalette, *Theor. Chem. Accounts 2007 1174*, 2007, **117**, 565–574.

174 F. Zasada, W. Piskorz, S. Godlewski, J. S. Prauzner-Bechcicki, A. Tekiel, J. Budzioch, P. Cyganik, M. Szymonski and Z. Sojka, *J. Phys. Chem. C*, 2011, **115**, 4134–4144.

175 L. Deng, M. Mrksich and G. M. Whitesides, *J. Am. Chem. Soc.*, 1996, **118**, 5136–5137.

176 F. Tielens, D. Costa, V. Humblot and C. M. Pradier, *J. Phys. Chem. C*, 2007, **112**, 182–190.

177 J. C. Love, L. A. Estroff, J. K. Kriebel, R. G. Nuzzo and G. M. Whitesides, *Chem. Rev.*, 2005, **105**, 1103–1169.

178 U. Diebold, *Surf. Sci. Rep.*, 2003, **48**, 53–229.

179 A. Tekiel, J. S. Prauzner-Bechcicki, S. Godlewski, J. Budzioch and M. Szymonski, *J. Phys. Chem. C*, 2008, **112**, 12606–12609.

180 W. Zhang, L. Cao, L. Wan, L. Liu and F. Xu, *J. Phys. Chem. C*, 2013, **117**, 21351–21358.

181 J. S. Prauzner-Bechcicki, S. Godlewski, A. Tekiel, P. Cyganik, J. Budzioch and M. Szymonski, *J. Phys. Chem. C*, 2009, **113**, 9309–9315.

182 P. Rahe, M. Nimmrich, A. Nefedov, M. Naboka, C. Woll and A. Kuḧnle, *J. Phys. Chem. C*, 2009, **113**, 17471–17478.

183 F. Schreiber, *J. Phys. Condens. Matter*, 2004, **16**, R881.

184 F. Zasada, W. Piskorz, S. Godlewski, J. S. Prauzner-Bechcicki, A. Tekiel, J. Budzioch, P. Cyganik, M. Szymonski and Z. Sojka, *J. Phys. Chem. C*,

2011, **115**, 4134–4144.

185 I. Lyubinetsky, Z. Q. Yu and M. A. Henderson, *J. Phys. Chem. C*, 2007, **111**, 4342–4346.

186 D. S. Martin, R. J. Cole and S. Haq, *Phys. Rev. B*, 2002, **66**, 155427–155434.

187 H. Li, M. Eddaoudi, M. O’Keeffe and O. M. Yaghi, *Nature*, 1999, **402**, 276–279.

188 F. Zasada, W. Piskorz, J. Gryboś and Z. Sojka, *J. Phys. Chem. C*, 2014, **118**, 8971–8981.

189 J. K. Bristow, K. T. Butler, K. L. Svane, J. D. Gale and A. Walsh, *J. Mater. Chem. A*, 2017, **5**, 6226–6232.

190 A. Bétard and R. A. Fischer, *Chem. Rev.*, 2011, **112**, 1055–1083.

191 W. Xuan, C. Zhu, Y. Liu and Y. Cui, *Chem. Soc. Rev.*, 2012, **41**, 1677–1695.

192 Q. L. Zhu and Q. Xu, *Chem. Soc. Rev.*, 2014, **43**, 5468–5512.

193 J. Lee, O. K. Farha, J. Roberts, K. A. Scheidt, S. T. Nguyen and J. T. Hupp, *Chem. Soc. Rev.*, 2009, **38**, 1450–1459.

194 B. Li, H. M. Wen, Y. Cui, W. Zhou, G. Qian and B. Chen, *Adv. Mater.*, 2016, **28**, 8819–8860.

195 Z. Y. Gu, C. X. Yang, N. Chang and X. P. Yan, *Acc. Chem. Res.*, 2012, **45**, 734–745.

196 J. Winarta, B. Shan, S. M. McIntyre, L. Ye, C. Wang, J. Liu and B. Mu, *Cryst. Growth Des.*, 2019, **20**, 1347–1362.

197 C. A. Allen and S. M. Cohen, *Inorg. Chem.*, 2014, **53**, 7014–7019.

198 A. P. Smalley, D. G. Reid, J. C. Tan and G. O. Lloyd, *CrystEngComm*, 2013, **15**, 9368–9371.

199 S. Lee, H. B. Bürgi, S. A. Alshmimri and O. M. Yaghi, *J. Am. Chem. Soc.*, 2018, **140**, 8958–8964.

200 Crystallography Open Database, http://www.crystallography.net/cod/index.php, (accessed 8 February 2022).

201 F. Zasada, W. Piskorz, S. Godlewski, J. S. Prauzner-Bechcicki, A. Tekiel, J. Budzioch, P. Cyganik, M. Szymonski and Z. Sojka, *J. Phys. Chem. C*, 2011, **115**, 4134–4144.

APPENDIX-1

Table A1- 1: Calculated formation energies (E_{form}) using different XC functionals varying the basis set and their difference than the experimental data (ΔE_{form}). Literature values are highlighted.

Approximation	XC functional	Basis set	Rutile		Anatase	
			E_{form} (eV)	ΔE_{form} (eV)	E_{form} (eV)	ΔE_{form} (eV)
LDA	LDA	Light	-10.250	-0.466	-10.253	-0.524
		Intermediate	-10.175	-0.391	-10.187	-0.458
GGA	AM05	Light	-9.016	0.768	-9.073	0.656
		Intermediate	-8.938	0.846	-9.005	0.724
	PBE	Light	-9.041	0.743	-9.106	0.623
		Intermediate	-8.969	0.815	-9.044	0.685
		Tight	-9.011	0.773	-9.107	0.622
	PBEsol	Light	-9.345	0.439	-9.371	0.358
		Intermediate	-9.273	0.511	-9.309	0.420
		Tight	-9.322	0.462	-9.382	0.347
	rPBE	Light	-8.469	1.315	-8.570	1.159
		Intermediate	-8.402	1.382	-8.512	1.217
meta-GGA	M06-L	Light	-9.356	0.428	-9.269	0.460
		Intermediate	-9.253	0.531	-9.191	0.538
	SCAN	Light	-10.481	-0.697	-10.376	-0.647
		Intermediate	-10.090	-0.306	-10.093	-0.364
		Literature[105]	**-10.656**		**-10.680**	
	mBEEF	Light	-9.804	-0.020	-9.873	-0.144
		Intermediate	-9.682	0.102	-9.763	-0.034
Hybrid	B3LYP	Light	-10.021	-0.237	-10.100	-0.371
		Intermediate	-9.951	-0.167	-10.037	-0.308
	HSE06	Light	-9.614	0.170	-9.646	0.083
		Intermediate	-9.573	0.211	-9.579	0.150
	PBE0	Light	-9.577	0.207	-9.614	0.115
		Intermediate	-9.501	0.283	-9.549	0.180
Hybrid meta-GGA	M06	Light	-10.276	-0.492	-9.856	-0.127
		Intermediate	-9.751	0.033	-9.803	-0.074
Formation energy at 298 K[139]			-9.784		-9.729	

Table A1- 2: Unit cell parameters (a and c), their difference than the experimental data (Δa and Δc) and, the β angle of the rutile TiO_2 calculated using different XC functionals varying the basis set. Literature values are highlighted.

Approximation	XC functional	Basis set	a (Å)	Δa (Å)	c (Å)	Δc (Å)	β (°)
LDA	LDA	Light	4.550	-0.043	2.926	-0.033	90.000
		Intermediate	4.547	-0.046	2.922	-0.037	90.000
GGA	AM05	Light	4.597	0.004	2.948	-0.011	90.000
		Intermediate	4.594	0.001	2.944	-0.015	90.000
	PBE	Light	4.643	0.050	2.973	0.014	90.000
		Intermediate	4.640	0.047	2.969	0.010	90.000
		Tight	4.642	0.049	2.963	0.004	90.000
	PBEsol	Light	4.591	-0.002	2.948	-0.011	90.000
		Intermediate	4.587	-0.006	2.944	-0.015	90.000
		Tight	4.589	-0.004	2.938	-0.021	90.000
	rPBE	Light	4.685	0.092	2.988	0.029	90.000
		Intermediate	4.681	0.088	2.985	0.026	90.000
meta-GGA	M06-L	Light	4.605	0.012	2.989	0.030	90.000
		Intermediate	4.603	0.010	2.982	0.023	90.000
	SCAN	Light	4.594	0.001	2.964	0.005	90.000
		Intermediate	4.635	0.042	2.970	0.011	90.000
	mBEEF	Light	4.625	0.032	2.970	0.011	90.000
		Intermediate	4.602	0.009	2.961	0.002	90.000
Hybrid	B3LYP	Light	4.619	0.026	2.973	0.014	90.002
		Intermediate	4.616	0.023	2.970	0.011	89.999
	HSE06	Light	4.578	-0.015	2.958	-0.001	89.996
		Intermediate	4.572	-0.021	2.953	-0.006	90.000
	PBE0	Light	4.575	-0.018	2.954	-0.005	90.000
		Intermediate	4.570	-0.023	2.951	-0.008	90.000
Hybrid meta-GGA	M06	Light	4.600	0.007	2.952	-0.007	89.999
		Intermediate	4.596	0.003	2.951	-0.008	90.001
Neutron diffraction data at 295 K[142]			**4.593**		**2.959**		
PBE[105]			**4.644**		**2.967**		
PBE+U (6 eV)[105]			**4.679**		**3.044**		
SCAN[105]			**4.591**		**2.957**		
SCAN+U (2 eV)[105]			**4.604**		**2.982**		
HSE (25% Fock)[105]			**4.582**		**2.946**		

Table A1- 3: Unit cell parameters (a and c), their difference than the experimental data (Δa and Δc) and, the β angle of the anatase TiO_2 calculated using different XC functionals varying the basis set. Literature values are highlighted.

Approximation	XC functional	Basis set	a (Å)	Δa (Å)	c (Å)	Δc (Å)	β (°)
LDA	LDA	Light	3.744	-0.041	9.489	-0.023	90.000
		Intermediate	3.738	-0.047	9.490	-0.022	90.000
GGA	AM05	Light	3.769	-0.016	9.640	0.128	90.000
		Intermediate	3.764	-0.021	9.643	0.131	90.000
	PBE	Light	3.800	0.015	9.742	0.230	90.000
		Intermediate	3.795	0.010	9.742	0.230	90.000
		Tight	3.798	0.013	9.706	0.194	90.000
	PBEsol	Light	3.772	-0.013	9.584	0.072	90.000
		Intermediate	3.766	-0.019	9.586	0.074	90.000
		Tight	3.768	-0.017	9.561	0.049	90.000
	rPBE	Light	3.823	0.038	9.843	0.331	90.000
		Intermediate	3.817	0.032	9.846	0.334	90.000
meta-GGA	M06-L	Light	3.796	0.011	9.663	0.151	90.000
		Intermediate	3.785	0.000	9.697	0.185	90.000
	SCAN	Light	3.851	0.066	8.979	-0.533	90.004
		Intermediate	3.776	-0.009	9.871	0.359	90.000
	mBEEF	Light	3.770	-0.015	9.846	0.334	90.000
		Intermediate	3.762	-0.023	9.751	0.239	90.000
Hybrid	B3LYP	Light	3.781	-0.004	9.765	0.253	90.000
		Intermediate	3.775	-0.010	9.762	0.250	90.068
	HSE06	Light	3.762	-0.023	9.644	0.132	90.000
		Intermediate	3.756	-0.029	9.644	0.132	90.000
	PBE0	Light	3.759	-0.026	9.631	0.119	89.982
		Intermediate	3.749	-0.036	9.632	0.120	90.049
Hybrid meta-GGA	M06	Light	3.766	-0.019	9.651	0.139	90.002
		Intermediate	3.759	-0.026	9.636	0.124	90.037
Neutron diffraction data at 295 K[142]			**3.785**		**9.512**		
PBE[105]			**3.802**		**9.703**		
PBEsol[143]			**3.77**		**9.56**		
PBE+U (6 eV)[105]			**3.881**		**9.765**		
PBE+U[Ti][143]			**3.88**		**9.77**		
PBE+U[Ti,O][143]			**3.86**		**9.74**		
SCAN[143]			**3.777**		**9.587**		
SCAN+U (2 eV)[105]			**3.805**		**9.599**		
HSE (25% Fock)[105]			**3.756**		**9.615**		
HSE15[143]			**3.78**		**9.64**		

Table A1- 4: Calculated band gap (E_g) using different XC functionals varying the basis set and, their difference than the experimental data (ΔE_g). Literature values are highlighted.

Approximation	XC functional	Basis set	Rutile E_g (eV)	ΔE_g (eV)	Anatase E_g (eV)	ΔE_g (eV)
LDA	LDA	Light	1.77	-1.26	2.09	-1.11
		Intermediate	1.81	-1.22	2.11	-1.09
GGA	AM05	Light	1.79	-1.24	2.15	-1.05
		Intermediate	1.83	-1.20	2.18	-1.02
	PBE	Light	1.77	-1.26	2.13	-1.07
		Intermediate	1.80	-1.23	2.15	-1.05
		Tight	1.84	-1.19	2.16	-1.04
	PBEsol	Light	1.77	-1.26	2.11	-1.09
		Intermediate	1.81	-1.22	2.13	-1.07
		Tight	1.85	-1.18	2.14	-1.06
	rPBE	Light	1.77	-1.26	2.14	-1.06
		Intermediate	1.81	-1.22	2.16	-1.04
meta-GGA	M06-L	Light	2.06	-0.97	2.44	-0.76
		Intermediate	2.08	-0.95	2.49	-0.71
	SCAN	Light	2.08	-0.95	2.02	-1.18
		Intermediate	2.17	-0.86	2.63	-0.57
	mBEEF	Light	2.19	-0.84	2.66	-0.54
		Intermediate	2.22	-0.81	2.68	-0.52
Hybrid	B3LYP	Light	3.53	0.50	3.92	0.72
		Intermediate	3.58	0.55	3.95	0.75
	HSE06	Light	3.27	0.24	3.65	0.45
		Intermediate	4.09	1.06	3.69	0.49
	PBE0	Light	4.06	1.03	4.42	1.22
		Intermediate	4.11	1.08	4.46	1.26
Hybrid meta-GGA	M06	Light	4.03	1.00	4.38	1.18
		Intermediate	4.10	1.07	4.40	1.20
Experimental data at 298 K[144,145]			**3.03**		**3.20**	
PBE[105]			**1.83**		**2.10**	
PBE+U (6 eV)[105]			**2.49**		**2.82**	
SCAN[105]			**2.23**		**2.56**	
SCAN+U (2 eV)[105]			**2.47**		**2.80**	
HSE (25% Fock)[105]			**3.42**		**3.77**	
LMTO-ASA+G_0W_0[106]			**2.50**			
LCAO-PBE[106]			**1.88**		**2.36**	
LCAO-PBE0[106]			**4.05**		**4.50**	
PAW-PBE[106]			**3.03**		**2.08**	
PW-PPS-LDA[106]			**1.88**			
OLCAO-LDA-AE[106]			**1.78**		**2.04**	
PW-PPs-PBE+G_0W_0[106]			**2.05**			
Gaussian basis, B3LYP[106]					**3.70**	

APPENDIX-2

Table A2- 1: Data for slabs generation in different facets of anatase TiO_2.

Facet	No. of Ti_2O_4 layers	No. of Ti atoms	No. of O atoms	No. of unit cells
Anatase 101	1	2	4	0.5
	2	4	8	1
	3	6	12	1.5
	4	8	16	2
	5	10	20	2.5
	6	12	24	3
Anatase 001	2	4	8	1
	4	8	16	2
	6	12	24	3
Anatase 100	2	4	8	1
	4	8	16	2
	6	12	24	3
Anatase 110	1	2	4	0.5
	2	4	8	1
	3	6	12	1.5
	4	8	16	2
	5	10	20	2.5
	6	12	24	3
	7	14	28	3.5

Table A2- 2: Data for slabs generation in different facets of rutile TiO_2.

Facet	No. of Ti_2O_4 layers	No. of Ti atoms	No. of O atoms	No. of unit cells
Rutile 110	1	2	4	1
	2	4	8	2
	3	6	12	3
	4	8	16	4
	5	10	20	5
	6	12	24	6
Rutile 101	1	2	4	1
	2	4	8	2
	3	6	12	3
	4	8	16	4
	5	10	20	5
	6	12	24	6

APPENDIX-3

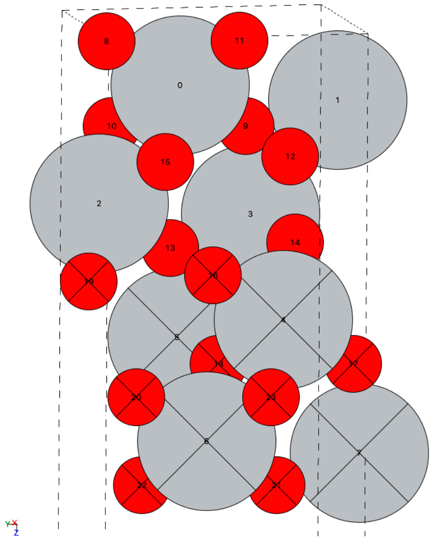

Figure A3.1: The 4-layer slab model, with top 2-layers unconstrained of (101) facet of rutile TiO_2 where a dotted line highlights the conventional unit cell, grey and red spheres represent Ti and O atoms respectively.

Table A3- 1: Unrelaxed coordinates (x_1, y_1, z_1), relaxed coordinates (x_2, y_2, z_2), and relaxations (Δx, Δy, Δz) of near-surface atoms of (101) facet of rutile TiO_2 where atom index is referred to Figure A3.1.

(101) Rutile		Unrelaxed coordinates			Relaxed coordinates			Relaxations		
Atom	Atom index	x_1	y_1	z_1	x_2	y_2	z_2	Δx	Δy	Δz
Ti	0	2.295	3.524	1.240	2.509	3.408	1.329	0.214	-0.116	0.089
Ti	1	0.000	0.796	1.240	-0.214	0.680	1.329	-0.214	-0.116	0.089
Ti	2	2.295	5.116	3.720	2.202	5.152	3.688	-0.093	0.036	-0.032
Ti	3	0.000	2.389	3.720	0.093	2.424	3.688	0.093	0.035	-0.032
O	8	3.695	4.702	0.484	3.593	4.725	0.531	-0.102	0.023	0.047
O	9	0.896	2.346	1.996	0.907	2.359	1.987	0.011	0.013	-0.009
O	10	1.399	5.074	1.996	1.389	5.087	1.987	-0.010	0.013	-0.009
O	11	3.191	1.974	0.484	3.294	1.997	0.531	0.103	0.023	0.047
O	12	3.695	0.838	2.964	3.674	0.827	3.003	-0.021	-0.011	0.039
O	13	0.896	3.939	4.477	0.915	3.931	4.478	0.019	-0.008	0.001
O	14	1.399	1.211	4.477	1.380	1.203	4.478	-0.019	-0.008	0.001
O	15	3.191	3.566	2.964	3.212	3.555	3.003	0.021	-0.011	0.039

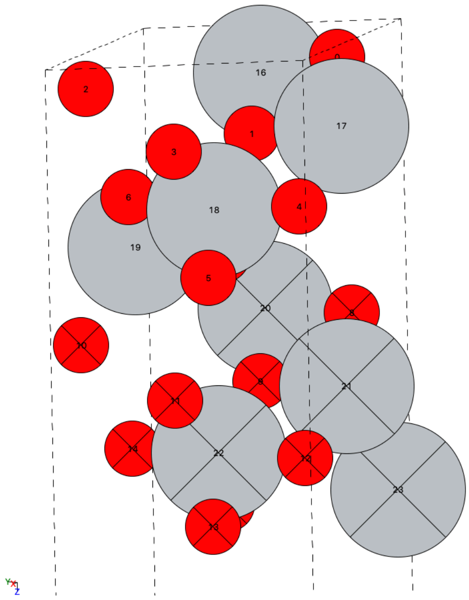

Figure A3.2: The 4-layer slab model, with top 2-layers unconstrained of (110) facet of anatase TiO_2 where a dotted line highlights the conventional unit cell, grey and red spheres represent Ti and O atoms respectively.

Table A3- 2: Unrelaxed coordinates (x_1, y_1, z_1), relaxed coordinates (x_2, y_2, z_2), and relaxations (Δx, Δy, Δz) of near-surface atoms of (110) facet of anatase TiO_2 where atom index is referred to Figure A3.2.

(110) Anatase		Unrelaxed coordinates			Relaxed coordinates			Relaxations		
Atom	Atom index	*x*	*y*	*z*	*x*	*y*	*z*	Δ*x*	Δ*y*	Δ*z*
O	0	2.000	0.411	0.667	2.094	0.597	0.508	0.094	0.186	-0.159
O	1	3.334	1.985	2.000	3.389	2.044	2.002	0.055	0.059	0.002
O	2	7.335	4.381	0.667	7.241	4.195	0.508	-0.094	-0.186	-0.159
O	3	6.001	2.807	2.000	5.946	2.748	2.002	-0.055	-0.059	0.002
O	4	4.668	0.411	3.334	4.677	0.422	3.275	0.009	0.011	-0.059
O	5	6.001	1.985	4.668	6.013	1.986	4.661	0.012	0.001	-0.007
O	6	4.668	4.381	3.334	4.658	4.370	3.275	-0.010	-0.011	-0.059
O	7	3.334	2.807	4.668	3.323	2.806	4.661	-0.011	-0.001	-0.007
Ti	16	2.000	2.396	0.667	2.000	2.396	0.939	0.000	0.000	0.272
Ti	17	3.334	0.000	2.000	3.334	0.000	1.748	0.000	0.000	-0.252
Ti	18	4.668	2.396	3.334	4.668	2.396	3.437	0.000	0.000	0.103
Ti	19	3.334	4.792	4.668	3.334	4.792	4.588	0.000	0.000	-0.080

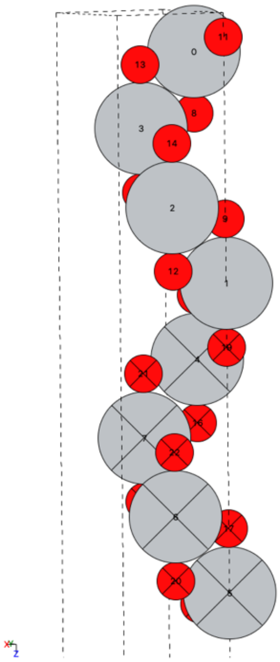

Figure A3.3: The 4-layer slab model, with top 2-layers unconstrained of (001) facet of anatase TiO_2 where a dotted line highlights the conventional unit cell, grey and red spheres represent Ti and O atoms respectively.

Table A3- 3: Unrelaxed coordinates (x_1, y_1, z_1), relaxed coordinates (x_2, y_2, z_2), and relaxations (Δx, Δy, Δz) of near-surface atoms of (001) facet of anatase TiO_2 where atom index is referred to Figure A3.3.

(001) Anatase		Unrelaxed coordinates			Relaxed coordinates			Relaxations		
Atom	Atom index	x	y	z	x	y	z	Δx	Δy	Δz
Ti	0	0.000	1.886	1.198	0.000	1.886	1.248	0.000	0.000	0.050
Ti	1	0.000	0.000	8.386	0.000	0.000	8.386	0.000	0.000	0.000
Ti	2	1.886	0.000	5.990	1.886	0.000	5.986	0.000	0.000	-0.004
Ti	3	1.886	1.886	3.594	1.886	1.886	3.583	0.000	0.000	-0.011
O	8	0.000	1.886	3.183	0.000	1.886	3.169	0.000	0.000	-0.014
O	9	0.000	0.000	6.401	0.000	0.000	6.399	0.000	0.000	-0.002
O	10	0.000	1.886	8.797	0.000	1.886	8.797	0.000	0.000	0.000
O	11	0.000	0.000	0.787	0.000	0.000	0.761	0.000	0.000	-0.026
O	12	1.886	0.000	7.975	1.886	0.000	7.973	0.000	0.000	-0.002
O	13	1.886	1.886	1.609	1.886	1.886	1.624	0.000	0.000	0.015
O	14	1.886	0.000	4.005	1.886	0.000	4.005	0.000	0.000	0.000
O	15	1.886	1.886	5.579	1.886	1.886	5.572	0.000	0.000	-0.007

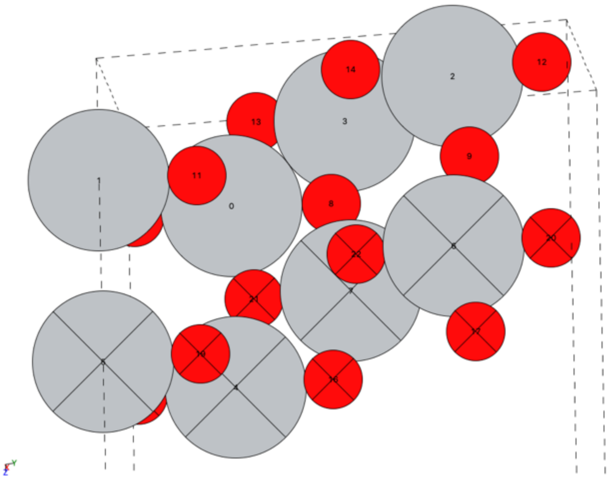

Figure A3.4: The 4-layer slab model, with top 2-layers unconstrained of (100) facet of anatase TiO_2 where a dotted line highlights the conventional unit cell, grey and red spheres represent Ti and O atoms respectively.

Table A3. 1: Unrelaxed coordinates (x_1, y_1, z_1), relaxed coordinates (x_2, y_2, z_2), and relaxations $(\Delta x, \Delta y, \Delta z)$ of near-surface atoms of (100) facet of anatase TiO_2 where atom index is referred to Figure A3.4.

(100) Anatase		Unrelaxed coordinates			Relaxed coordinates			Relaxations		
Atom	Atom index	*x*	*y*	*z*	*x*	*y*	*z*	Δ*x*	Δ*y*	Δ*z*
Ti	0	1.886	2.396	2.829	1.886	2.396	2.659	0.000	0.000	-0.170
Ti	1	0.000	0.000	2.829	0.000	0.000	2.659	0.000	0.000	-0.170
Ti	2	0.000	7.188	0.943	0.000	7.245	1.022	0.000	0.057	0.079
Ti	3	1.886	4.792	0.943	1.886	4.734	1.022	0.000	-0.058	0.079
O	8	1.886	4.381	2.829	1.886	4.429	2.787	0.000	0.048	-0.042
O	9	0.000	7.599	2.829	0.000	7.551	2.787	0.000	-0.048	-0.042
O	10	1.886	0.411	2.829	1.886	0.410	2.729	0.000	-0.001	-0.100
O	11	0.000	1.985	2.829	0.000	1.986	2.729	0.000	0.001	-0.100
O	12	0.000	9.173	0.943	0.000	9.056	0.879	0.000	-0.117	-0.064
O	13	1.886	2.807	0.943	1.886	2.924	0.879	0.000	0.117	-0.064
O	14	0.000	5.203	0.943	0.000	5.167	0.698	0.000	-0.036	-0.245
O	15	1.886	6.777	0.943	1.886	6.813	0.698	0.000	0.036	-0.245